Bridging the Pressure Gap in the Surface Analysis of Transition Metal Catalyzed Reactions

BY
MOHAMMED KAYED ABDEL-RAHMAN
B.S., University of Illinois at Chicago, Chicago, 2012

THESIS

Submitted as partial fulfillment of the requirements
for the degree of Doctor of Philosophy in Chemistry
in the Graduate College of the
University of Illinois at Chicago, 2021

Chicago, Illinois

Defense Committee:

Michael Trenary, Advisor and Chair
Nan Jiang
Preston Snee
Ksenija Glusac
Aditya Ashi Savara, Oak Ridge National Laboratory

Dedicated to my darling wife, Sara. Without your love and support, this would not be possible.

ACKNOWLEDGEMENTS

The journey toward the doctorate degree is not one that is taken alone; therefore, I would like to acknowledge those who helped me along the way to this moment. The completion of my dissertation would not have been possible without the support of my advisor, Professor Michael Trenary, who provided me with the opportunity to conduct high quality research and introduce me to surface science and catalysis. I also thank him for supporting me with Research Assisstantships during the completion of the program. I extend my thanks to my committee members Preston Snee, Nan Jiang, Ksenija Glusac, and Aditya Ashi Savara for their time in the review of this dissertation.

I would like to thank my mentors Dr. Xu Feng and Dr. Christopher Kruppe for their instruction and patience as I became familiar with the instrumentation and apparatuses in the laboratories. During my studies, there were times when the equipment would malfunction. I learned how to troubleshoot, diagnose, and repair both the instruments and the computer systems from Dr. Paul Melnikov. I am glad to have worked alongside the other graduate students Mark Muir, Ravi Ranjan, Arephin Islam, Buddhika Wijenayake, and David Molina all of whom I am proud to call my “brothers of the lab”. Through the hard times and the easy times, we always found a way to make the lab a joyful and low-stress environment. I also thank the Department of Chemistry at UIC for supporting my endeavor through teaching assistantships, and the department staff without whom the program would not function. Without the assistance of the UIC machine, glass, and electronics shops, the work presented in this dissertation would not be possible, so I thank the machine shop staff: Kevin Lynch, Dave Kuntzelman, Rick Frueh, and Rich Dojutrek, glassblowing specialist Brian Schwandt, and electronics specialist Don Rippon.

Aside from professional support, I would like to thank my family and friends for their support. I thank my wife Sara Shuaibi for her patience and support while tolerating the hectic

lifestyle of a graduate student, my parents, Kayed Alkhdour and Rania Abdel-Rahman, for their unwavering support and confidence, and my son Yusuf for always brightening my days. I extend thanks to my friend and colleague Panagiotis Alexakos for convincing me to apply to the Ph.D. program back in 2014.

CONTRIBUTION OF AUTHORS

One of the benefits of conducting research is the collaborative environment. Colleagues and collaborators assisted in improving the quality of the projects presented in this dissertation. Chapter 1 provides information regarding current methods used in academic and industrial heterogeneous catalysis research, some which are portions of previously published articles: Abdel-Rahman, M.K.; Feng, X.; Muir, M.; Gale, K.; Xu, Y.; Trenary, M. *Phys. Chem. Chem. Phys.* **2019**, 21, 5274-5284. Copyright (2019) PCCP Owners Society, Feng, X.; Abdel-Rahman, M.K.; Kruppe, C.M.; Trenary, M. *Surface Science* **2017**, 664, 1-7. Copyright (2017) Elsevier B.V., and Abdel-Rahman, M.K.; Trenary, M. *ACS Catalysis* **2020**, 10, 9716-9724. Copyright (2020) American Chemical Society.

Chapter 2 introduces the experimental apparatuses and techniques. The work performed on these systems was with the assistance of Xu Feng and Christopher M. Kruppe. Ravi Ranjan, Arephin Islam, Hamzzat Soyege, and Jonathon Kruppe assisted with sample preparation. The systems were maintained with assistance from the machine, glass, and electronics shops at UIC notably Kevin Lynch, Dave Kuntzelman, Rick Frueh, Brian Schwandt, and Don Rippon.

The results from investigating the reaction pathways of HCN are presented in Chapter 3. I performed the HCN synthesis and the experiments with Pd(111). Xu Feng assisted in the synthesis of HCN and preliminary experiments with Pd(111). Mark Muir performed the experiments on Ru(001). Kushal Gale and Ye Xu provided the computational results and edited the manuscript. Michael Trenary assisted with data interpretation and editing the manuscript. The results are reprinted from ref. (1) with permission from the PCCP Owner Societies.

Chapter 4 provides the results from the growth of V_2O_5 thin films. I assisted Xu Feng in conducting the experiments and collecting data. Xu Feng interpreted the data and wrote the manuscript. Christopher M. Kruppe installed the Pd(111) crystal. Michael Trenary provided

additional interpretations and edited the manuscript. The results are reprinted from ref. (2) with permission from Elsevier.

Chapter 5 discusses the oxidative desulfurization of dibenzothiophene which is an ongoing project. Xu Feng and I performed the experiments and interpreted the data. I performed additional data analysis during the writing of this chapter.

Chapter 6 provides the results from the partial hydrogenation of propyne over a Pd/Cu(111) single atom alloy catalyst. I performed all the experiments, interpreted the data, and wrote the manuscript. Michael Trenary provided additional interpretations and edited the manuscript. This work is reprinted with permission from Abdel-Rahman, M.K.; Trenary, M. *ACS Catal.*, **2020**, 10, 9716-9724. Copyright (2020) American Chemical Society.

TABLE OF CONTENTS

LIST OF TABLES

LIST OF FIGURES

LIST OF ABBREVIATIONS

AES	Auger Electron Spectroscopy
AFM	Atomic Force Microscopy
AP	Ambient Pressure
ATR	Attenuated Total Reflection
CI-NEB	Climbing Image Nudged Elastic Band
CMA	Cylindrical Mirror Analyzer
CVD	Chemical Vapor Deposition
DBT	Dibenzothiophene
DBTO	Dibenzothiophene Sulfoxide ($C_{12}H_8SO$)
$DBTO_2$	Dibenzothiophene Sulfone ($C_{12}H_8SO_2$)
DFT	Density Functional Theory
EPMA	Electron Probe Microanalysis
ESCA	Electron Spectroscopy for Chemical Analysis
FWHM	Full Width at Half Maximum
GGA	General Gradient Approximation
HDS	Hydrodesulfurization
HOPG	Highly Ordered Pyrolytic Graphite
HREELS	High Resolution Electron Energy Loss Spectroscopy

IMFP	Inelastic Mean Free Path
IR	Infrared Radiation
IR(R)AS	Infrared Reflection Absorption Spectroscopy
IS	Initial State
LEED	Low Energy Electron Diffraction
MCT	Mercury Cadmium Telluride
ODS	Oxidative Desulfurization
PAW	Projector Augmented Wave
PD-RAIRS	Polarization Dependent Reflection Absorption Infrared Spectroscopy
PID	Proportional Integral Derivative
PVD	Physical Vapor Deposition
QMS	Quadrupole Mass Spectrometer
RAIRS	Reflection Absorption Infrared Spectroscopy
RPBE	Revised Perdew-Burke-Ernzerhof
SAA	Single Atom Alloy
STM	Scanning Tunneling Microscopy
TDS	Thermal Desorption Spectroscopy
TOF	Turnover Frequency

TPD	Temperature Programmed Desorption
TPRS	Temperature Programmed Reaction Spectroscopy
TS	Transition State
UHV	Ultrahigh Vacuum
VASP	Vienna Ab-Initio Simulations Package
vdW	Van der Waals
XPS	X-ray Photoelectron Spectroscopy
ZPE	Zero Point Energy

SUMMARY

Surface scientists strive to understand the interaction between molecules and surfaces. These interactions are typically studied under low temperature and ultrahigh vacuum (UHV) conditions. These conditions minimize contamination from background gases and allow for the detailed study of gas-surface interactions. One such study investigates the reactivity of HCN with various transition metal surfaces. Reflection absorption infrared spectroscopy (RAIRS) was the characterization technique used in this study. The metal surface selection rules (MSSR) for RAIRS allows for the determination of adsorption geometry based on the observed features. HCN was confirmed to bond to the Pd(111) surface in an upright manner where the lone pair electrons on the nitrogen atoms interact with the Pd surface. Although, density functional theory (DFT) calculations predict the di-σ HCN adsorption geometry to be more stable, the upright HCN geometry can be observed at 90 K after a high exposure of HCN to the Pd surface. The upright HCN reacts through a bimolecular mechanism to form the aminocarbyne CNH_2. This reaction was identified to occur on Pt(111) but not on Cu(111), Cu(100), or Ru(001). On the Cu surfaces, HCN will desorb without reaction. On the Ru(001) surface, HCN decomposes to surface-bound H, C, and N atoms. DFT calculations confirmed the experimental conclusions by providing the energy of various adsorption states. The lowest energy states corresponded with each of the experimental conclusions. The significance of these conclusions allows scientists and engineers to design new materials to favor a particular reaction. The design of new materials involves minimizing the use of precious metals due to scarcity, cost, and reactivity. Metal oxide thin films provide an attractive alternative to pure metal catalysts. Vanadium oxides garnered much attention in the electrochemical and catalysis communities. Vanadium oxide reversibly and easily transitions between its many oxidation states V^{2+} to V^{5+}. The method of physical vapor deposition was used to deposit V_2O_5 on Pd(111). V_2O_5 powder was heated to 675°C at 1.0×10^{-10} Torr which

increased the vapor pressure of V_2O_5. With the vapor pressure increased, V_2O_5 was deposited on the Pd(111) which was held at room temperature. The thin films were mainly characterized with X-ray photoelectron spectroscopy (XPS); however, low energy electron diffraction (LEED), and RAIRS were found to be useful secondary characterization methods. The deposited V_2O_5 thin films retained the V_2O_5 stoichiometry throughout the process. Upon heating the Pd(111) substrate, V_2O_5 reduced to VO_2 at 700 K and to V_2O_3 at 1000 K. After the successful deposition and reduction of V_2O_5 on Pd(111), the ability of V_2O_5 to oxidize sulfur containing hydrocarbons was investigated. Sulfur contamination in fossil fuels reduces the efficiency of the fuel as an energy source and introduces harmful sulfur oxides into the environment. Oxidative desulfurization (ODS) is a method of removing sulfur from hydrocarbons as SO_2. Desulfurization of dibenzothiophene (DBT) is difficult due to the delocalization of the sulfur lone pair electrons throughout the aromatic structure of the molecule. The oxidation of DBT to its sulfoxide (DBTO) and sulfone ($DBTO_2$) using V_2O_5 as the oxidizing agent was investigated. Unfortunately, preliminary temperature programmed desorption (TPD) studies indicate a weak interaction between DBT and the V_2O_5 thin films. DBT desorbs from the thin films at 150 K without reaction. This reaction will be investigated more thoroughly in the future. Another industrially relevant reaction is the partial hydrogenation of alkynes to alkenes. Alkenes are desired for their ability to form polymers with various properties. Alkynes are common contaminants in the alkene production process. While partial hydrogenation can be studied under UHV conditions, the information gained from UHV studies is more desirable when gathered under industrial conditions such as high temperatures and pressure. In recent years, many surface science techniques have been developed or modified to study gas-surface interactions under industrial conditions. One such modification is polarization dependent reflection absorption infrared spectroscopy (PD-

RAIRS). Alongside ambient pressure techniques, single atom alloy (SAA) catalysts provide attractive alternatives to precious metal-rich catalysts. Pd/Cu SAA catalysts allow for stable H transfer from Pd sites to Cu sites to promote alkene selectivity. The partial hydrogenation of propyne to propene over Cu(111) and a 2% Pd/Cu(111) SAA was studied under ambient pressures with PD-RAIRS. The SAA enhanced the conversion and selectivity of the reaction. The activation energy of the reaction over the SAA catalyst was equal to that of a pure Pd catalyst and half that of a pure Cu catalyst. These conclusions were drawn from surface sensitive methods performed under industrial conditions. The versatility and significance of surface analysis methods will provide investigators with the understanding of how reactions occur and allow engineers to develop new materials to improve the efficiency of industrial processes.

Chapter 1 – Introduction

1.1 Outline

This chapter explains surface science used in this thesis. Section 1.2 discusses the importance of surface science and ongoing challenges in heterogeneous catalysis research. A traditional surface science study investigating adsorbate structure on metal surfaces is presented in Section 1.3. In Section 1.4, different methods for thin film deposition are introduced. Finally, Section 1.5 introduces the hydrogenation of propyne over Pd/Cu single atom alloy catalysts.

1.2 Background

Heterogeneous catalysis is used in many industrial chemical processes, and all processes occur on catalyst surfaces. For decades, surface science research used highly ordered catalyst surfaces, such as the (111) facet of transition metals, to understand how these processes occur so that these catalysts can be optimized for selectivity and activity. Traditional surface science experiments are generally performed at ultrahigh vacuum (UHV) with pressures on the order of 10^{-10} Torr to maintain a chemically clean environment. There are many surface sensitive spectroscopic techniques including but not limited to X-ray photoelectron spectroscopy (XPS), Auger electron spectroscopy (AES), reflection absorption infrared spectroscopy (RAIRS), and temperature programmed desorption (TPD). In addition, there are surface imaging techniques such as low energy electron diffraction (LEED), scanning tunneling microscopy (STM), and atomic force microscopy (AFM). These techniques allow researchers to identify the properties of various surfaces; however, most of these techniques require UHV conditions.

Industrial processes, however, occur at high pressures with multi-faceted catalyst surfaces. While traditional studies offer great insight, the findings may not always hold true under industrial conditions. The differences between the fundamental research and industrial applications are commonly called the pressure and materials gaps in surface science. As technology progresses, scientists and engineers develop techniques that could provide the desired information from UHV studies under industrial reaction conditions. These techniques are called ambient pressure (AP) techniques since they are not restricted to UHV conditions. This dissertation focuses on the versatility of infrared spectroscopy as it is applied in the characterization of small molecules on transition metal surfaces, thin film analysis, and ambient pressure chemical reactions in conjunction with other UHV analytical methods.

1.3 Reactions of HCN

The adsorption and reactions of hydrogen cyanide on transition metal surfaces have been widely studied. These studies have been motivated in part by the relevance of the surface chemistry of molecules containing CN bonds to various areas of heterogeneous catalysis. At a more fundamental level, as a relatively small molecule that is isoelectronic with the prototypical molecular adsorbate CO, HCN offers an opportunity for a detailed mapping of its bonding structure and reaction pathways by both experimental and theoretical methods. Here we present a study that combines surface vibrational spectroscopy with density functional theory calculations of HCN interaction with the Pd(111) and Ru(001) surfaces. The present study was motivated in part by the marked contrast in the reported structure and reactions of HCN on Pd(111) with those on Pt(111). Kordesch et al. observed a vibrational loss with high resolution electron energy loss spectroscopy (HREELS) at 1540 cm^{-1} following HCN adsorption on Pd(111) at 300 K (4,5). This frequency is characteristic of a C=N double bond from which they concluded that HCN bonds to the surface in a di-σ configuration with the C=N bond parallel to the surface. A NEXAFS study confirmed this orientation for the CN bond (4).

In a series of papers (6–11), we have used the technique of reflection absorption infrared spectroscopy (RAIRS) to investigate the structure and reactions of HCN on Pt(111). At a temperature of 85 K, we found that HCN adsorbs molecularly with the axis oriented perpendicular to the surface. This was based on the strong similarity of the infrared spectrum of the absorbed molecule to that of gas phase HCN. In particular, the CH stretch of HCN on Pt(111) was observed at 3298-3000 cm^{-1}, compared to values of 3311-3312 cm^{-1} in the gas phase(12,13) and 3305-3306 cm^{-1} in an argon matrix (14,15). As the C–H

stretch frequency is a sensitive indicator of the hybridization on the C atom, the observed value indicates that the adsorbed molecule retains a CN triple bond. The CN stretch is very weak for HCN on Pt(111), which is also characteristic of the gas phase and matrix-isolated molecule. For HCN adsorbed with a perpendicular orientation, the CH and CN stretches would be surface IR allowed but the bending mode would be forbidden. The latter occurs at 712 cm^{-1} in the gas phase (12,13), which was below the low wavenumber cutoff in our RAIRS studies. However, we detected a peak at 1311 cm^{-1} that we assigned to the overtone of the bending fundamental. This overtone is observed at 1411 cm^{-1} in the gas phase and at 1425 cm^{-1} in an Ar matrix. The bending mode is presumably shifted to a lower value when the molecule is bonded to the surface. These spectral characteristics of HCN adsorbed at low temperature on Pt(111) led us to conclude that the molecule bonds to a Pt atom through the nitrogen lone pair in a perpendicular orientation.

When HCN is adsorbed on Pt(111) at low temperature and then warmed to 300 K, pronounced changes are observed in the RAIR spectra. The bands associated with HCN are replaced with ones at 3363, 1567, and 1323 cm^{-1}, which were assigned to an NH_2 symmetric stretch, a NH_2 scissor mode, and a C=N stretch, respectively, of an aminocarbyne (CNH_2) species (6). These assignments were supported by observing isotopic shifts after adsorbing $H^{13}C^{14}N$ and $H^{12}C^{15}N$. Subsequent density function theory calculations based on small Pt cluster models of the Pt(111) surface were used to accurately simulate the observed RAIR spectrum and isotopic shifts of aminocarbyne on Pt(111) (16). Other theoretical calculations showed that aminocarbyne is a stable species on Pt(111) and that it bonds with the CN axis perpendicular to the surface (17,18). In independent work,

aminocarbyne has also been identified as a stable intermediate on Rh(111) in the decomposition of methyl amine (19) and azomethane (20).

The previous work arguing that HCN adsorbs on Pd(111) at 300 K with a CN double bond parallel to the surface did not consider the possibility of reaction to form a new chemical entity, such as CNH_2. The present study is designed to determine if HCN displays qualitatively different behavior on Pt(111) and Pd(111), as suggested by past studies. By observing with RAIRS small isotopic shifts with ^{13}C and ^{15}N substitution, we show that CNH_2 does indeed form on Pd(111). Furthermore, our DFT calculations show that CNH_2 is stable over a wide temperature range on Pd(111) just as it is on Pt(111). Following the low temperature adsorption of HCN on Pd(111), peaks are observed at 3301 and 1641 cm^{-1}. While the peak at 3301 cm^{-1} is unambiguously assigned to the CH stretch of a triply bonded carbon atom, the 1641 cm^{-1} peak could be plausibly assigned to either a C=N stretch or to the overtone of the bending mode. Although either assignment is qualitatively consistent with the observed shifts with ^{13}C and ^{15}N substitution, the magnitude of the shifts is more consistent with the bending overtone. We therefore find no evidence for a di-σ-bonded HCN species on Pd(111).

On the Ru(001) surface, no RAIR peaks are observed after annealing the surface to temperatures of 150 K or higher. From this observation, we conclude that HCN dissociates completely to atomic H, C, and N. At the other extreme of reactivity, on Cu(100), HCN was found to desorb molecularly without reaction. Based on the similarity of the low temperature and low coverage RAIR spectra for HCN on Pt(111), Pd(111), Ru(001) and Cu(100), we conclude that HCN can adsorb in a common metastable form on these surfaces that is independent of its subsequent reactive chemistry.

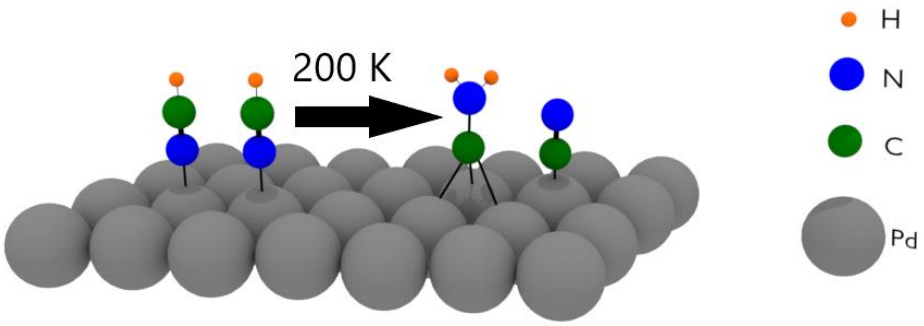

Figure 1 HCN bonds to the Pd(111) surface through the N lone pair electrons. When heated to 200 K, the adsorbed HCN molecules transform into aminocarbyne (-CNH_2) via a bimolecular mechanism

1.4 Deposition of V_2O_5 thin films

The wide range of oxidation states of vanadium among its oxides and the ability to switch between these multiple oxidation states from V^{5+} (V_2O_5) to V^{2+} (VO) gives the vanadium oxides vast potential in heterogeneous catalysis. Oxide supported V_2O_5 catalysts have been applied in industrial catalytic processes for decades, such as the oxidation of SO_2 to SO_3 in the production of sulfuric acid, the oxidation of *o*-xylene to phthalic anhydride, and the reduction of NO_x with NH_3 to N_2 (21–23). In recent years, they have also been promoted for oxidative desulfurization (ODS) in oil refining (24).

V_2O_5 has also attracted great interest in electrochemistry due to its multiple accessible vanadium oxidation states and layered structure. Carbon-coated V_2O_5 nanocrystals have been investigated as a high performance cathode material for Li-ion batteries (25). In addition, V_2O_5 gels are considered as a promising cathode material for rechargeable Mg batteries, which is a competitive alternative to Li-ion batteries (26).

To understand the basic structural and electronic properties of V_2O_5 and its interfacial behavior in both catalysis and electrochemistry, investigation of well-defined and characterized model systems is highly desirable. The preparation of model V_2O_5 surfaces is therefore of great interest. V_2O_5 single crystals generally exhibit surface charging problems in spectroscopic measurements, thus various methods have been used in an attempt to grow V_2O_5 thin films, which can be summarized into three categories. The first approach is the oxidation of vanadium during or following vanadium metal deposition (27–35). Netzer and co-workers (27–29) applied reactive evaporation of vanadium onto Pd(111) in 2×10^{-7} mbar of O_2, but could only achieve mainly a stoichiometry of V_2O_3. Wong et al. (30,31) studied the post-oxidation of vapor-deposited vanadium on CeO_2(111) and TiO_2(110) by X-ray photoelectron spectroscopy (XPS). They found on both surfaces that the oxidation in 10^{-7} Torr of O_2 produces primarily V^{3+}, while oxidation in 10^{-3} Torr of O_2 yields primarily V^{5+}, though it is always accompanied by some V^{4+} species. Guimond et al. (34,35) reported the first and only growth of well-ordered V_2O_5(001) thin films on Au(111), however it requires post-oxidation of vanadium layers under an oxygen flow of 50 mbar in a high pressure cell, which is not suitable for common UHV systems.

Chemical vapor deposition has also been used to prepare V_2O_5 thin films. Wang and Madix (36) simultaneously dosed $VOCl_3$ (5×10^{-7} Torr) and water (5×10^{-6} Torr) onto a TiO_2(110) surface at room temperature and produced sub-monolayer to multilayer V_2O_5 thin films as verified by XPS. However, this method also must be carried out in a high-pressure preparation chamber attached to a UHV system.

Another approach is physical vapor deposition from a V_2O_5 source. Silversmit et al. (37) prepared fully oxidized V_2O_5 up to 30 Å in thickness on a TiO_2(001)-anatase substrate with reactive DC magnetron sputtering of a polycrystalline V_2O_5 target in 1 Pa of flowing O_2. In another

attempt, Julien et al. (38,39) applied flash evaporation of V_2O_5 powder to grow amorphous V_2O_5 films on silicon substrates at room temperature, however the stoichiometry of the as-grown films was not characterized. Ramana et al. (40) have grown V_2O_5 thin films on glass and Si(100) substrates at room temperature by the evaporation of V_2O_5 powders in a molybdenum crucible in high vacuum (10^{-6} Torr). The authors found that the as-grown films are nearly stoichiometric V_2O_5 as indicated by XPS and electron probe micro-analysis (EPMA) and are completely amorphous at room temperature. However, the V_2O_5 source temperature was not mentioned. Wu et al. (41–43) have deposited V_2O_5 thin films on highly ordered pyrolytic graphite (HOPG) at room temperature by the evaporation of V_2O_5 powders in a boron nitride crucible in UHV, with the source temperature at 670 °C. Amorphous, nearly stoichiometric V_2O_5 thin films were identified by XPS, ultraviolet photoelectron spectroscopy and low energy electron diffraction (LEED). However, a small amount of V^{4+} species is always present at various coverages as revealed by XPS, which suggests a slight reduction of V_2O_5 during the deposition process.

Although most successful cases of growth of stoichiometric V_2O_5 thin films were carried out under extreme conditions for a UHV system – either ambient pressure oxidation treatment, or high-pressure water vapor dosages – direct evaporation from V_2O_5 powder offers an attractive alternative method for surface science studies in UHV. Here we demonstrate the successful growth of stoichiometric V_2O_5 thin films on Pd(111) by this method and have characterized the films with XPS, reflection absorption infrared spectroscopy (RAIRS) and LEED. By growing the V_2O_5 films on a Pd(111) substrate by this physical vapor deposition (PVD) method, we are able to make a direct comparison with the extensive existing literature on the growth and characterization of vanadium oxides on Pd(111) by other methods.

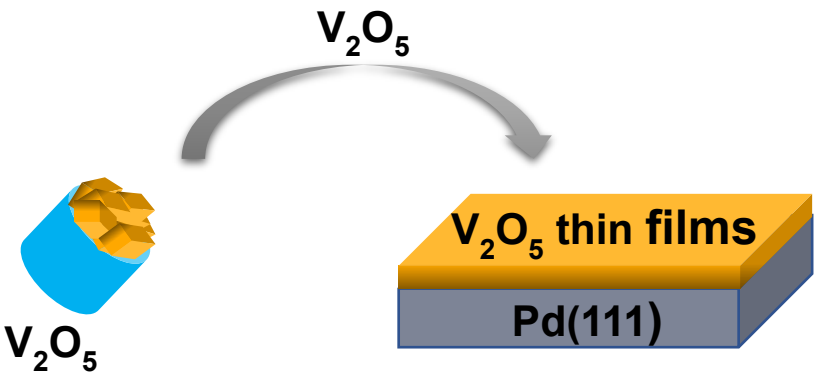

Figure 2 V_2O_5 thin films were grown on Pd(111) by PVD under UHV conditions. V_2O_5 retains its stoichiometry upon deposition, eliminating the need for oxidative environments or multistep CVD processes.

1.5 Oxidative desulfurization of dibenzothiophene with V_2O_5 thin films on Pd(111)

Impurities in crude oil distillates increase the difficulty of achieving clean fossil fuels. Among the impurities, sulfur is the most hazardous. Oxidative desulfurization (ODS) has garnered much attention since the mid-2000's as the desire to lower environmental impact increases (44). Oxidative desulfurization is the process of converting sulfur from an aromatic species to a sulfone species. Thiophene (C_4H_4S) is the simplest aromatic sulfur-containing compound, and dibenzothiophene ($C_{12}H_8S$, DBT) is a common impurity in oil refining.

Oxidative desulfurization of dibenzothiophene has been achieved under harsh oxidative conditions using either ozone and H_2O_2 mixtures as an advanced oxidation process in ionic liquids (45). Other desulfurization methods include hydrodesulfurization (HDS) which uses hydrogen to remove sulfur from organic compounds. However, for HDS to be effective, severe conditions are required which leads to high operating costs. ODS offers an alternative by eliminating the need for H_2 and oxidizing DBT and its derivatives under milder conditions (46–48).

More recently, the use of transition metals to catalyze the ODS process to avoid using harsh chemicals such as ozone, which can corrode equipment or oxidize hydrocarbons. Tomskii et al. (49) investigated the feasibility of ODS using a mixture of vanadium and molybdenum oxide catalysts. Cedeño-Caero et al. (50) investigated the effect of supports on vanadium based catalysts. Here we investigated the oxidative desulfurization of DBT using V_2O_5 thin films grown on Pd(111).

1.6 Partial hydrogenation of propyne over Pd/Cu(111)

Alkenes are desired for their use in polymers such as polystyrene, polyvinyl chloride, polypropylene, etc. For alkenes to be used in polymers, they must be obtained without impurities. Alkyne impurities affect the polymerization reaction and the properties of the polymers (51). Alkynes must be removed from the alkene feed for polymer manufacturers to better control their processes. The most efficient removal technique is the partial hydrogenation of the alkyne thereby converting an impurity into a desired compound.

Selective hydrogenation of alkynes to alkenes is plagued by the competing reactions of polymerization and further hydrogenation of the alkene product to form alkanes. Therefore, the ideal catalyst would be able to inhibit polymerization and alkene hydrogenation. Current hydrogenation catalysts mainly consist of Pd or Pt due to their ability to facilitate H_2 activation; however, to enhance selectivity to the alkene, CO must be introduced with the reaction mixture (52–54). Unfortunately, Pd and Pt catalysts are easily coked by CO, which decreases the catalyst lifetime.

Pd and Pt catalysts can be avoided by using other transition metals such as copper. Aside from being less expensive and more abundant than the precious metals, copper is more selective for hydrogenation to alkenes. However, copper cannot activate H_2 near room temperature.

Without H_2 activation, oligomerization of the alkyne is a major competitor (55). Altering the catalyst structure prevents oligomerization and promotes alkene desorption. However, altering the structure involves using high pressures of CO to rearrange the copper atoms (56,57). Alkyne hydrogenation requires a catalyst that is selective for alkene production and resistant to coking by CO or hydrocarbons.

To provide a selective coke-resistant catalyst to produce alkenes, single atom alloy (SAA) catalysts have grown more popular. SAA catalysts take advantage of facile H_2 dissociation on the active site, typically isolated platinum or palladium atoms, and the selectivity of the transition metal host to enhance the selectivity and longevity of the catalyst (58).

The hydrogenation of acetylene over Pd/Cu SAA catalysts demonstrated a high selectivity for ethylene with large turnover frequencies (TOFs) (59). Acetylene is the simplest alkyne and useful for fundamental studies; however, there have been relatively few studies of propyne hydrogenation over SAA catalysts despite its significant practical importance.

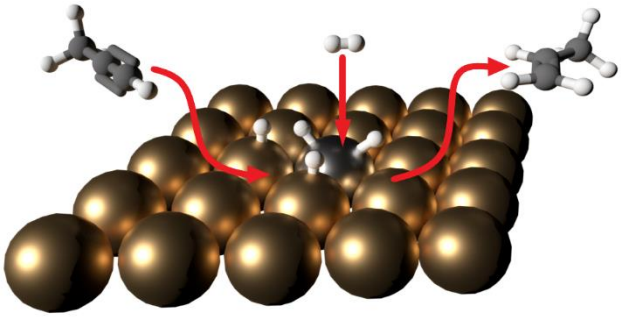

Figure 3 Hydrogenation of propyne (C_3H_4) to propylene (C_3H_6) occurs at ambient temperatures over the SAA Pd/Cu(111) surface. The hydrogenation is facilitated by H_2 dissociation at the Pd (silver colored) sites followed by H addition to C_3H_4 at nearby Cu (bronze colored) sites. C_3H_6 readily desorbs from the SAA surface inhibiting polypropylene formation.

In one propyne hydrogenation study, the optimal Cu:Pd ratio, H_2:C_3H_4 ratio, and reaction temperature were determined (60). While McCue et al. were able to optimize the reaction conditions, they did not study the reaction kinetics (60). In other cases, the kinetics of propyne hydrogenation have been studied over pure metal and supported metal catalysts (61–64). Mann and Khulbe, in a multipart study, determined the reaction's dependence on reactant pressure and its activation energy over different catalysts (61–63). In the present study, we present results on the hydrogenation of propyne over a well-characterized Pd/Cu(111) SAA catalyst. The kinetics of the reaction were determined by monitoring the gas phase reactant and product concentrations based on selected infrared absorption peaks.

Chapter 2 – Instrumentation

2.1 Outline

This chapter introduces the instrumentation used throughout the thesis. The two UHV chambers on which experiments were performed are detailed in Section 2.2. The first UHV chamber is referred to as the XPS system, and the second chamber is referred to as the AP-RAIRS system. Section 2.3 describes experimental operations and catalyst preparation methods. Finally, the major experimental techniques are explained in Section 2.4.

2.2 Ultrahigh Vacuum Chambers

2.2.1 XPS System

The XPS system was used to conduct experiments for "Deposition and characterization of V_2O_5 thin films on Pd(111)" (2) and the Pd based experiments for "Reaction pathways for HCN on transition metal surfaces" (1). This UHV chamber contains a UTI 300C quadrupole mass spectrometer, Mattson Research Series 10000 FTIR, Princeton Electronics reverse view LEED, PHI 04-161 sputter ion source, and a VG Scientific X-ray photoelectron spectrometer equipped with dual anode Mg/Al X-ray source and CLAM 2 hemispherical analyzer. This chamber is maintained at a base pressure of $<1\times10^{-10}$ Torr with a Balzers TMU 520 turbomolecular pump backed by a Leybold TriVac D4B series rotary vane pump.

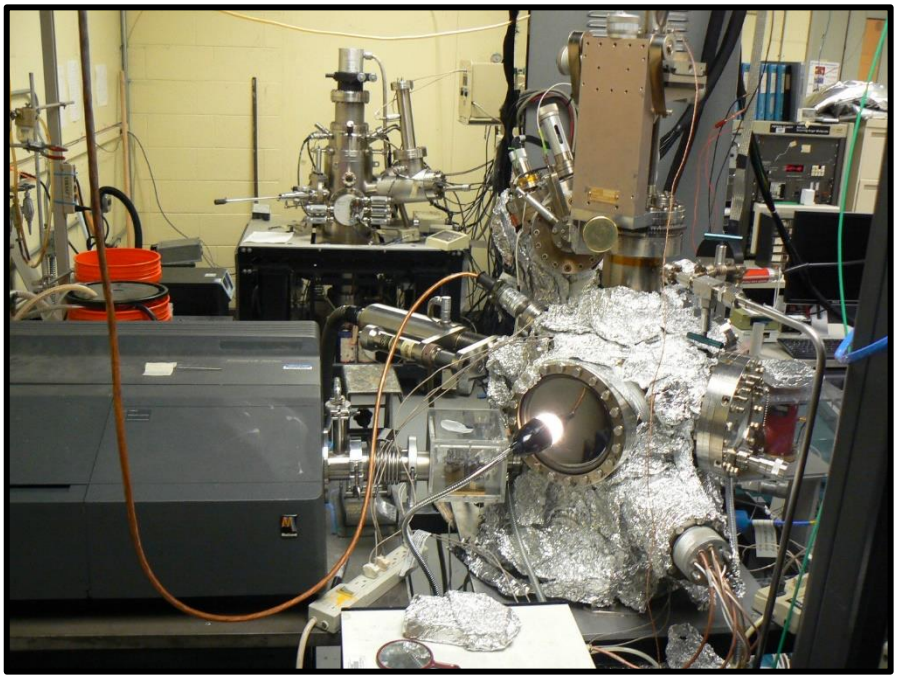

Figure 4 A photograph of the XPS system (foreground) and a PHI 600 Scanning Auger Multiprobe (background)

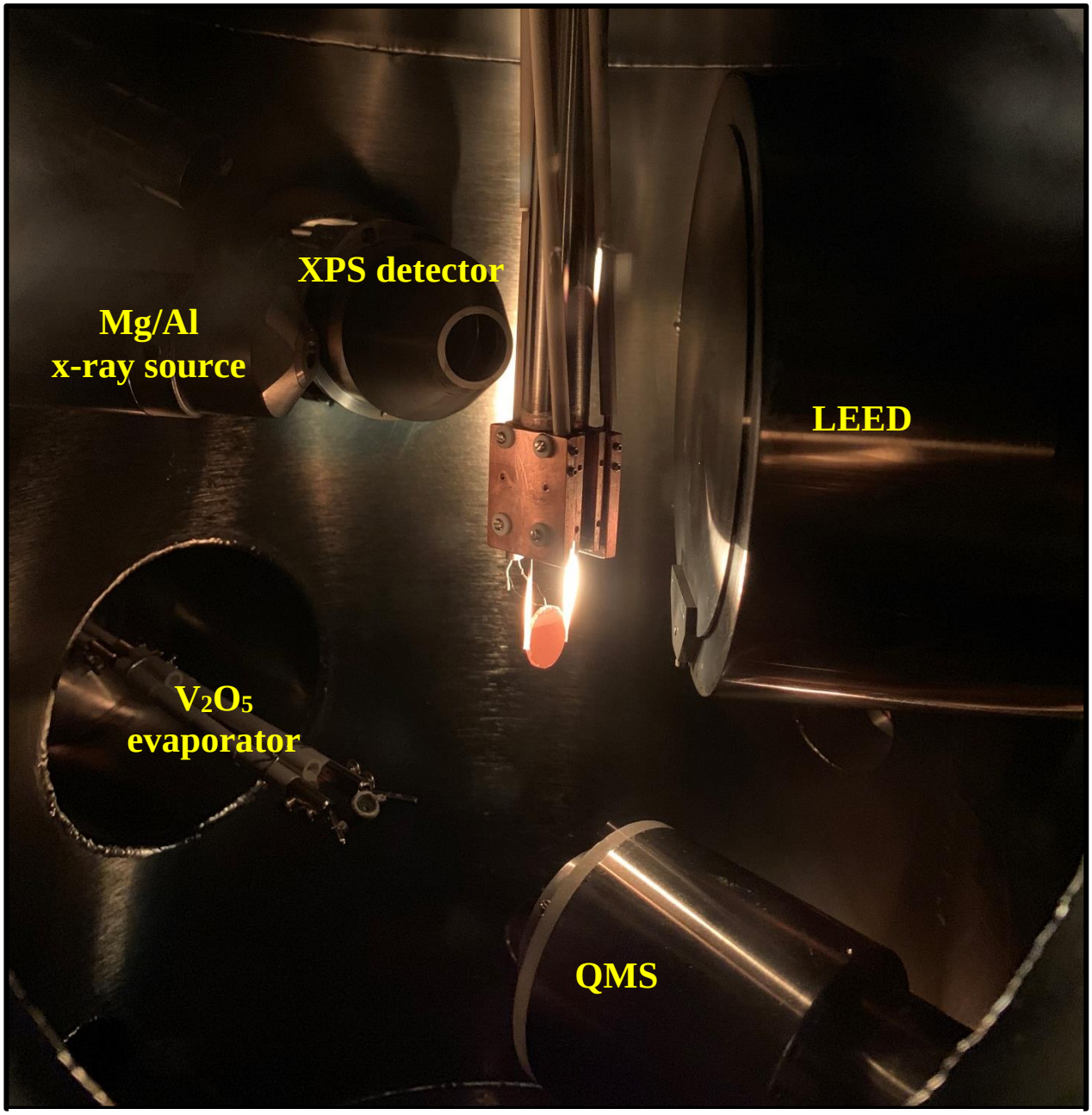

Figure 5 A photograph of XPS-system interior while annealing the Pd(111) at 1200 K

The UHV chamber is shown in Figure 4. A Pd(111) crystal was installed for all experiments performed with this system. The crystal was spot-welded to two tantalum wires, as shown in Figure 5, mounted on an electrical feedthrough for direct heating up to 1200 K and liquid nitrogen cooling to 90 K. A type K thermocouple junction was spot-welded to the top of the crystal for temperature measurement using a Eurotherm 2416 PID controller. An evaporator for V_2O_5 deposition was built from an electrical feedthrough (Kurt J. Lesker) with an alumina coated tungsten crucible (Midwest Tungsten) spot welded to vacuum side terminals, also shown in Figure 5. A type K thermocouple junction was fixed to the bottom of the crucible with Aremco Ceramabond cement. The Pd(111) surface was cleaned by Ar^+ ion sputtering (5μA, 1.0 kV) and annealing (1200 K, 2 min). The surface was determined to be clean when no carbon or oxygen XPS features were detected. Alternatively, the surface was prepared by oxidative treatment with 1.0×10^{-7} Torr of O_2 (1000 K, 30 min) and was determined to be clean when water or oxides of carbon were not detected by O_2 TPRS.

2.2.2 AP-RAIRS System

The AP-RAIRS system was used to conduct experiments for "Propyne hydrogenation over Pd/Cu(111) single atom alloy catalysts studied with ambient pressure infrared spectroscopy" (3). This system is unique because it allows traditional UHV characterization of surface catalyzed reactions as well as ambient pressure infrared spectroscopy to provide information about the catalyst activity under reaction conditions that more closely resemble industrial practices. The upper portion is a stainless steel UHV chamber which houses a Pfeiffer Prisma quadrupole mass spectrometer, PHI 04-161 sputter ion source, an LK Technologies RVL 2000 Auger/LEED instrument with a mini-CMA analyzer for Auger electron spectroscopy, and a home-built metal evaporator used for Pd deposition. The AP-RAIRS chamber is shown in Figure 6. The lower

portion of the chamber is used for RAIRS analyses and can be sealed from the upper portion and pressurized up to atmospheric pressures. A Bruker Vertex 70v FTIR spectrometer equipped with a liquid N_2 cooled MCT external detector allows for RAIRS experiments under UHV or ambient pressure conditions. This system is maintained at a base pressure of 1×10^{-9} Torr with a Pfeiffer TMU 261 turbomolecular pump backed by a Pfeiffer rotary vane pump. Additional pumping is provided by a Varian diode ionization pump and a titanium sublimation pump.

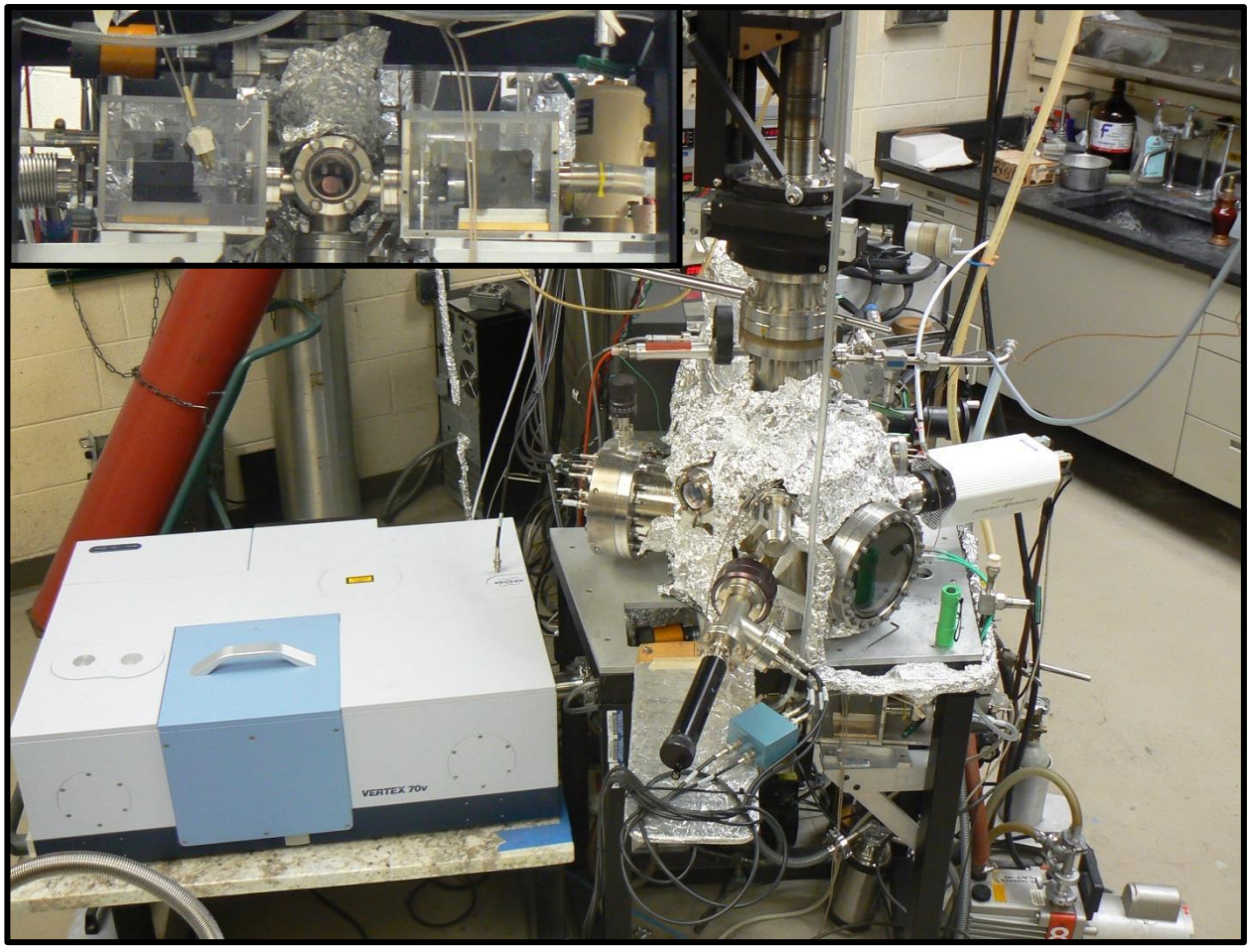

Figure 6 A photograph of the AP-RAIRS system. Inset: a photograph of the Cu(111) crystal in the ambient pressure IR cell

A Cu(111) crystal was mounted by inserting two tantalum wires through the crystal. These wires allow for direct heating of the crystal. A type K thermocouple junction was placed in a hole at the top of the crystal for temperature measurement up to 1000°C with a Watlow EZ-Zone PID controller. The Cu(111) surface is prepared by Ar^+ ion bombardment (10μA, 1 kV) followed by annealing (950 K, 10 min). The surface is analyzed by AES and determined to be clean when only the Cu AES features are present in the spectrum. Alternatively, a LEED image showing a 1×1 pattern indicates a contaminant-free surface. The procedure for Pd deposition was outlined by the Sykes group at Tufts University (65). Pd is deposited on the Cu(111) surface by heating a Pd filament to 900°C with the Cu(111) crystal held at 108°C to prevent agglomeration of the Pd atoms on the surface.

2.3 Instrument Operations

2.3.1 XPS System

A typical UHV experiment performed on the XPS system involves first positioning the Pd(111) crystal for the appropriate analysis method using the four-coordinate manipulator to which the crystal is attached. Then the crystal is heated to 1200 K while degassing the necessary filaments for the analytical instrument. Once the crystal has cooled back to room temperature, it is further cooled to 90 K by slowly filling the manipulator with liquid nitrogen. The crystal is again rapidly heated to 1200 K to remove any contaminants, nominally CO, that may have adsorbed to the surface during the cooling process. The crystal is subsequently cooled back to 90 K by adding liquid nitrogen to the manipulator as needed. Once the crystal has reached a temperature of 90 K, a background spectrum (diffraction pattern if using LEED) is collected with the desired instrument (XPS, RAIRS, or QMS). After the background is collected, the test gas is admitted into the chamber by a precision leak valve. Once the desired exposure of test gas in

Langmuir units (L, 1 L = 1×10^{-6} Torr·s) is admitted, the leak valve is closed, and sample spectra are collected after allowing the chamber pressure to return to its base level.

2.3.2 AP-RAIRS System

Experiments conducted in the AP-RAIRS system are typically carried out at or above room temperature. First the Cu(111) is annealed at 950 K in the analysis chamber under UHV while the desired instrument filament is degassed. When the Cu(111) crystal has cooled back to room temperature, the crystal is positioned for the desired operation. A background spectrum is collected from the clean Cu(111) surface, then the test gas is admitted into the chamber by a precision leak valve. Once the desired exposure of the test gas is admitted, the leak valve is closed and sample spectra are collected once the chamber pressure returns to its base level.

Ambient pressure RAIR experiments are conducted by first annealing the Cu(111) crystal at 950 K then positioning the crystal in the IR cell after it has cooled to room temperature. The pneumatic 8-inch gate valve between the analysis chamber and the turbomolecular pump is then closed and the MCT detector is cooled with liquid N_2. The crystal and detector positions are modified empirically to maximize the signal intensity on the computer. Once the positions are optimized, a background spectrum is collected followed by a sample spectrum of the clean surface. After the sample spectrum is acquired, the angle valve between the IR cell and the turbomolecular pump is closed so that the IR cell can be pressurized up to atmospheric pressures for desired reactions. After the experiment, the IR cell is evacuated by opening a Swagelok bellows-sealed valve to a mechanical pump. When the pressure in the IR cell reaches 0.01 Torr, the bellows-sealed valve is closed and the angle valve to the turbomolecular pump is slowly opened. The IR cell is evacuated overnight before opening the pneumatic 8-inch gate valve between the main chamber and the turbomolecular pump. After the IR experiments, it is common to conduct AES

or TPD experiments to characterize residual compounds that may be on the surface after ambient pressure experiments.

2.4 Analytical Methods

2.4.1 Reflection Absorption Infrared Spectroscopy

2.4.1.1 Theoretical Principles

Infrared (IR) spectroscopy is a powerful tool for identifying chemical bonds and functional groups. The frequency of IR light is on the same order as molecular vibrational energy; thus, a molecule's vibrational energy states can be studied with IR spectroscopy. This technique can be used both qualitatively and quantitatively for molecular entities and a large range of temperature and pressure. The versatility of IR spectroscopy is also seen in surface science. A type of IR spectroscopy termed reflection absorption infrared spectroscopy (RAIRS), also referred to as infrared reflection absorption spectroscopy (IRRAS or IRAS), takes advantage of this versatility and can be applied from UHV conditions to ambient pressures. In RAIRS studies on metal surfaces, only vibrations with a component of the transition dipole moment parallel to surface normal are observed (66). This selection rule, illustrated in Figure 7, is due to the image dipole of the molecule produced by the metal surface. The *p*-polarized component of the incident IR beam interferes constructively with its reflection; conversely, the *s*-polarized component interferes destructively with its reflection. Under UHV conditions, *p*-polarized light will give spectra of adsorbed species only. At ambient pressures, vibrations from gas phase and adsorbed molecules will be detected with *p*-polarized light, and *s*-polarized light will detect only gas phase vibrations. Subtracting the *s*- polarized RAIR spectra from the *p*-polarized RAIR spectra will provide vibrational information about the adsorbed molecules at ambient pressures. This adaptation of RAIRS is termed polarization dependent reflection absorption spectroscopy (PD-RAIRS).

Through PD-RAIRS, industrial reactions can be more accurately studied in academic environments.

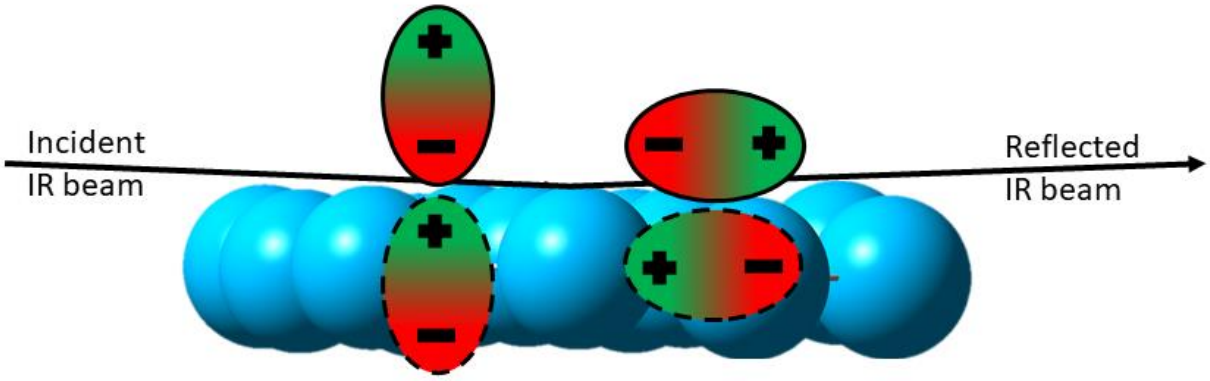

Figure 7 The metal surface selection rule for RAIRS. The adsorbate dipole moment (solid outline) and the surface image dipole (dashed outline) combine constructively when perpendicular to the surface but destructively when parallel to the surface.

2.4.1.2 Instrumentation

Modern infrared spectrometers have the same basic design as developed by Albert Abraham Michelson in 1887 (67). They are composed of the following components: an infrared source, a beamsplitter, a moving mirror, a stationary mirror, a sample compartment, and a detector. The source emits infrared radiation, which is focused by a mirror toward a beamsplitter. The beamsplitter separates the IR beam so that some of the beam reflects off a stationary mirror and the rest reflects off a moving mirror. When the two reflected beams recombine, they will interfere constructively or destructively with each other based on the position of the moving mirror at the

time of reflection. The recombined beam is directed by mirrors to a sample compartment, passes through the sample, and interacts with the detector. The resulting interferogram is processed with software that performs a Fourier transform to convert the interferogram into a typical transmittance or absorbance Fourier transform infrared (FTIR) spectrum. For RAIRS studies, a polarizer is inserted between the sample and the detector to select for *p* polarized light as shown in Figure 8. This allows the user to collect spectra of adsorbate species. In PD-RAIRS, the polarizer is rotatable to select for *p* or *s* polarized light.

Interpreting FTIR spectra presents its own challenges. There is usually interference from water vapor and CO_2 present in the atmosphere. To remove these contaminants, the spectrometer and associated optics must be under a vacuum or in an inert atmosphere. The former is easily done with roughing pumps such as rotary vane or scroll pumps. The latter can be done by passing compressed air through a series of desiccants to remove water and CO_2 and admitting the dry air into the spectrometer optics array. Other challenges arise from differences between background and sample spectra. These differences can lead to artefacts in the FTIR spectra which may overlap with anticipated peaks. To overcome this challenge, the spectra should not be collected shortly after evacuating or purging atmospheric gases from the system. Typically, after maintenance, the user allows the system to equilibrate overnight so that there will be no significant changes between background and sample spectra.

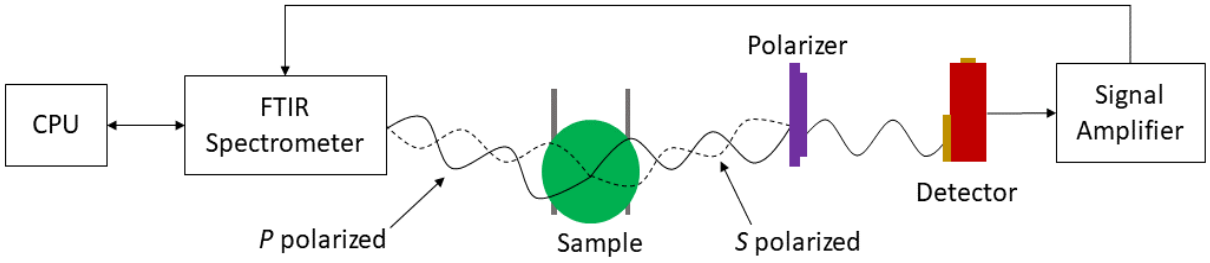

Figure 8 Block diagram of RAIRS instrument with an external detector. The polarizer rotates to select for *p* or *s* polarized light in PD-RAIRS.

2.4.2 X-ray Photoelectron Spectroscopy

2.4.2.1 Theoretical Principles

X-ray photoelectron spectroscopy (XPS), also known as electron spectroscopy for chemical analysis (ESCA), is a surface sensitive elemental analysis technique. X-rays bombard a sample providing electrons with enough energy to escape the sample surface. The ejected electrons are termed photoelectrons. The kinetic energy of the photoelectron in vacuum depends on the binding energy of the electron, the energy of the incident photon, and the work function of the sample analyzed. This is described in equation 2.1 where $h\nu$ is the photon energy, BE is the binding energy of the photoelectron, and φ is a combination of the material work function and spectrometer work function.

$$KE = h\nu - BE - \phi \qquad \text{Equation 2.1}$$

It is common to present photoemission spectra in terms of binding energy by rearranging equation 2.1 as follows:

$$BE = h\nu - KE - \phi \qquad \text{Equation 2.2}$$

Expressing the electron energy in terms of binding energy is more practical than kinetic energy because an electron's binding energy is determined by its chemical environment. For example, a 2p electron of Fe (720 and 707 eV) will have a lower binding energy than a 2p electron of Cu (953 and 933 eV) (68). The binding energy of the photoelectron changes with an element's oxidation state. Higher oxidation states result in higher binding energies, thus providing crucial information about elemental composition. For example, the C 1s XPS peak for graphitic carbon is 284.5 eV; however, the binding energy shifts to 288.5 eV in CO_2 (69). The X-ray photoemission spectrum can also indicate the relative abundance of elements in a sample by taking the ratio of the major peak intensities for each element after correcting for sensitivity factors (70).

XPS is a surface sensitive technique and can analyze thin films of up to approximately 10 nm thick. Although the X-ray penetration depth is much larger than 10 nm, the sensitivity is limited by the inelastic mean free path (IMFP) of the photoelectron. Deeper electrons can be scattered and lose energy. If the energy of the scattered electron is less than the work function, the electron will not be detected as it cannot leave the sample. The depth of detected electrons, and subsequently film thickness, can be determined by equation 2.3 where I_0 is the intensity of an electron at depth *d*, I_S is the intensity of the same electron when it reaches the sample surface, and λ is the inelastic mean free path (IMFP) of the electron.

$$I_s = I_0 e^{-d/\lambda} \qquad \text{Equation 2.3}$$

Electrons in the same orbital have slightly different energies due to spin-orbit coupling. Spin-orbit coupling is due to the magnetic moment due to electron spin interacting with the magnetic field produced by the orbiting electrons The magnitude of the energy change depends on three angular momenta: orbital (*l*), spin (*s*), and total (*j*) angular momenta (71). Spin-orbit coupling is observed in X-ray photoelectron spectra if the resolution of the analyzer is within the

magnitude of spin-orbit interactions. For example, the S $2p_{1/2}$ and $2p_{3/2}$ peaks are separated by 1.18 eV and have a significant overlap. The peaks are labeled by the convention nl_j where n is the principal quantum number, l is the orbital angular momentum quantum number, and j is the total angular momentum quantum number. The total angular momentum, j, is calculated by equation 2.4 where s is the spin quantum number of an electron.

$$j = l + s \qquad \text{Equation 2.4}$$

For example, the Pd 3d peaks would be labeled as $3d_{3/2}$ and $3d_{5/2}$. These peaks have a specific intensity ratio with the larger spin state having a greater intensity than the lower spin state. The intensity differences reflect the number of m values for a given j. The z-component component of the angular momentum vector is given by quantum number m. The number of m states for a given j is provided by equation 2.5:

$$m = 2j + 1 \qquad \text{Equation 2.5}$$

When interpreting a spectrum, there are many features that must be addressed. These include ghost peaks, satellite peaks, plasmon energy loss features, shake up and shake off effects, photon-induced Auger peaks, and a rising secondary electron background. These features convolute the spectrum and can lead to quantification errors, false positive or false negative results.

Ghost peaks arise from worn or contaminated X-ray sources. In common Mg/Al dual anode systems, a ghost peak can be identified if a peak of the same shape is found at a binding energy that is shifted by the difference in the photon energy. A Mg Kα source provides photons with an energy of 1253.3 eV, and an Al Kα source provides photons with an energy of 1486.6 eV. A minor peak in a spectrum collected with an Al Kα photon that appears at a position 233.3 eV less than its major peak may be attributed to Mg contaminants on the Al anode.

Satellite peaks arise from polychromatic X-ray sources. A Mg Kα source could emit $K\alpha_1$, $K\alpha_{2,3}$ and Kβ photons. These photons cause peaks to appear at positions corresponding to the difference between the undesired photon energy and the desired $K\alpha_1$ energy. These energy differences and relative intensities are typically provided in a reference book such as *Handbook of X-ray Photoelectron Spectroscopy* from Perkin-Elmer Corporation (68).

Some materials can exhibit plasmon loss peaks. Plasmon loss peaks are a result of the photoelectron losing energy to the host material. This feature is typical in conducting materials such as metals and its intensity varies by material. Shake up peaks are due to an element remaining in an excited state after photoemission occurs. Shake down effects result from valence electron emission after the core level photoelectron is ejected. Shake up peaks appear as separate smaller peaks at a higher binding energy than the parent peak. Shake off features broaden the parent photoemission peak. Auger peaks are due to an electron being emitted by energy released from another electron relaxing to fill a core level vacancy. Auger peaks are described in greater detail in Section 2.4.3.

2.4.2.2 Instrumentation

An XP spectrometer, illustrated in Figure 9, consists of the following components: an X-ray source, an analyzer, and an electron multiplier. Optional components include an X-ray monochromator and an electrostatic lens. Traditional XPS instruments have twin anode polychromatic x-ray sources. These sources typically provide Mg Kα or Al Kα X-rays. The X-rays are produced when electrons emitted from a filament strike a Mg or Al coated anode. The anode core electrons are ejected causing higher energy electrons to relax and emit a photon in the X-ray region of the electromagnetic spectrum. This type of X-ray source is polychromatic because there are different X-rays emitted from the same material. For example, a Mg source primarily

emits X-rays from the $K\alpha_1$ relaxation; however, $K\alpha_{2,3}$ and $K\beta$ relaxations also occur producing X-rays of slightly different energies. Having X-rays of different energies exciting a sample limits the resolution of the spectra. To improve the resolution, a monochromator can be installed between the source and the sample to disperse the polychromatic beam and align the photon of interest with the sample.

The two main types of analyzers in XPS instruments are cylindrical mirror analyzers (CMA) and hemispherical analyzers. The CMA is made of two cylindrical electrodes that are concentrically aligned. The inner and outer electrodes are biased at different voltages allowing electrons with a kinetic energy of the bias difference to pass through the analyzer to the detector. A drawback of the CMA is the limited resolution of the XPS peaks. To improve the resolution, a hemispherical analyzer can be implemented. The hemispherical analyzer consists of an inner and outer hemisphere. A positive voltage is applied to the inner hemisphere and a negative voltage is applied to the outer hemisphere. Only photoelectrons with a kinetic energy between the applied voltages will pass through to the detector. On the path from the detector entrance to the multiplier, the photoelectrons follow a 180° arc which causes electrons of insufficient kinetic energy to be deflected to either the inner or outer hemispheres.

The current generated from photoelectrons is in the range of 10^{-12}-10^{-14} amperes (70). Since this is below conventional current detection limits, a channel electron multiplier is needed to enhance the signal. A channel electron multiplier is a curved glass tube coated with an easily ionized material. When the photoelectrons strike the multiplier, an electron avalanche effect is triggered amplifying the signal by a factor of 10^6-10^8. For this effect to happen, a high voltage is applied to the electron multiplier. The channel electron multiplier voltage applied in the experiments performed for this dissertation was 2.4 kV.

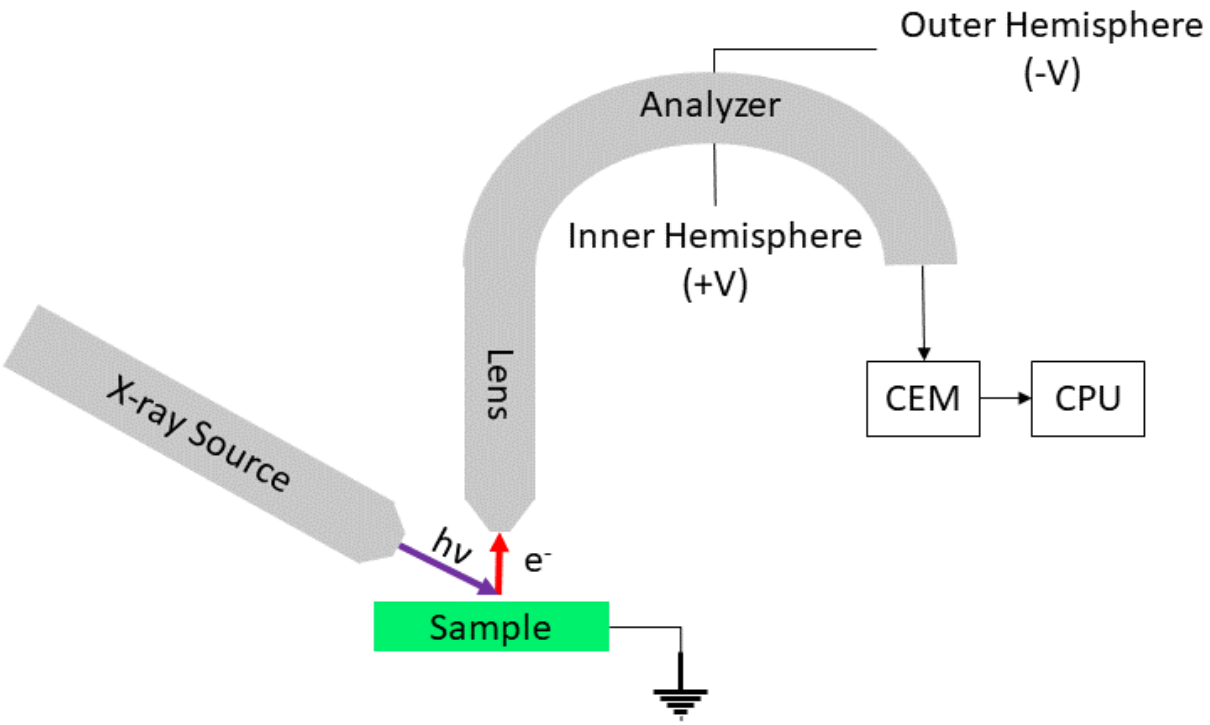

Figure 9 Scheme of an X-ray photoelectron spectrometer with a concentric hemispherical analyzer.

2.4.3. Auger Electron Spectroscopy

2.4.3.1 Theoretical Principles

Like XPS, Auger electron spectroscopy (AES) is used to determine the composition of surfaces. The discovery of AES is credited to Pierre Auger who noticed strange features in X-ray photoelectron spectra (72). These features, now known as Auger peaks, resulted from electrons emitted from the analyte surface whose kinetic energy was not dependent on the incident photon energy. Auger electrons are emitted from an atom when the electrons in the atom relax to fill a core shell hole. This hole is generated by X-ray absorption or collisions with an energetic electron beam. Most AES systems use an electron beam as the incident beam in the process. Figure 10

depicts the Auger process. The incident electron beam collides with core electrons transferring enough energy to eject the core electron from the atom. Outer electrons relax to fill the hole in the core shell and release energy in the process. If the released energy is greater than the binding energy of another outer shell electron, the outer shell electron can absorb the energy and be emitted from the atom. The kinetic energy of Auger electrons is unique to different elements; therefore, AES is used to characterize the chemical makeup of adsorbates or contaminants.

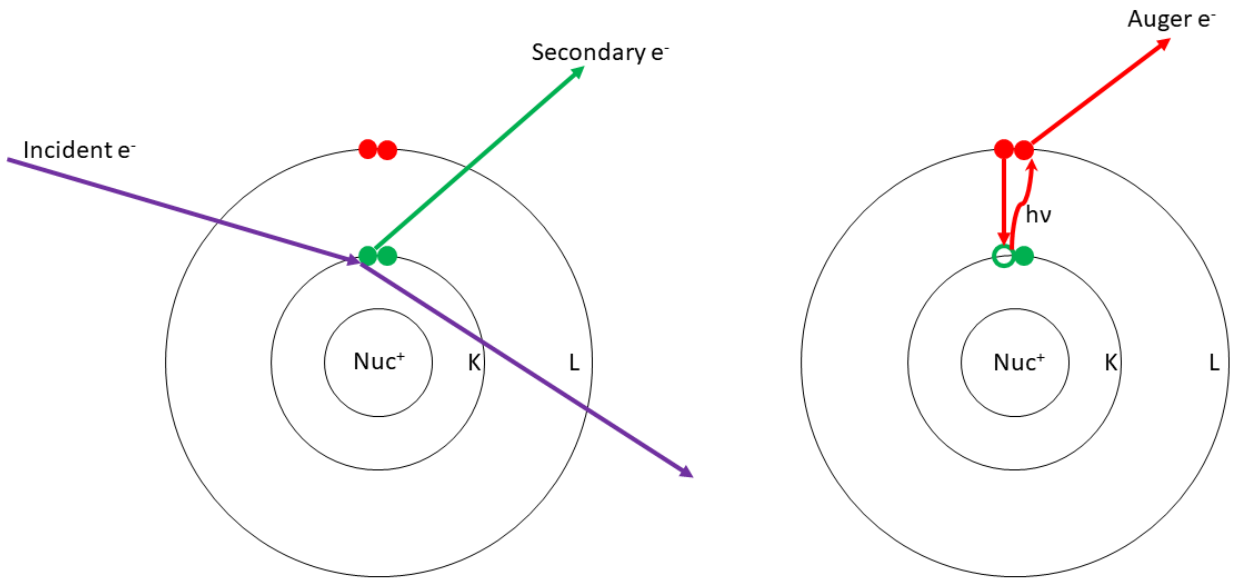

Figure 10 The KLL Auger process. The incident electrons collide with K shell electrons causing the ejection of the K shell electron (secondary electron). An electron from the L shell relaxes to fill the core hole in the K shell. When the L shell electron relaxes, the emitted energy is absorbed by another L shell electron which is ejected from the atom.

As stated above, the kinetic energy of the Auger electron does not depend on the incident beam energy; however, it does depend on the binding energy of the core electron, the binding energy of the relaxing electron, and the binding energy of the Auger electron as expressed in equation 2.5.

$$KE_{Auger} = BE_{secondary} - BE_{relaxing} - BE_{Auger} \qquad \text{Equation 2.6}$$

The Auger transitions are typically denoted with the energy level of the electrons involved. For example, the Auger transition for carbon is written as KLL, where the secondary electron is from the K shell and the relaxing and Auger electrons are from the L shell. Occasionally, V is used to denote the valence shell so the Auger transition in carbon could also be written as KVV.

Different elements have different energies for the same Auger transitions. For example, the KLL transition of carbon occurs at 272 eV but the same transition occurs at 512 eV in oxygen. Furthermore, different elements have different sensitivity factors to the Auger transition. These sensitivity factors are well documented by instrument manufacturers. The composition of analyte surfaces can be calculated, in monolayers, by taking the ratio of an individual peak intensity to the sum of the intensities of all the detected peaks after correcting for sensitivity as in equation 2.6:

$$Conc\ (\%) = \frac{I_x/s_x}{\sum_x (I_x/s_x)} \times 100 \qquad \text{Equation 2.7}$$

Auger electron spectra are recorded as either a measurement of the number of electrons as a function of kinetic energy, N(E)/E, or its differentiated form, dN(E)/dE. The differentiated form is most used due to the rising background of secondary electrons detected as kinetic energy increases. In addition to surveying a range of kinetic energies, line scans, mapping, and profiling can be done with AES. Line scans measure the intensity of specific AES peaks as a function of beam position. This is used to determine where different elements are concentrated or dispersed across a surface. If used in conjunction with electron microscopes, a surface can be imaged with

AES. Like the line scan, Auger mapping is performed by scanning the surface at constant kinetic energies. In mapping, the electron beam is moved across the surface in two dimensions. A contrast image is generated based on the intensity of the signal detected at given x and y coordinates. Depth profiling can also be done with AES by sputtering away a small area of the surface and measuring the intensity of the Auger transition at specific kinetic energies. In a line scan, the beam is passed across the surface, whereas, in depth profiling, the beam is kept in a fixed position. As more material is sputtered away, the composition of surface species could change. This is useful for determining film thickness of deposited materials.

2.4.3.2 Instrumentation

A typical Auger electron spectrometer, illustrated in Figure 11, consists of a few key components: an electron beam source, an analyzer, and an electron multiplier. Electron sources are typically tungsten filaments since they are easy to make and robust. For small beam sizes, lanthanum hexaboride (LaB_6) or field emission guns should be used as electron beam sources. Tungsten filaments can provide consistent electron beams with a diameter no smaller than 3-5 μm; whereas, LaB_6 and field emission guns can produce beams with diameters $\leq$ 20 nm (72). Electron beams are energized with a high voltage so the beam can have sufficient energy to eject core electrons from the sample. Common beam energies for spectral acquisition are 3, 5, and 10 keV. In compact units, the electron source is located inside the analyzer; however, some systems, such as the LK Technologies RVL2000, use the electron source for low energy electron diffraction as a source for AES. X-rays can also be used as incident beams for AES; however, electron beams with the same energy as X-rays are produced more easily and do not require the high voltages described in section 2.4.2 on X-ray photoemission spectroscopy.

After the incident electron beam interacts with the analyte, electrons are emitted from the analyte. These electrons are a mix of secondary and Auger electrons. Cylindrical mirror analyzers and hemispherical analyzers contain electrodes that are individually biased to deflect electrons of undesired kinetic energy. The remaining electrons pass through the analyzer to the electron multiplier where an electron avalanche occurs to amplify the signal by a factor of 10^6-10^8. The signal from the electron multiplier can be plotted to produce a direct measurement spectrum, N(E)/E vs E. As mentioned above, the increasing background of secondary electrons makes the AES peaks difficult to discern. Thus, a lock-in amplifier is used to measure the change in signal from the electron multiplier. The output of the lock-in amplifier is plotted against the analyzer energy to provide a differential Auger electron spectrum, dN(E)/dE vs E.

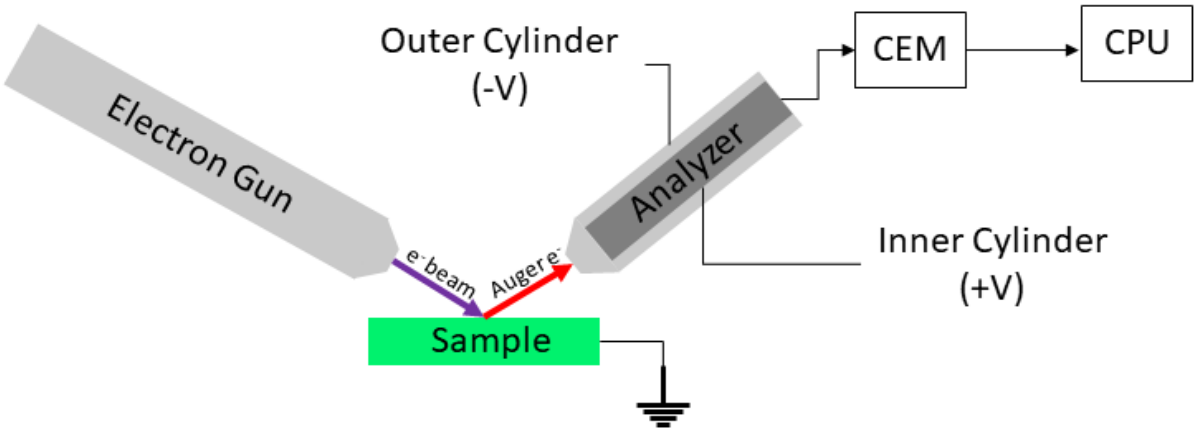

Figure 11 A schematic of an Auger electron spectrometer with an external electron beam source. Models with the electron source built into the analyzer are also widely used.

2.4.4. Low Energy Electron Diffraction

2.4.4.1 Theoretical Principles

Low energy electron diffraction (LEED) is a common surface analysis technique that provides structural information about a surface and adsorbates on that surface. Using a low energy (< 500 eV) electron beam, the surface structure can be probed by electron scattering. The incident electron beam is directed at a surface. Due to the low energy, the electrons are more likely to be scattered by the surface instead of penetrating into the bulk lattice, thus providing a two-dimensional diffraction pattern. When the electron beam is parallel to the surface normal, the elastic backscattering of electrons is maximized. The backscattered electrons arise from the electron beam interacting with the surface atoms along azimuthal indices within the Ewald sphere which demonstrates the relationship between the wavevector of the incident and diffracted electron beams (73). In a two-dimensional system, the Miller indices are represented as (*h*,*k*), and the surface lattice parameters can be determined from the Bragg diffraction equation.

$$a \sin\theta = (h^2 + k^2)^{\frac{1}{2}}\lambda \qquad \text{Equation 2.8}$$

The operation of LEED instruments is simpler than real space imaging techniques such as atomic force microscopy (AFM) and scanning tunneling microscopy (STM). There are five 2-D plane lattice types that can be identified from LEED. The adsorption geometry of adsorbates can be described relative to the substrate lattice by converting the reciprocal lattice parameters to real-space lattice parameters. Adsorbate geometries are often recorded in Wood's notation indicating the relationship between the adsorbate and substrate lattice structure. Wood's notation uses the substrate translation vector multipliers to indicate the size of the adsorbate structure along with an angle if the adsorbate lattice is rotated relative to the substrate lattice. An example of Wood's notation for a possible adsorption structure of CO on Pd(111) is given below:

$$Pd(111)(2x2) - CO$$ Equation 2.9

2.4.4.2 Instrumentation

A typical LEED instrument, shown in Figure 12, consists of an electron source, a fluorescent screen, and a system of grids that allow backscattered electrons of a specific energy to pass to the screen. The electron source is generally a tungsten filament although LaB_6 can also be used. The electrons are produced by heating the filament and then accelerated by applying the desired voltage to the beam. The electron beam then interacts with the sample, and electrons are scattered from the surface. Most of the electrons are inelastically scattered and must be filtered by the grid system to allow only the elastically scattered electrons to reach the screen. In the grid system, there are usually three grids identified as G1, G2, and G3. The grid nearest the sample, G1, is set to ground potential while G2 and G3 are set to an adjustable negative potential to deflect the inelastically scattered electrons. The screen is biased at a positive potential, typically 3-5 kV. This accelerates the elastically scattered electrons to provide enough energy to cause the screen material to fluoresce and produce a pattern of bright spots (73). Samples for LEED analysis must be at ground potential to prevent surface charging because of electron collisions. Surface charging obscures the LEED pattern because the energy of the scattered electrons will be retarded by a positive charge buildup on the surface.

LEED patterns are often recorded simply by photographing the pattern with a digital camera. To enhance the photograph, the camera settings should be set for low light photography. Background light from the room or inside the analysis chamber will mask the LEED pattern, so it is essential that the image is captured in darkness. More sophisticated LEED instruments can provide details about spot intensity. This is done using deflection plates and a channel electron

multiplier to provide spot profile analysis. Our systems are not equipped for spot profile analysis, and our LEED patterns are captured with a standard camera.

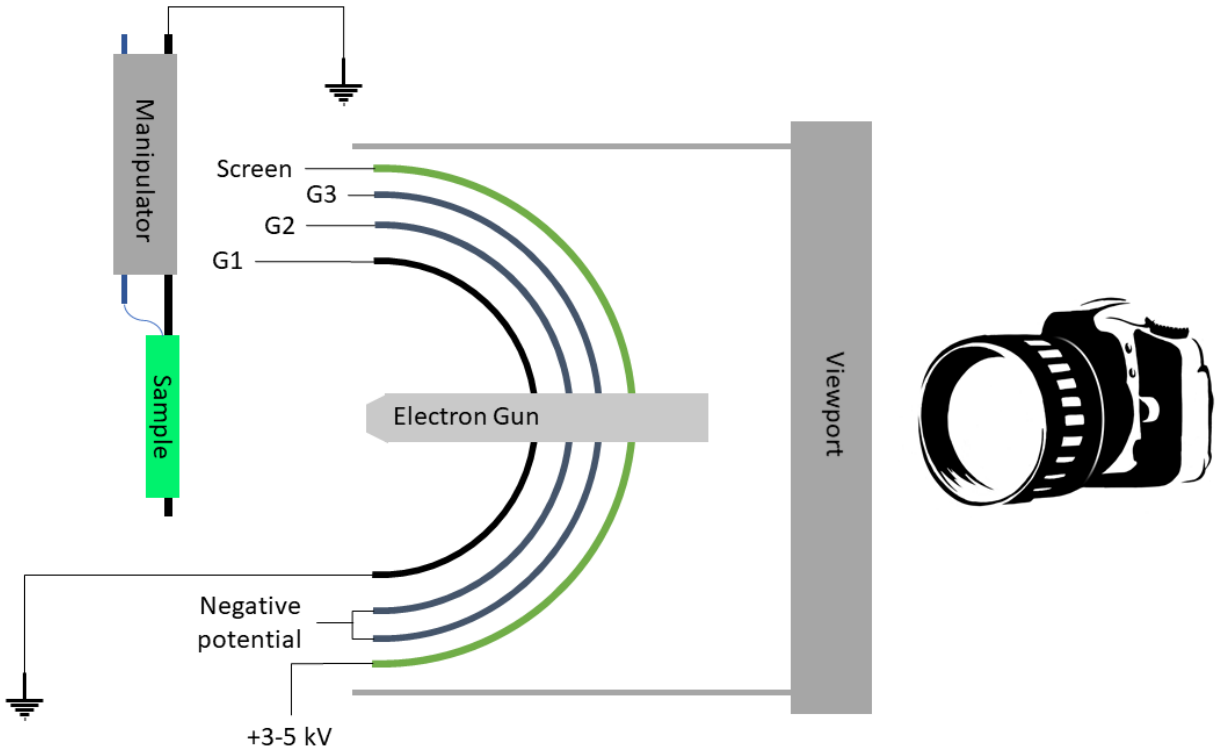

Figure 12 A schematic of a reverse-view LEED instrument.

2.4.5 Temperature Programmed Desorption

2.4.5.1 Theoretical Principles

A common technique in UHV research is temperature programmed desorption (TPD), also referred to as thermal desorption spectroscopy (TDS). Molecular desorption can be described with a kinetic model using time-dependent coverage and a rate constant. Typically, temperature is varied linearly with time at a rate of $\beta = dT/dt$. The kinetic equation can be rearranged to give a dependence on temperature. The desorption rate constant obeys the Arrhenius law, and the

activation energy of desorption can be obtained (74). These relations lead to the Polyani-Wigner model for molecular desorption in equation 2.10 and its linear form equation 2.11, where θ is surface coverage, x is the desorption order, A is the Arrhenius constant, β is the heating rate, E_d is the activation energy for desorption, and T is substrate temperature.

$$-\frac{d\theta}{dT} = \frac{A}{\beta}\theta^x e^{-\frac{E_d}{RT}} \qquad \text{Equation 2.10}$$

$$\ln\left(-\frac{d\theta}{dt}\right) = \ln\left(\frac{A\theta^x}{\beta}\right) - \frac{E_d}{RT} \qquad \text{Equation 2.11}$$

In this model, the desorption rate depends on two parameters: temperature and coverage. As temperature increases, coverage decreases giving rise to peaks in a TPD spectrum. The activation energy for desorption can be obtained by plotting equation 2.11 for different temperatures at which a desired coverage occurs (75). The temperature at which a desired coverage occurs varies with initial coverage.

When gas mixtures are adsorbed onto surfaces, reactions can occur if the activation energy of the reaction or its elementary steps are lower than the activation energy of desorption. Temperature programmed reaction spectroscopy (TPRS) is conducted by simultaneously monitoring the desorption rate of administered gases and possible reaction products. The terms TPD, TDS, and TPRS are used interchangeably although TPD and TDS analysis do not factor in substrate catalyzed reactions. TPRS is far more useful in catalysis studies to provide selectivity towards specific products and determine the minimum temperature at which desired or undesired reactions occur. The competing rates for desorption, dissociation, and reaction convolute TPR spectra. While TPRS provides information about reaction products, it does not provide information about reaction mechanisms.

2.4.5.2 Instrumentation

Typical TPD instrumentation, shown in Figure 13, requires a temperature controller, substrate heating method, and a gas analyzer. A sample is heated at a constant rate and adsorbed molecules are desorbed once there is sufficient energy to overcome the desorption energy barrier. Heating methods are either direct or indirect. Direct substrate heating, also called resistive heating, is performed by passing current through the substrate. The amount of current required to heat the substrate varies by material since different substrates have different resistances. Current is provided by a constant current DC power supply which can be operated manually or by a temperature controller. Indirect heating is realized by electron bombardment of the substrate. A filament is heated by passing current through it, and electrons are emitted from the filament. The electrons are accelerated toward the substrate by applying a positive potential bias to the substrate. The heating rate can be controlled by varying the bias potential. Indirect heating allows for higher temperatures to be obtained and is typically required for substrates that have high annealing temperatures.

Substrate temperature is measured by a thermocouple junction. Type K thermocouples are commonly used since they can accurately measure the temperature in the range of 77 – 1500 K. Heating and cooling the thermocouple junction results in a change in the voltage across the junction. The temperature can be controlled by interfacing a feedback loop to provide current to reach a desired temperature based on the present measurement. This capability is standard in most temperature control devices and allows for a more stable heating rate.

As the substrate temperature is increased, the molecules desorb from the surface and are detected by a quadrupole mass analyzer (QMS). In theory, a user can monitor multiple ions simultaneously; however, this results in slower data acquisition in practice. To maximize

efficiency, our mass spectrometers use up to six measurement channels. For our Pfeiffer Prisma QMS, the provided software allows multiple ion detection (MID). For our UTI 300C QMS, a previous Ph.D. recipient, James Jones, created software in LabView in 2010 (76) which was later modified to increase the number of measurement channels from four to six and monitor temperature by Xu Feng and myself in 2016 as shown in Figure 14.

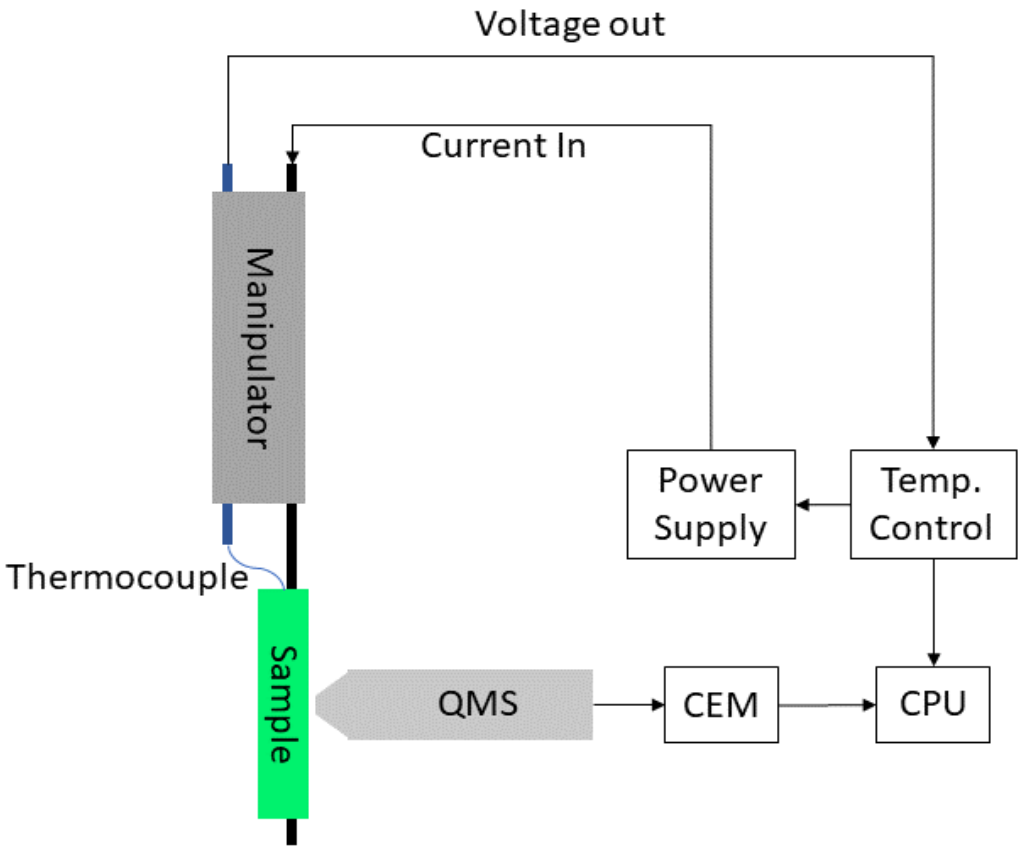

Figure 13 Schematic of a TPD system.

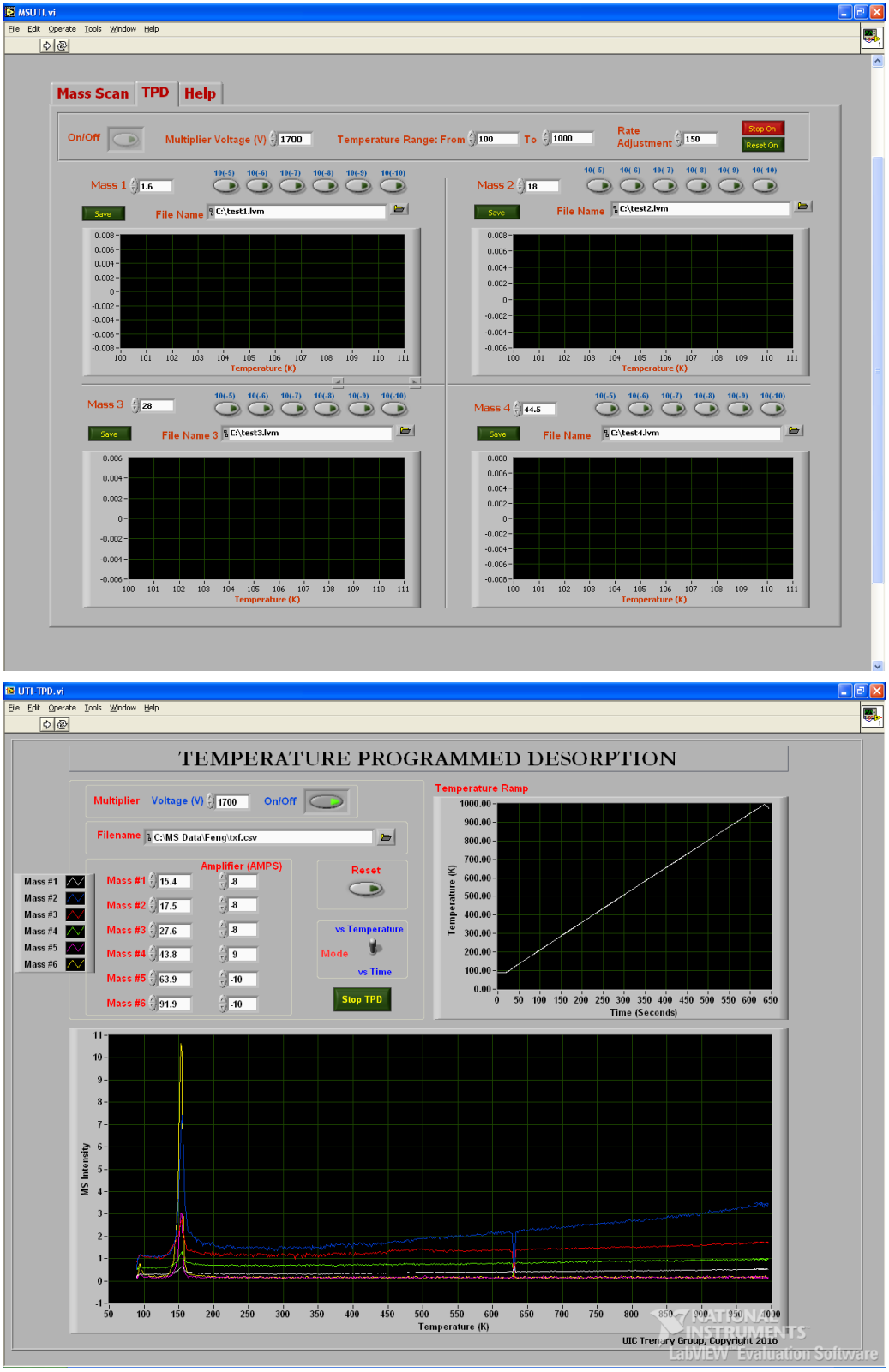

Figure 14 TPD software user interface from 2010 (above) and 2016 (below). The 2016 update allows for simultaneous monitoring of six ions and the heating rate of the Pd(111) crystal.

The QMS signal is plotted against temperature to provide a thermal desorption spectrum. The relative peak area of the spectrum is proportional to the relative surface coverage; therefore, integrating peak area is a common practice to determine the degree of saturation of specific species. In this dissertation, TPD and TPRS are used mainly for qualitative purposes in identifying desorbed reaction products. For quantitative analyses, the peaks must be resolved from overlapping signals of related molecules and fragments.

Chapter 3 – Reaction Pathways for HCN on Transition Metal Surfaces

3.1 Outline

RAIRS and DFT were employed to elucidate the mechanism for HCN adsorption and reaction on Ru(0001) and Pd(111). These results were compared to previous reports on Cu(100), Pt(111), and an HREELS study on Pd(111). Section 3.2 describes the experimental parameters. Section 3.3 explains the DFT methods. Section 3.4 displays the results of the experiments and calculations followed by a discussion in Section 3.5. The chapter is concluded with Section 3.6 followed by a list of references in Section 3.7.

Portions of this chapter are reproduced from Ref. (1) with permission from the PCCP Owner Societies.

3.2 Experimental Methods

The experiments on Pd(111) were conducted in the XPS-System described in Chapter 2. The Ru(001) experiments were conducted in a separate UHV chamber equipped for RAIRS, TPRS, Auger electron spectroscopy and LEED. This apparatus and the crystal mounting and cleaning procedure are described elsewhere (77). Briefly, the Ru(001) crystal was cleaned by Ar^+ sputtering at 5 μA and annealing at 1500 K followed by Ar^+ sputtering at 2.5 μA and annealing at 850 K. Cleanliness was confirmed by O_2 TPD when no carbon oxides were detected with the mass spectrometer.

Hydrogen cyanide was synthesized using the method of Hagans et al. in which potassium cyanide was reacted with H_2SO_4(aq) (78). Natural abundance KCN was purchased from Aldrich Chemical Company with a quoted purity of 97%. $H^{13}C^{14}N$ and $H^{12}C^{15}N$ were synthesized using the same procedure with $K^{13}C^{14}N$ and $K^{12}C^{15}N$, which were purchased from Cambridge Isotope Laboratories with quoted purities of 99 and >98 %, respectively. The purity of the HCN gases were verified with mass spectrometry and no impurities were detected.

3.3 Computational Methods

Self-consistent, periodic DFT calculations were performed using the Vienna Ab Initio Simulations Package (VASP v5.2 and above(79)) in the optB86b Van der Waals (vdW) functional developed by Klimeš et al. (80,81) as well as the GGA-RPBE functional (82) for comparison. Core electrons were described by the projector augmented wave (PAW) method (83,84) and the Kohn-Sham valence states (including Pd(4d5s); Ru(4d5s); N(2s2p); C(2s2p); and H(1s)) were expanded in a plane wave basis set up to a cutoff energy of 500 eV. The electronic states were smeared using a first-order Methfessel-Paxton

scheme with a temperature of 0.075 eV (85). All total energies were extrapolated back to 0 K.

The lattice constants were calculated to be 3.906 Å for Pd and 2.704/4.259 Å for Ru using the optB86b vdW functional, in close agreement with measured values (3.92 Å and 2.70/4.266 Å, respectively (86)). In comparison, the RPBE lattice constant for Pd is 3.941 Å. The fcc(111) facet was modeled using a four-layer slab with either a (2×2) or a (4×2) surface unit cell, and the Brillouin zone was sampled on a 7×7×1 and 5×7×1 Monkhorst-Pack *k*-point mesh, respectively. A vacuum space of ~16 Å was included in the *z* direction to minimize interactions of neighboring images, together with electrostatic decoupling in the *z* direction (87). The top two layers of metal atoms were fully relaxed, with the bottom two fixed at bulk positions. Geometric optimization (i.e. structural relaxation) was converged to 0.01 eV/Å for each relaxed degree of freedom.

Adsorption energies were calculated as $\Delta E = E_{slab} + E_{mol} - E_{total}$, where E_{slab}, E_{mol}, and E_{total} are the energies of the clean surface without any adsorbate, the adsorbate molecule isolated in the gas phase in a neutral state (closed-shell or radical), and the surface with the adsorbate. A more positive ΔE therefore corresponds to stronger adsorption. The minimum-energy reaction path for an elementary step and the transition state (TS) associated with it were determined using the climbing-image nudged elastic band (CI-NEB) method (88) and the dimer method (89). The activation energy was calculated as $E_a = E_{TS} - E_{IS}$, where IS and TS denote the initial state and transition state, respectively. Each TS was verified to possess only one vibrational mode with imaginary frequency in the direction of the bond being broken or formed. Transition state search was converged to 0.03 eV/Å for each relaxed degree of freedom. The simulated IR spectra of surface adsorbates were

calculated using the Atomic Simulation Environment (90). The vibrational modes and frequencies were calculated from a finite difference approximation of the dynamical matrix, and the IR intensities were calculated from a finite difference approximation of the gradient of the dipole moment in the z direction (90). The magnitude of the displacement was 0.01 Å in each relaxed degree of freedom. The zero-point energies (ZPE) were calculated from the vibrational frequencies (ν_i) of a molecule as.

$$E^{ZPE} = \frac{1}{2}\sum_i h\nu_i \qquad \text{Equation 3.1}$$

3.4 Results

3.4.1 RAIR Spectra

The changes in the RAIR spectra for increasing exposure of HCN to Ru(001) at 90 K are shown in Figure 15. Similar behavior was observed on Pd(111) and Pt(111) (9). For the highest exposures, HCN forms a multilayer and the spectra are similar to those reported previously for solid HCN (91–94). As a linear triatomic molecule, HCN has three fundamentals: the CH and CN stretches and the bending mode. At the lowest exposure, only the CH stretch at 3297 cm^{-1} is observed. As the exposure increases, it changes from a single-sharp peak in the 0.1 L spectrum, to a broader pair of peaks 3246 and 3134 cm^{-1} after a 5 L exposure. At the saturation coverage of HCN, the CN stretch is weakly present at 2180 cm^{-1} (Fig.51 Appendix A) . In the solid, HCN forms linear chains of hydrogen-bonded molecules and the strong red-shift and broadening of the CH stretch is consistent with the formation of hydrogen bonds in the multilayer. For the multilayer, the bending fundamental at 845 cm^{-1} is by far the most intense. The CN stretch, seen at 2101 cm^{-1} in the 5.0 L spectrum, is notably weak relative to the other fundamentals for gas and solid phase HCN and for HCN in an Ar matrix and is thus an intrinsic characteristic of the molecule. The CH stretch at 3297 cm^{-1} is close to the value of gas phase HCN (12) at 3312 cm^{-1} and of HCN in an Ar

matrix (14,15) at 3305-3306 cm^{-1}. As this value is indicative of the hybridization of the carbon atom, it follows that the adsorbed HCN retains a CN triple bond. The spectra at the lowest coverages are thus most consistent with an HCN molecule bonded through the nitrogen lone pair with the axis

perpendicular to the surface. With this orientation, the bending mode would not be surface IR allowed. However, the overtone of the bend would be allowed, and peaks assigned to it were observed at 1311-1323 cm^{-1} on Pt(111) (6,9) and at 1395 on Cu(100) (9). No peak clearly attributable to the bending overtone is observed for low coverages on Ru(001), although there are broad but weak features in this spectral region.

Upon annealing the HCN covered Ru(001) surface to 150 K and above, all peaks disappear from the RAIR spectrum. We interpret this as indicating complete dissociation to atomic species. A distinctly different change is seen in the RAIR spectra of HCN on Pd(111), as shown in Figure 16. After exposing the Pd(111) surface at 90 K to 1.0 L of $H^{12}C^{14}N$, two peaks are seen at 1641 and 3301 cm^{-1}. These are assigned to molecularly adsorbed HCN. As for HCN on Ru(001), the value of the CH stretch is indicative of an sp-hybridized carbon atom thus implying a triple CN bond.

The assignment of the peak at 1641 cm^{-1} is less straightforward. In solid HCN (91–93), the overtone of the bending mode occurs at 1621-1632 cm^{-1} whereas it is at 1427 cm^{-1} in an Ar matrix (15) and at 1412 cm^{-1} in gas phase HCN (95). For HCN on Pt(111) and Cu(100), we assigned peaks at 1311 and 1395 cm^{-1} to the bending overtone (6,9). The peak observed at 1641 cm^{-1} in Fig. 16 could be plausibly assigned to the bending overtone, but this frequency is also consistent with a CN double bond stretch mode. One way to distinguish between these two possibilities is through isotopic shifts. Table I compares the values of the HCN bending modes

and CN stretch modes of gas phase HCN and of CNH_2 on Pt(111) upon substitution with ^{13}C and ^{15}N along with the ratio of the frequencies for the ^{13}C and ^{15}N isotopologues.

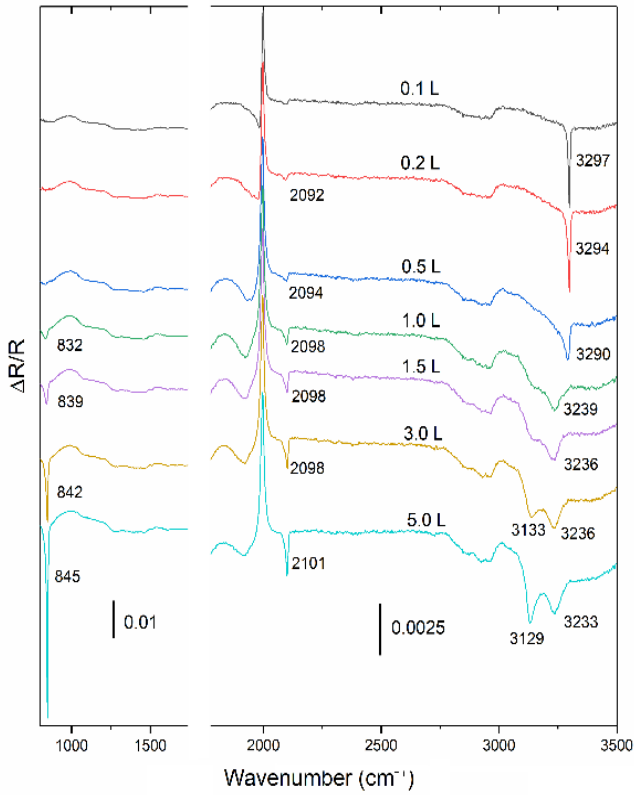

Figure 15 RAIR spectra for increasing exposures of HCN to Ru(001) at 90 K. The negative peak just below 2000 cm^{-1} is due to adsorbed CO that is displaced and shifted upon HCN adsorption.

As the values of the bending overtone for the ^{13}C and ^{15}N isotopologues of HCN in an Ar matrix are not available in the literature, the frequencies given in Table I are simply twice the fundamentals given by Nakagawa and Morino (13). With ratios of 0.9872 and 0.9884 upon ^{13}C

and ^{15}N substitution, the peak on Pd(111) shows shifts similar to those seen on Pt(111) for the peak assigned to the bending mode overtone, despite the rather different frequencies (1641 vs 1311 cm^{-1}). Moreover, these shifts are notably different from what is seen for the CN bond stretch of gas phase HCN or of CNH_2 on Pt(111), where the bond-order is between one and two. We therefore assign the 1641 cm^{-1} peak for HCN adsorbed at low temperature on Pd(111) to the overtone of the bending mode. This mode would be surface IR allowed for an upright HCN orientation, although the bending fundamental would not be allowed. While a wavenumber value of 1641 cm^{-1} is consistent with a C=N stretch, a C=N double bond implying sp^2 hybridization on the carbon atom is not consistent with the high value of the CH stretch peak at 3301 cm^{-1}.

Table I*:* Wavenumber (cm^{-1}) positions of infrared peaks of HCN isotopologues and ratios (in parentheses) of positions relative to $H^{12}C^{14}N$.

	$H^{12}C^{14}N$	$H^{13}C^{14}N$	$H^{12}C^{15}N$
δ(HCN), Ar matrix (14)	721	715 (0.9917)	720 (0.9986)
2× δ(HCN), Ar matrix (14)	1442	1430 (0.9917)	1440 (0.9986)
ν(CN), gas (13)	2097	2063 (0.9838)	2064 (0.9838)
2× δ(HCN), Pt(111) (6)	1311	1295 (0.9878)	1303 (0.9939)
2× δ(HCN), Pd(111)	1641	1620 (0.9872)	1622 ((0.9884)
ν(CN), CNH_2 Pt(111) (6)	1323	1290 (0.9751)	1312 (0.9917)

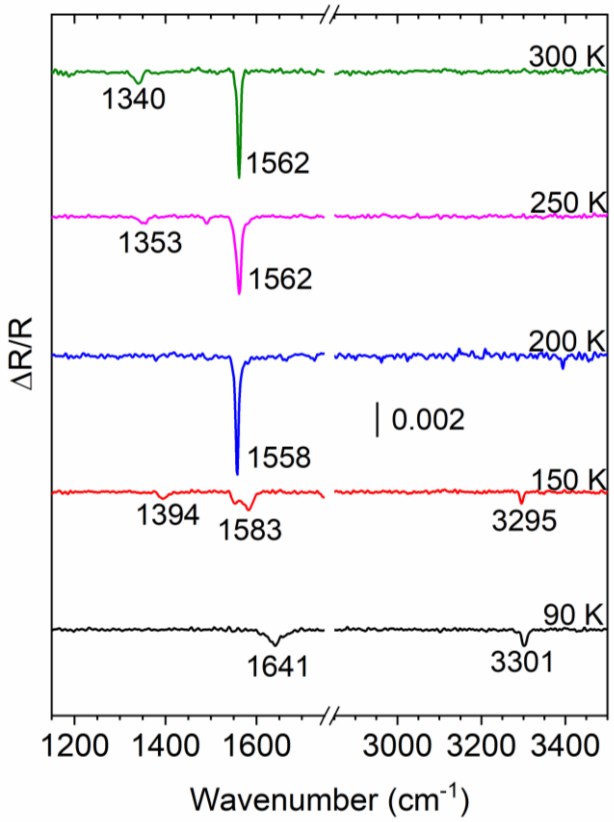

Figure 16 RAIR spectra of $H^{12}C^{14}N$ after exposure of 1.0 L to Pd(111) and annealing to the indicated temperatures. These spectra were obtained with 4096 scans, corresponding to approximately 16 minutes per spectrum.

The RAIR spectra in Fig. 16 shows that as the HCN covered Pd(111) surface is heated, the peaks associated with adsorbed HCN are replaced by a new set of peaks, the most prominent of which is at 1562 cm^{-1} in the 250 and 300 K spectra. In the 150 K spectrum the reaction is incomplete with some adsorbed HCN still present as indicated by the CH stretch at 3295 cm^{-1}. The spectra in Fig. 16 were obtained with 4096 scans, requiring approximately 16 minutes per spectrum. While this reduces the noise level, it also can lead to some miscancellations between the background and sample spectra leading to artefacts. The peaks that are labelled in Fig. 16 are

reproducible, while other features, such as the peaks at about 3400 cm^{-1} in the 200 K spectrum and 1500 cm^{-1} in the 250 K spectrum, are not.

Table II. Peak positions for the ν(CN) and δ(NH_2) modes of CNH_2 on Pd(111) (experimental and calculated) and Pt(111) (experimental) and ratios, in parentheses, of the positions relative to those of $^{12}C^{14}NH_2$.

Mode, Isotopologue	Pd(111) (exp.)	Pd(111) (calc.)	Pt(111) (exp.)
ν(CN), $^{12}C^{14}NH_2$	1354	1347	1323
ν(CN), $^{13}C^{14}NH_2$	1328 (0.9808)	1317 (0.9777)	1290 (0.9751)
ν(CN), $^{12}C^{15}NH_2$	1342 (0.9911)	1337 (.09926)	1312 (0.9917)
δ(NH_2), $^{2}C^{14}NH_2$	1564	1524	1567
δ(NH_2), $^{3}C^{14}NH_2$	1562 (0.9987)	1521 (0.9980)	1566 (0.9994)
δ(NH_2), $^{2}C^{15}NH_2$	1554 (0.9936)	1514 (0.9934)	1559 (0.9949)

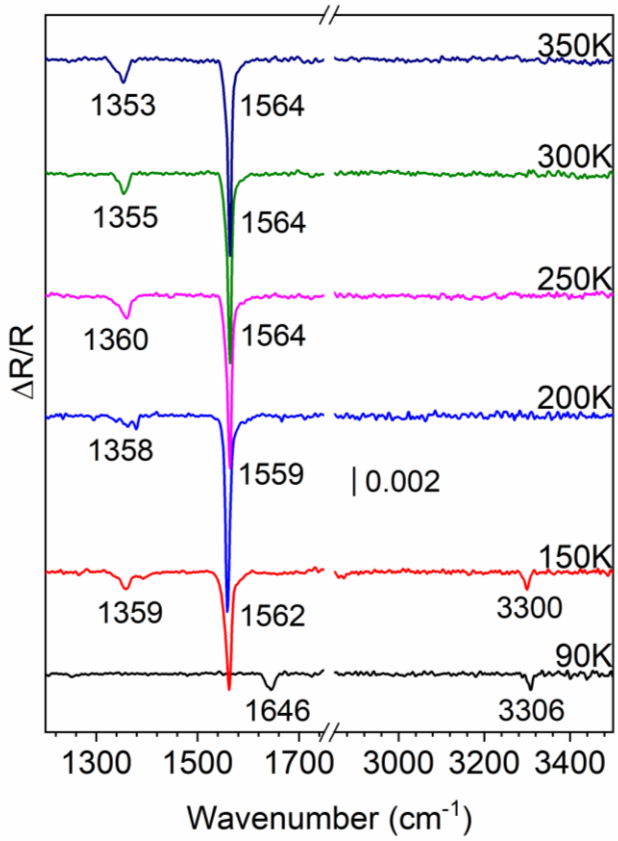

Figure 17 RAIR spectra of 1.0 L $H^{12}C^{14}N$ taken at 90 K after annealing for one minute at the indicated temperatures.

The most significant changes occur in the lower wavenumber range and Fig. 17 shows spectra from 1150 to 1750 cm^{-1}, which were obtained with 1024 scans, which eliminates some of the artefacts seen with 4096 scans in Fig. 16. As before, the 150 K anneal causes the 1646 cm^{-1} peak to disappear and be replaced by peaks at 1562 and 1359 cm^{-1}. The 1359 cm^{-1} peak is accompanied by a weak feature at about 1390 in the 150 K spectrum, and this region shows some possible structure in the 200 K spectrum, which may be indicative of incomplete conversion of HCN to CNH_2. The spectra show little change from 200 to 350 K, demonstrating the stability of

CNH_2 on the Pd(111) surface. The assignment of the CNH_2 peaks seen in Fig. 17 is aided by repeating the experiment with $H^{13}C^{14}N$ and $H^{12}C^{15}N$ and spectra with these isotopologues analogous to those of Fig. 17 are given in Appendix A (see Appendix A, Figure 51). Fig. 18 shows a comparison of the spectra obtained starting with $H^{12}C^{14}N$, $H^{13}C^{14}N$ and $H^{12}C^{15}N$. Table II lists the wavenumber values for the ν(CN) and δ(NH_2) modes for CNH_2 on Pd(111) along with the corresponding values for CNH_2 on Pt(111). The fact that the peak at 1564 cm^{-1} shifts to 1554 upon ^{15}N substitution but to only 1562 with ^{13}C substitution clearly reveals that this is a δ(NH_2) mode, rather than a C=N stretch. The large shift of the peak at 1354 to 1342 cm^{-1} with ^{15}N substitution and to 1328 cm^{-1} with ^{13}C substitution clearly indicates that it is a CN stretch mode. The similar positions and isotopic shifts of the peaks on Pd(111) and Pt(111) indicates that the same species, aminocarbyne, forms on both surfaces.

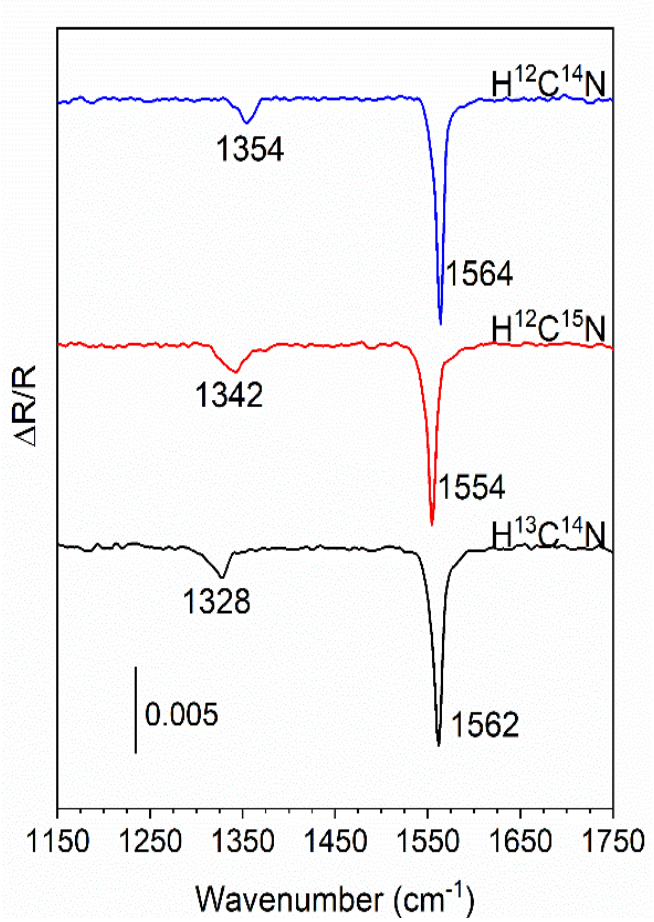

Figure 18 A comparison of RAIR spectra taken at 90 K for each isotope after annealing at 300 K for one minute.

3.4.2 Computational Results

3.4.2.1Adsorption of surface intermediates

To help elucidate the identities of the surface intermediates in the decomposition of HCN on Pd(111) and to establish the reaction mechanism for it, we first modelled and calculated potential intermediates based on prior work on this and other similar systems by us and other groups. Table III lists various intermediates' adsorption energies (ΔE_{ads}) calculated using the RPBE and optB86b functionals. Figure 19 shows the optimized molecular structures of these

species. The images of the molecules in this figure and those below were created using VESTA (96). The preferred adsorption sites of several of the species, including di-σ HCN, CN, and atomic H, are consistent with those previously reported by Herron et al. (97) CN, CNH, and CNH_2 all preferentially adsorb in upright geometries on the fcc threefold site. We have not found any stable geometry for CN adsorbed on Pd(111) in which the C-N bond is parallel to the surface, in agreement with Herron et al. and contradicting Kordesh et al (4).

Bader analysis indicates that the C atom in CN carries a charge of +0.56 *e* whereas the N atom carries -0.93 *e*, making the CN group overall negatively charged (98). *Cis*- and *trans*-HCNH are included in consideration as potential intermediates to CNH_2. The *cis* isomer binds through both C and N in the bridge-top geometry, whereas the *trans* isomer binds through C on the top site only. Atomic N and H prefer to adsorb on the fcc site, whereas atomic C prefers to adsorb on the hcp threefold site. The RPBE adsorption energies of CN, N, and C are noticeably more negative than those reported by Herron et al., which were calculated self-consistently in PW91 and non-self-consistently in RPBE. The latter may have been incomplete for describing the strong chemical bonding between the C or N and Pd.

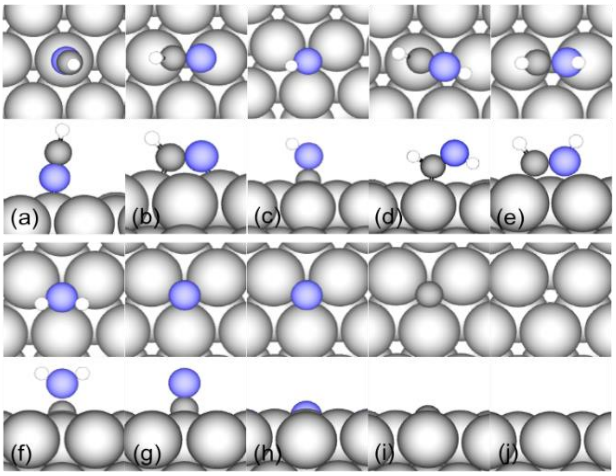

Figure 19 DFT (optB86b-vdW) calculated minimum-energy adsorption configurations for (a) upright HCN; (b) di-σ HCN; (c) CNH; (d) trans-HCNH; (e) cis-HCNH; (f) CNH2; (g) CN; (h) N; (i) C; (j) H. In each panel the top view is shown on top and the side view is shown on bottom. Silver, blue, black, and white spheres represent Pd, N, C, and H atoms, respectively. Molecular images in this figure and those below are created using VESTA. Periodic images of the adsorbates have been removed for clarity.

The fact that the molecular adsorption of upright HCN is not exothermic according to RPBE appears to be inconsistent with its facile reactivity on this surface. A recent study by Hensley et al. (99) finds that the contribution of vdW energies to adsorption on transition metal surfaces becomes significant when the values of RPBE ΔE_{ads} fall roughly below 70% of the corresponding ones for optB86b (99). Based on the adaptive sum method introduced by Hensley et al., we conclude that the optB86b values more closely reflect the actual heats of adsorption for most of the intermediates on Pd(111), although overbinding to some extend by optB86b is expected.

Table III DFT-calculated minimum-energy configurations and associated adsorption energies (ΔE_{ads}, in eV) of various molecular and atomic intermediates in HCN decomposition on Pd(111), in comparison with available DFT and experimental literature values.

Species	Preferred site	ΔE_{ads}		DFT lit. [1]	Exp. lit.
		GGA-RPBE	optB86b-vdW		
HCN upright	top	0.00	-0.56		-0.39 [2]
HCN di-σ	top-top | br-br	-0.47	-1.29	-0.42	
$(HCN)_2^{\alpha}$	top-top-br	-0.15 [3]	-1.02 [3]		
HCNH trans	top	-1.75	-2.49		
HCNH cis	br-top	-2.21	-3.21		
CNH	fcc	-1.69	-2.40		
CNH_2	fcc	-3.57	-4.48		
CN	fcc	-3.33	-4.08	-3.25	
$(CN)_2$	top-top	-3.11 [3]	-3.78 [3]		
C	hcp	-6.40	-6.99	-5.80	
N	fcc	-4.29	-5.03	-3.55	
H	fcc	-2.69	-3.06	-2.69	-2.80 [4]

Each adsorbate is located on a (2×2) surface unit cell at 1/4 ML coverage. ΔE_{ads} is with respect to each adsorbate in gas phase and is non-ZPE corrected. "br" stands for bridge site.
[1] From Ref. (97)
[2] From Ref. (100)
[3] per unit of HCN or CN.
[4] From Ref. (101)

The low-temperature desorption features observed by Guo et al. (100), from which they deduced a maximum desorption barrier of 9.1 kcal mol^{-1} (the α_3 state), most likely correspond to desorption from the upright HCN state present in a saturated HCN adlayer because the value is consistent with the optB86b ΔE_{ads} of -0.56 eV (-13 kcal mol^{-1}) for upright HCN. The subsequent investigation of the decomposition pathway is conducted based on the optB86b results.

3.4.2.2 Simulated infrared spectra of intermediates

The IR spectra for the possible H_xCN intermediates have been simulated and compiled in Fig. 20, which include only the fundamental modes but not overtones. The most prominent features include the $\delta(NH_2)$ mode of CNH_2 (1538 cm^{-1}) and ν(CH) mode of upright HCN (3366

cm^{-1}). They are in line with the assignment of 1564 cm^{-1} to CNH_2 and 3301 cm^{-1} to HCN. CNH, and cis- and trans-HCNH have several modes with moderate IR intensity. CN by itself has essentially no IR-active mode, although its ν(CN) mode is calculated to have a frequency of 1922 cm^{-1}, in agreement with the HREELS assignment of 1910 cm^{-1} by Kordesh et al. to CN (4).

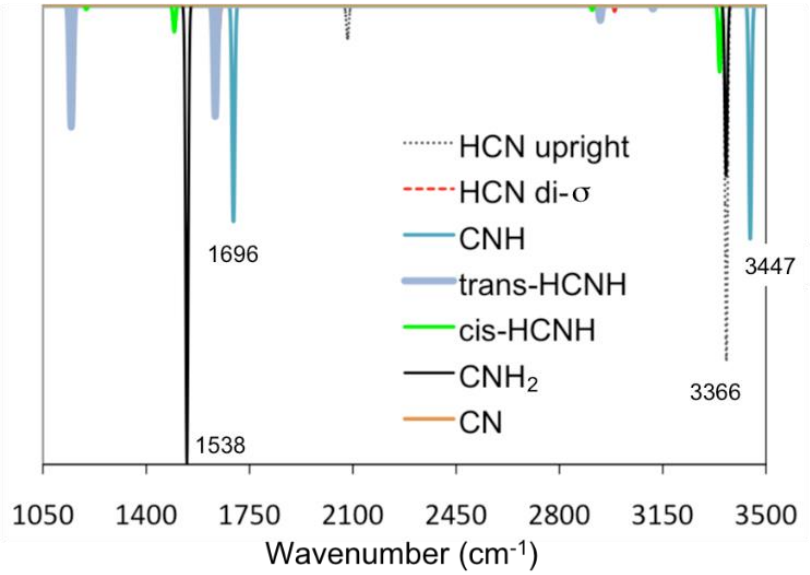

Figure 20 DFT (optB86b-vdW) calculated IR spectra of possible molecular intermediates formed upon adsorption of HCN on Pd(111). All intermediates calculated at 1/4 ML coverage without any co-adsorbate.

We have also simulated IR spectra for isotopically labeled CNH_2 coadsorbed with CN (Fig. 21), for reasons that will become clear below. The two modes shown in Fig. 21 are δ(NH_2) and ν(CN) of CNH_2. As can be seen, the experimental isotopic shifts seen in Fig. 18 are closely

reproduced by the computational results in Fig. 13, which further confirms the assignment of the 1564 and 1354 cm^{-1} peaks (Fig. 18).

3.4.2.3 Reaction pathway for HCN decomposition on Pd(111)

We have explored a number of possible reaction pathways to explain the reactivity of HCN following its deposition on Pd(111), including the nature of the hydrogenation/dehydrogenation steps that are operative at cryogenic temperatures. Two minimum-energy reaction pathways are reported below, one uni-molecular (Fig. 22) and the other bi-molecular (Fig. 23). The minimum-energy unimolecular mechanism for the formation of CNH_2 consists of the steps listed in Table IV corresponding to what is depicted in Fig 22.

The upright HCN state, which vibrational analysis indicates to be unstable according to RPBE but which does represent a shallow minimum on the potential energy surface according to optB86b, is predicted to convert to the di-σ state with an essentially zero barrier as an isolated molecule (Fig. 22 and Table IV). This suggests that the upright state cannot exist on the surface except under locally high coverage conditions where its isomerization is sterically hindered.

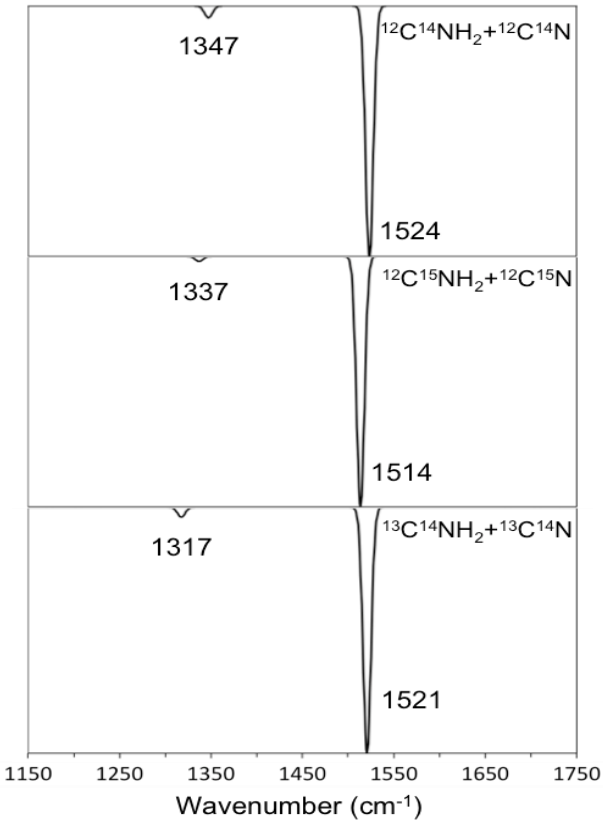

Figure 21 DFT (optB86b-vdW) calculated IR spectra of normal and isotopically labelled CNH_2 on Pd(111). CNH_2 is coadsorbed with CN on a (4×2) surface unit cell, for an overall coverage of 1/4 ML.

The minimum energy uni-molecular mechanism does not proceed through HCNH as an intermediate, unlike what was previously proposed by Gómez-Díaz and López for CNH_2 formation on Pt(111) (18). Similar to the energetics that they reported, the uni-molecular hydrogenation/dehydrogenation steps have significant kinetic barriers. Even with ZPE corrections included, the size of the activation energies for the last 3 steps is clearly inconsistent with the observed formation of CNH_2 at a temperature as low as 150 K, wich implies a maximum barrier of ca. 0.4 eV.

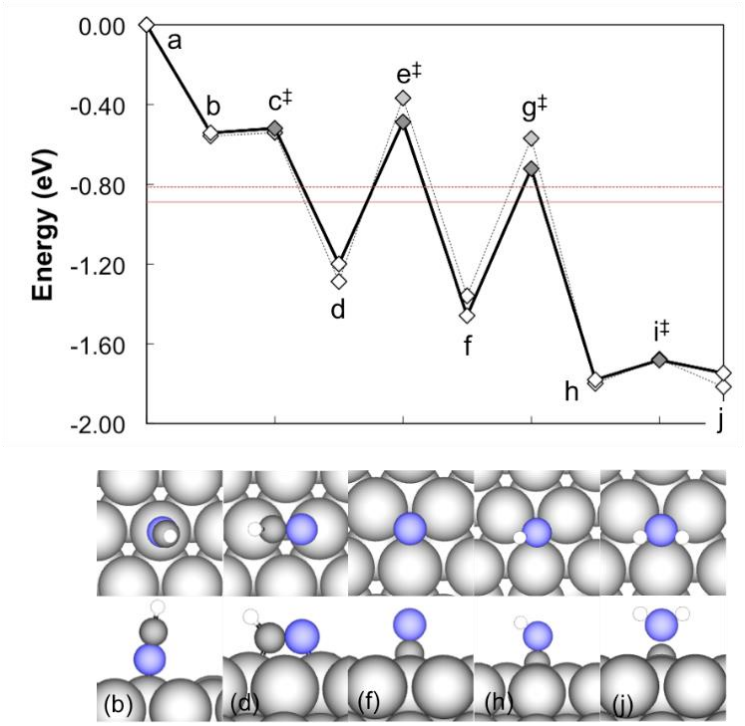

Figure 22 (Upper) DFT (optzB86b-vdw) calculated reaction energy diagram for HCN decomposition on Pd(111) at 1/4 ML coverage. Zero on the y-axis corresponds to a gas phase HCN molecule and an H atom adsorbed on surface. Horizontal lines correspond to atomic H, C, and N (i.e. atomized HCN). Dash and solid lines correspond to ZPE-corrected and non-ZPE-corrected total energies. (Lower) Snapshots of the surface intermediates and transition states, with top views on top and side views on bottom. Labels correspond to those in the upper panel. Silver, blue, black, and white spheres represent Pd, N, C, and H atoms, respectively. surface intermediates and transition states, with top views on top and side views on bottom. Labels correspond to those in the upper panel. Silver, blue, black, and white spheres represent Pd, N, C, and H atoms, respectively.

We use the semi-classically corrected harmonic transition state theory (SC-HTST) formulated by Fermann et al. (102) to estimate the contribution of quantum tunneling to the reactivity of the last hydrogenation step, which has the highest barrier of the 4 steps. The eigenvalue of the imaginary mode is found to be 1032 cm^{-1}, which corresponds to a crossover temperature of 239 K. On the other hand, 1.20 eV corresponds to a peak reaction temperature of 462 K based on Redhead analysis for a second-order rate process with initial coverage of 1 ML

and a heating rate of 2 K s^{-1}. Therefore, we conclude that quantum tunneling does not play any significant role in promoting the uni-molecular mechanism for CNH_2 formation.

Table IV OptB86b-vdW calculated forward activation energies (E_a, in eV), reaction energies (ΔE, in eV)[#] in the minimum energy uni-molecular mechanism

Step	E_a	ΔE	E_a^{ZPE}	ΔE^{ZPE}
1. $HCN^{upright} \rightarrow HCN^{di\text{-}\sigma}$	0.01	-0.73	0.00	-0.71
2. $HCN \rightarrow CN + H$	0.93	-0.07	0.74	-0.21
3. $CN + H \rightarrow CNH$	0.79	-0.44	0.74	-0.32
4. $CNH + H \rightarrow CNH_2$	1.23	+0.03	1.20	+0.21

[#] ΔE calculated with species at infinite separation.

Alternatively, we have explored whether bi-molecular interaction can facilitate the formation of CNH_2, and found it to be possible. The bi-molecular mechanism (Fig. 23), which to our knowledge has not been proposed before for HCN on transition metals, consists of the steps listed in Table V. All steps except one involve two (or two units of) HCN or its derivates reacting with each other. The pathway begins with an upright HCN coupling via its C atom to the N atom of a di-σ HCN, yielding a dimer state ($(HCN)_2^{\alpha}$). This species is reminiscient of the known HCN trimer, s-triazine, and its formation is consistent with the tendency of HCN to polymerize due to its possession of both a nucleophilic N and and electrophilic C. This step has a small barrier of 0.17 eV, below the negative of the ΔE_{ads} of the upright HCN state. After structural rearrangement, the dimer state $(HCN)_2^{\beta}$ undergoes dehydrogenation with a low activation energy of 0.14 eV. The remaining fragment, CNCHN, then undergoes an intramolecluar CN bond scission to produce a

CN group and an upright HCN. An intermolecular H transfer between the two species yields a CNH and an NC group binding through the N atom to a top site. The NC species is significantly less stable than the CN group, and it undergoes rapid conversion to the latter through a flipping movement. Finally, two CNH molecules undergo another intermolecular H transfer to produce CNH_2 and CN. The highest kinetic energy barrier is 0.51 eV (Step 5), which is much more in line with the observed low-temperature reactivity of HCN. Due to the involvement of upright HCN, a locally high coverage would be required to stabilize the state, which implies that this mechanism would not be operative at very low initial HCN coverages. We have used the approach by Herron et al.(97) to estimate the diffusion barriers for upright and di-σ HCN. Both are estimated to be less than 0.1 eV, indicating that surface mobility does not preclude adsorbed HCN molecules from finding and reacting with one another on Pd(111).

Table V OptB86b-vdW calculated forward activation energies (E_a, in eV), reaction energies (ΔE, in eV per unit of HCN)[#] in the minimum energy bi-molecular mechanism.

Step	E_a	ΔE	E_a^{ZPE}	ΔE^{ZPE}
1. 2HCN → $(HCN)_2^{\alpha}$	0.17	-0.23	0.17	-0.18
2. $(HCN)_2^{\alpha}$ → $(HCN)_2^{\beta}$	0.53	+0.10	0.46	+0.09
3. $(HCN)_2^{\beta}$ → CNCHN+H	0.25	-0.38	0.14	-0.43
4. CNCHN → CN+HCN	0.56	+0.10	0.48	+0.06
5. CN+HCN → CNH+NC	0.61	+0.25	0.51	+0.24
6. CNH+NC → CNH+CN	0.35	-0.43	0.34	-0.42
7. 2CNH → CNH_2 + CN[†]	0.20	-0.04	0.11	-0.02

[#] ΔE calculated with organic species co-adsorbed in same (2×2) surface unit cell. Balance of H is placed at infinite separation.
[†] ΔE calculated with balance of CN and H at infinite separation.

The pathway produces coadsorbed CNH_2 and CN, which stabilize each other by 0.22 eV, with ZPE and are slightly more stable than a pair of coadsorbed CNH by $2 \times \Delta E = -0.04$ eV. On an isolated basis, as indicated by the dashed lines in Fig. 23, CNH is more stable than CNH_2 by 0.11 eV, or 0.18 eV with RPBE. Thus, although DFT predicts CNH_2 to be a stable product, it is not predicted to be overwhelmingly more stable than CNH.

This is potentially a significant discrepancy with experiment, which finds no vibrational signature attributable to CNH on Pd(111). Whether this is due to any intrinsic error of DFT requires further investigation. In any case, this mechanism predicts that following the formation of CNH_2, the surface has a significant amount of CN and atomic H coexisting with CNH_2 since for every CNH_2, 3 CN molecules and 2 H atoms are formed. The presence of excess H atoms on the surface is consistent with the TPD findings of Guo et al. (100), who reported a H_2 desorption peak ca. 300 K that resembles the 2nd order desorption of pure hydrogen from Pd(111). We have also calculated the energy of adsorbed atomic H, C, and N (representing the complete atomization of HCN), which are less stable than di-σ HCN, CN, CNH, and CNH_2 (Fig. 22), indicating that thermodynamics does not favor complete dissociation of HCN on Pd(111), which is indeed not observed experimentally.

To shed light on the fate of HCN on Ru(001) and Cu(100), we compare the energies of several possible states, including upright and di-σ HCN, CN + H, CNH_2, and all atoms on Pd(111), Ru(001), and Cu(100) in Table VI. The energies for the species on Pd(111) are those plotted in Fig. 22. On Ru(001) the completely atomized state has by far the lowest energy, at 2.80 eV, which suggests a significant driving force toward atomization on Ru(001) and is consistent with the fact that only upright HCN is observed on Ru(001). On Cu(100) thermodynamics favours CN + H. Whether HCN dissociation is kinetically more facile than HCN desorption will be the subject of a

future study. We note that H_2 desorption is known to occur at lower temperature on Cu(100) (103) than on Pd(111). Thus monitoring H_2 desorption in a TPD study of HCN on Cu(100), which has not been performed to our knowledge, would provide definitive evidence whether HCN dissociates on Cu(100).

Table VI OptB86b-vdW calculated energies (in eV) for several possible states of HCN on Cu(100), Pd(111), and Ru(001).

State	Cu(100)	Pd(111)	Ru(001)
upright HCN	-0.32	-0.54	-0.91
di-σ HCN	-0.79	-1.25	-2.05
CN+H	-1.17	-1.46	-2.20
CNH_2	-0.83	-1.57	-1.80
all atoms	+0.04	-0.89	-2.80

Energy is referenced to a clean surface, gas phase HCN, and an adsorbed H atom and is calculated on (2×2) surface unit cells. CN prefers a di-σ geometry with the C-N bond axis parallel to the surface on Cu(100) and Ru(001). Multiple species in the same state are calculated at infinite separation.

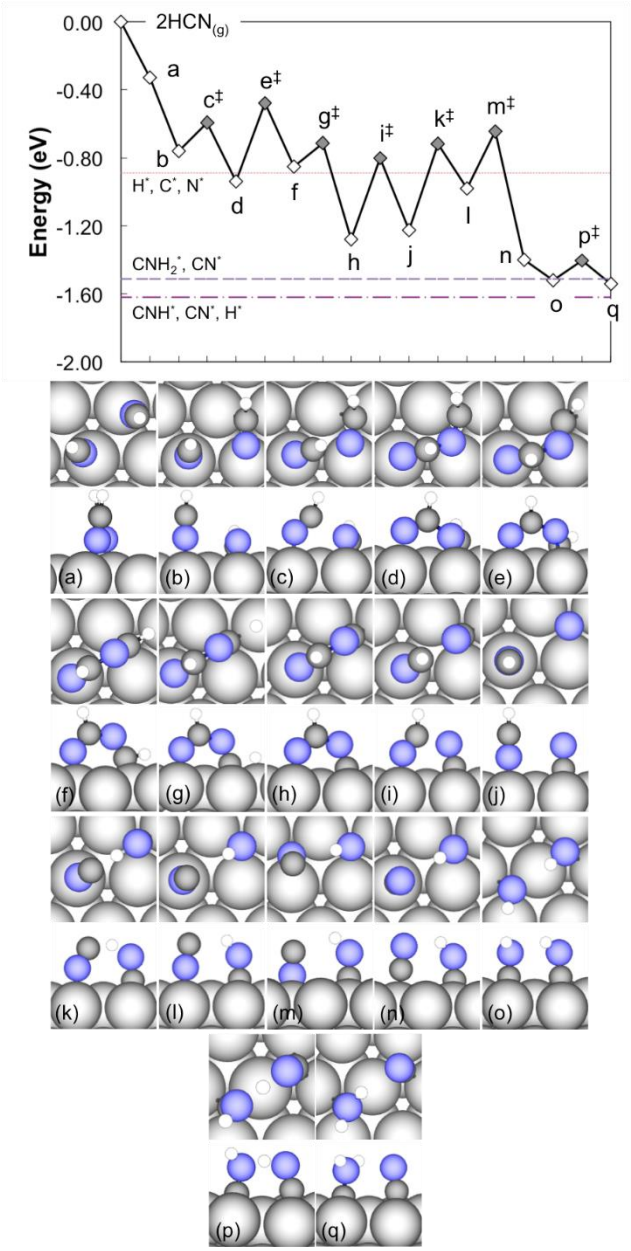

Figure 23 (Upper) DFT (optzB86b-vdw) calculated reaction energy profile for bi-molecular HCN decomposition on Pd(111) at combined 1/2 ML coverage. (a) 2 upright HCN, (b) 1 upright HCN and 1 di-σ HCN; (c) dimerization TS; (d) $(HCN)_2^{\alpha}$; (e) isomerization TS; (f) $(HCN)_2^{\beta}$; (g) dehydrogenation TS; (h) CNCHN; (i) C-N scission TS; (j) HCN and CN;[&] (k) H transfer TS; (l) NC and CNH; (m) flipping TS; (n) CN and CNH; (o) 2 CNH; (p) H transfer TS; (q) CNH_2 and CN. "‡" indicates a transition state (TS). Zero on the y-axis corresponds to a gas phase HCN molecule and an H atom adsorbed on surface. Horizontal lines correspond to indicated surface species at infinite separation from one another. Energies are ZPE-corrected DFT total energies. For brevity, balance of H atoms (at infinite separation) is not indicated. (Lower) Snapshots of the surface intermediates and transition states, with top views on top and side views on bottom. Labels correspond to those in the upper panel. Silver, blue, black, and white spheres represent Pd, N, C, and H atoms, respectively.

3.5 Discussion

The pathway that we have found for CNH_2 formation on Pd(111) from HCN allows new insights into the previously published studies on this system. The HREELS results from Kordesch et al. are similar to what we observe, but the assignments were quite different (5). For a 0.1 L HCN exposure to Pd(111) at 300 K, loss peaks were observed at 1290 and 1540 cm^{-1}, which given the HREELS resolution of 65 cm^{-1}, are close to our values of 1354 and 1564 cm^{-1}. Kordesch et al. found that the expected peak in the CH/NH stretch region was too weak to observe for low exposures at 300 K. They assigned their 1540 cm^{-1} peak to a C=N stretch and the 1290 cm^{-1} peak to the HCN bend, with the assumption that it was stiffened upon adsorption. In a separate study by the same authors, the HCN bend position was assigned to an HREELS peak at 1355 cm^{-1} (4). These values are essentially at the same position, within the margin of error, as the peaks that we observe at 1354 and 1564 cm^{-1} and assign to the ν(CN) and $\delta(NH_2)$ modes of CNH_2. We therefore conclude that the 300 K HREELS data is better assigned to CNH_2 than to a di-σ bonded HCN species. Other earlier observations are also consistent with CNH_2 on Pd(111). For example, it was noted that the same spectra were obtained from HCN absorption as from the hydrogenation of CN produced from the dissociation of cyanogen (98). On Pt(111), we showed that CN produced from cyanogen dissociation is readily hydrogenated to CNH_2, and it follows that the same reaction occurs on Pd(111) (104).

The orientation of the CN bond of the proposed di-σ bonded HCN was investigated with NEXAFS and the data indicated that the CN bond was parallel to the surface (4). For the adsorbed diatomic molecules CO, NO, and CN, the NEXAF spectra at the N 1s edge show a sharp π resonance at the threshold and a broader σ resonance at higher photon energy. The σ/π intensity ratio depends on the angle (θ_E) between the surface normal and the electric field vector and is much

larger for CO and NO than it is for CN. As the former are bonded perpendicular to the surface, it was concluded that CN was bonded parallel to the surface. They then argued that because the NEXAFS results for HCN resembled the results for CN, that the CN bond of HCN was also parallel to the surface. This is in contrast to our findings that HCN exposure at room temperature leads to both CN and CNH_2 on the surface. Although we do not detect adsorbed CN experimentally, the calculations indicate that it is oriented perpendicular to the surface, as is the CN bond of CNH_2. The calculations imply that di-σ bonded HCN should be a stable intermediate with the CN axis parallel to the surface, but there is no evidence for it from our RAIR spectra. Similar considerations would apply to an angle-resolved ultraviolet photoelectron spectroscopy (ARUPS) study (105). Spectra obtained after annealing to 200 K an HCN layer adsorbed at 110 K should have produced a mixture of CN and CNH_2. The resulting ARUP spectra display four distinct peaks and their angular dependencies were carefully characterized. However, the discussion indicated that there was some ambiguity in interpreting the results in terms of a di-σ bonded HCN with the CN bond parallel to the surface. While it is difficult to reconcile the results from NEXAFS and ARUPS with our results using RAIRS, it is possible that the former techniques detect species that are invisible to the latter.

Our findings can also provide new insights into a thorough study of the reaction chemistry of HCN on Pd(111) as studied with TPRS by Guo et al. (100) Following an HCN exposure of 2.6×10^{15} molecules/cm^2 at a surface temperature of 87 K, three desorption products were observed: HCN, H_2, and C_2N_2. Multilayer HCN was observed to desorb as two peaks (α_1 and α_2) at 118 and 131 K and monolayer HCN as a peak (α_3) at 150 K. A single higher temperature HCN desorption peak (β_1) was observed at 400 K. The latter was accompanied by reaction limited H_2 desorption (β_2). A desorption-limited H_2 peak (β_1) was observed at lower temperatures, with the exact

temperature depending on HCN exposure. Cyanogen desorption was observed in the temperature range of 500 to 750 K. No surface carbon or nitrogen was detected with Auger electron spectroscopy after cyanogen desorption, indicating that the CN bond remains intact throughout the reaction pathway. Our limited TPRS results roughly matched those of Guo et al. (100), although we were unable to detect cyanogen desorption, which was almost certainly due to a lower sensitivity in our TPRS experiments compared to theirs.

In contrast to the results obtained following HCN exposures at 87 K, high HCN exposures with the Pd(111) surface at 300 K led to the formation of a $(HCN)_x$ polymeric species (100). Upon heating, $(HCN)_x$ decomposes to liberate HCN (β_2 HCN) at temperatures as high as 800 K. The amount of β_2 HCN desorbing following 300 K exposures is much greater than observed following low temperature exposures and increases linearly with HCN exposure, indicating that it forms a multilayer polymer. Although we did not explore such a polymeric species in this study, our computational results suggesting a mechanism involving HCN dimers also reflects the tendency of the HCN molecule to form bonds with itself.

Our results can provide new insights into the origin of the β_1 HCN and β_1 and β_2 H_2 peaks observed by Guo et al.(100) We can associate the β_1 H_2 peak with the decomposition of the $(HCN)_2^{\beta}$ dimer to produce CNCHN + H, with the H atom stable on the surface until the recombinative H_2 desorption temperature is reached. Guo et al. (100) found that for the lowest exposures to the Pd(111) crystal at 300 K, β_2 H_2 occurs at 375 K and β_1 HCN at 510 K. As these peaks are associated with reaction-limited desorption, and from RAIRS we observed the disappearance of CNH_2 for annealing temperatures above 300 K, the simplest conclusion is that β_1 HCN and β_2 H_2 are associated with CNH_2 decomposition. We further assume that at low coverages, CNH_2 decomposes by the reverse of the uni-molecular mechanism to produce H, which

immediately desorbs as β_2 H_2, and adsorbed CNH. The latter is then assumed to be stable to higher temperatures, but eventually desorbs as β_1 HCN. As the coverage increases, intermolecular interactions change the energetics of various steps such that the β_1 HCN and β_2 H_2 peaks moved closer together as the coverage increased to the point where both molecules desorbed at the same temperature of 400 K.

The experimental evidence for an upright bonding configuration for HCN on Pd(111) at low temperatures is quite clear from the RAIR spectra. When van der Waals contributions are included with the optB86b-vdW functional, an isolated, weakly bound but stable upright HCN is obtained from DFT. However, the upright HCN can be stabilized in the presence of a neighboring di-σ bonded HCN (Fig. 23). This is only consistent with the experimental RAIRS results if we assume that the peaks of di-σ bonded HCN are too weak to observe. The calculated spectra imply that this would be the case. Similarly, although the experimentally implied pathway involves adsorbed CN, DFT indicates that it would likely be undetectable with RAIRS. The calculations predict two strong RAIRS peaks for the CNH intermediate, but these peaks are not observed in the experiments for HCN on Pd(111). However, on Pt(111), a peak was observed at 3348 cm^{-1}, the intensity of which rose and fell as HCN was converted to CNH_2, and was therefore attributed to the NH stretch of CNH. This peak was not accompanied by an observable CN stretch, in contrast to the DFT prediction in Fig. 20. Also, the position of the experimental 3348 cm^{-1} peak fell between that of the CH stretch of adsorbed HCN and the NH stretch of CNH_2, whereas DFT implies that the NH stretch of CNH would lie above the NH stretch of CNH_2. Coincidently, the NH stretch of CNH_2 is calculated to be at the same value as the CH stretch of upright HCN, which is not observed in the experimental spectra. The calculations predict moderately intense peaks for

both *cis*- and *trans*-HCNH, but no peaks assignable to these species are observed with RAIRS, implying that HCNH is not a stable intermediate.

3.6 Conclusions

The initial adsorption of HCN on Cu(100), Pt(111), Pd(111), and Ru(001) at temperatures below 100 K is characterized by a relatively sharp CH stretch at about 3300 cm^{-1}. This value is close to that of the gas phase and is characteristic of a CN triple bond. This implies that this peak corresponds to an HCN molecule that does not bond in a way that involves rehybridization of the carbon atom. The overall spectral characteristics indicate that this form of HCN bonds to these surfaces through the nitrogen lone pair and is oriented with the molecular axis perpendicular to the surface. DFT calculations imply that an upright HCN would be stabilized through interaction with a neighboring HCN molecule bonded with the CN axis parallel to the surface. Both the experimental and calculated RAIR spectra, including isotopic shifts, demonstrate that CNH_2 forms on Pd(111). The RAIR spectra of CNH_2 on Pd(111) are almost identical to the spectra on Pt(111). DFT calculations indicate that a bi-molecular mechanism for formation of CNH_2 from HCN with low barriers is available that can explain the observation of CNH_2 at relatively low temperatures. However, the bi-molecular mechanism involves intermediates that are not detected with RAIRS.

Chapter 4 – Deposition and Characterization of Stoichiometric Films of V_2O_5 on Pd(111)

4.1 Outline

In Chapter 4, the growth vanadium(V) oxide films on Pd(111) by physical vapor deposition and characterization with XPS, RAIRS, and LEED are presented. The experimental parameters are explained in Section 4.2. The results are described in Section 4.3 followed by an explanation in Section 4.4. Vanadium(V) oxide films grown on Pd(111) by physical vapor deposition retain their stoichiometry providing a simple and efficient method to grow V_2O_5 films for catalytic or electrochemical studies. Finally, the conclusions are stated in Section 4.5.

Portions of this chapter are reprinted from Ref. (2) with permission from Elsevier.

4.2 Experimental Methods

The experiments in this chapter were conducted in the XPS-System described in Chapter 2. The Pd(111) single crystal was spot-welded to two tantalum wires mounted on a LN_2-cooled sample holder. A type K thermocouple was spot-welded to the edge of the crystal for temperature measurement. The sample can be resistively heated to 1200 K and cooled with LN_2 to 90 K. The Pd(111) surface was prepared by Ar^+ bombardment (1 KeV, 5μA) and annealing to 1200 K in UHV. The cleanness of the surface was examined by XPS, LEED and O_2 TPD. V_2O_5 (VWR, 99.99%) powder was placed in an alumina coated tungsten basket (Midwest Tungsten Service) and was evaporated onto the sample by resistively heating to 675 °C without introducing O_2 into the chamber. A type K thermocouple was pasted to the external surface of the tungsten basket by Aremco Ceramabond 569 cement for temperature measurement.

All XPS spectra were acquired at 50 eV pass energy using Mg Kα radiation corresponding to a nominal resolution of 1.32 eV at a sample temperature of 300 K. XPS data analysis, including subtraction and peak resolution, was performed with eXPFit15.xlsm (www.chem.qmul.ac.uk/software/eXPFit15.xlsm). All XPS spectra shown in this work have been corrected by satellite and Shirley background (106) subtraction. The film thickness was estimated based on the attenuation of the Pd 3d XPS intensity due to V_2O_5 deposition using the equation:

$$\frac{I}{I_0} = \exp\left(-\frac{d}{\lambda}\right) \qquad \text{Equation 4.1}$$

where d is the film thickness, λ (2.1 nm) is the inelastic mean free path (IMFP) of a photoemitted Pd 3d electron in bulk V_2O_5 calculated via the NIST Electron Inelastic-Mean-Free-Path Database (107), and I_0 and I are the integrated intensities of the Pd 3d peaks before and after V_2O_5 deposition, respectively. The V/O ratios were determined from the integrated XPS intensity of the deconvoluted V 2p and O 1s peaks corrected by atomic sensitivity factors estimated by

$$\frac{S_1}{S_2} \approx \frac{\sigma_1 \lambda_1 / KE_1}{\sigma_2 \lambda_2 / KE_2}$$ Equation 4.2

as described elsewhere(108), where σ is the photoionization cross section of the element core level found in published data(109), *KE* is the kinetic energy of the photoemitted electron, and λ is the inelastic mean free path of the photoemitted electron. The ratio of atomic sensitivity factors for V 2p and O 1s was estimated to be 3.34, while a similar value of 2.98 was calculated from the Perkin-Elmer XPS Handbook (68). This comparison indicates that the sensitivity factor that we use is unlikely to be in error by more than ~10%.

All RAIR spectra were acquired using 1024 scans and 2 cm^{-1} resolution with a LN_2-cooled mercury-cadmium-telluride (MCT) detector at a sample temperature of 300 K. When using triangle apodization, significant interference fringes were observed. Therefore, all RAIR spectra shown have been processed with cosine 4th apodization, which smooths the spectra but also reduces the effective resolution. The corresponding RAIR spectra processed with triangle apodization are shown in the Supporting Information. Reported full width at half maxima (FWHM) were measured from the triangle apodized spectra.

All LEED patterns were taken using a beam energy of 138 eV at a sample temperature of 300 K. For the annealing experiments, the sample was heated from 300 K then held at the annealing temperature for 60 s, then cooled down to 300 K for data acquisition.

4.3 Results

4.3.1 As grown thin films at various coverages

4.3.1.1 XPS

Figure 24(a) displays the XP spectra of the sample in the V 2p, O 1s and Pd $3p_{3/2}$ regions after successive V_2O_5 depositions on Pd(111) up to a film thickness of 3.8 nm. For a clean Pd(111) surface, only the Pd $3p_{3/2}$ feature is present. For the 0.07 nm thick oxide films, a V $2p_{3/2}$ peak

appears at 515.7 eV, and an O 1s peak at 529.6 eV is seen as a weak shoulder on the lower binding energy side of the Pd $3p_{3/2}$ peak, which is slightly attenuated. With increasing film thickness up to 0.6 nm, the V $2p_{3/2}$ and O 1s peaks grow while the Pd $3p_{3/2}$ peak is further suppressed. The V $2p_{3/2}$ binding energy shifts to higher values up to 516.9 eV, while the O 1s peak shows only a small shift to 529.8 eV. For oxide films from 0.6 to 3.8 nm thick, the V $2p_{3/2}$ and O 1s peaks continue to grow accompanied by significant suppression of the Pd $3p_{3/2}$ peak. However, the V $2p_{3/2}$ and O 1s binding energies remain at about the same values.

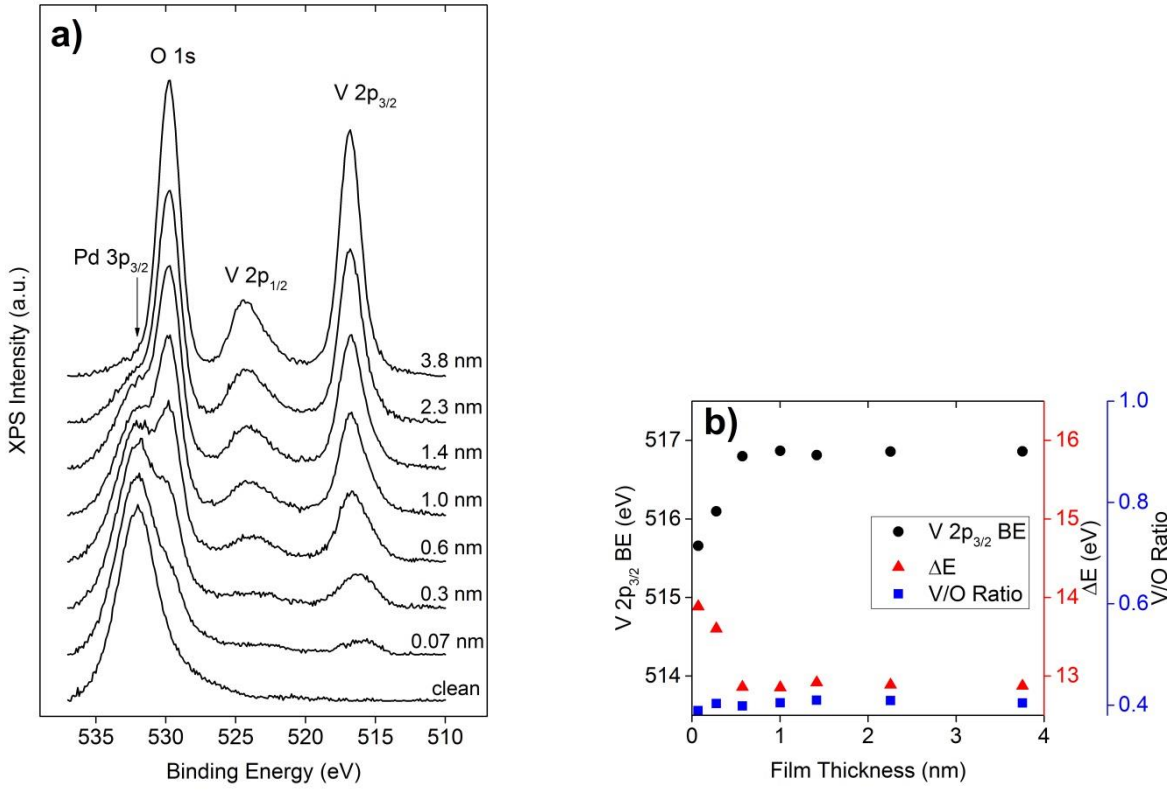

Figure 24 (a) XP spectra of the Pd $3p_{3/2}$, O 1s and V 2p region after successive V_2O_5 depositions on Pd(111). (b) Plots of the V $2p_{3/2}$ binding energy, the difference in binding energy between O 1s and V $2p_{3/2}$ (ΔE), and the V/O ratio as a function of the V_2O_5 film thickness. All spectra were acquired at 300 K and have been corrected by satellite and Shirley background subtraction.

In addition, Figure 24(b) displays plots of the V $2p_{3/2}$ binding energy, as well as the difference in binding energy between O 1s and V $2p_{3/2}$ (ΔE) and the V/O ratio obtained from the XPS data in Figure 24(a), as a function of film thickness. The value of ΔE decreases from 13.9 eV for a 0.07 nm film to 12.9 eV for a 0.6 nm film then shows no change for thicker films, which is similar to the trend in the V $2p_{3/2}$ binding energy. Unlike the V $2p_{3/2}$ binding energy and ΔE, the V/O ratio is fairly constant at around 0.40 over the full range of film thickness from 0.07 to 3.8 nm.

4.3.1.2 RAIRS

Figure 25 displays the RAIR spectra of the sample after successive V_2O_5 depositions on Pd(111) up to a film thickness of 2.3 nm. For oxide films of 0.4 nm on Pd(111), a weak and broad vibrational feature at 940 cm^{-1} and an intense peak at 1034 cm^{-1} are present. The 940 cm^{-1} feature grows without change in peak position with increasing film thickness up to 2.3 nm. The 1034 cm^{-1} peak shifts to 1039 cm^{-1} and sharpens for a 0.8 nm film. A new feature appears at 1026 cm^{-1} for a 1.2 nm film and becomes predominant for a film thickness of 2.3 nm.

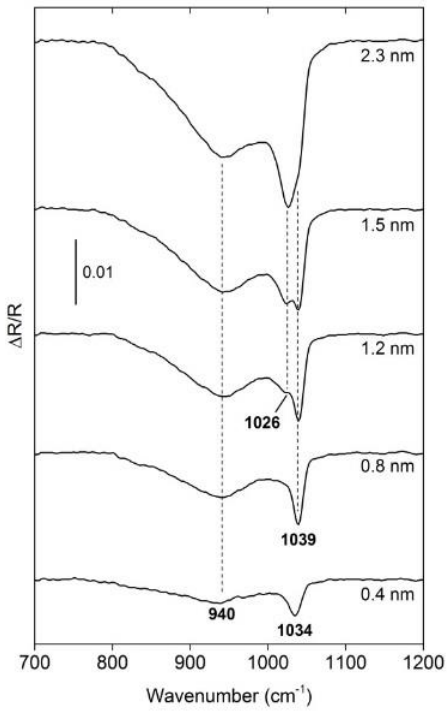

Figure 25 RAIR spectra of the sample after successive V_2O_5 depositions on Pd(111). All spectra were acquired using 1024 scans and 2 cm^{-1} resolution with an MCT detector at 300 K.

4.3.2 As-grown thin films after annealing to various temperatures

4.3.2.1 XPS

Figure 26 displays the XP spectra in the V 2p, O 1s and Pd $3p_{3/2}$ regions for 1.3 nm vanadium oxide films at 300 K, as well as the sample after annealing to 1000 K. The initial oxide film at 300 K exhibits a V $2p_{3/2}$ peak at 516.8 eV, a difference in binding energy between O 1s and V $2p_{3/2}$ (ΔE) of 12.9 eV and a V/O ratio of 0.40, which are all consistent with the results in Figure 16. Apparent changes in the V $2p_{3/2}$ feature are observed at annealing temperatures between 600 and 700 K. Upon annealing to 600 K, no obvious change is observed in the V 2p and O 1s peaks compared to those at 300 K; however, the V/O ratio slightly increased to 0.44. After the sample

was annealed to 620 K, a V $2p_{3/2}$ shoulder at 515.8 eV appears, and becomes more pronounced at annealing temperatures up to 700 K. Meanwhile, the binding energy of the main V $2p_{3/2}$ feature slightly shifts from 516.9 eV after annealing to 600 K to 517.2 eV after annealing to 700 K. Moreover, the V/O ratio gradually increases from 0.44 after annealing to 600 K to 0.50 after annealing to 700 K. After annealing the sample to 800 K, only the V $2p_{3/2}$ feature at 515.8 eV is present with a ΔE of 14.1 eV and a V/O ratio of 0.50. After the sample was further annealed to 1000 K, the spectrum yields a V $2p_{3/2}$ binding energy of 514.7 eV, a ΔE of 15.2 eV and a V/O ratio of 0.66.

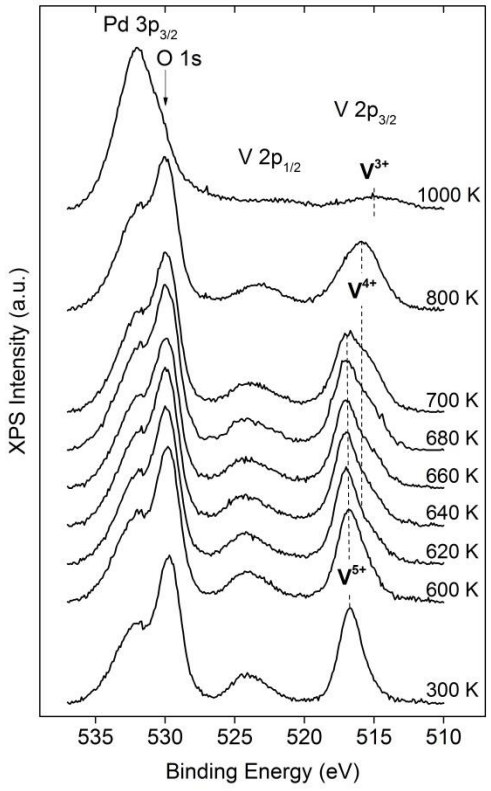

Figure 26 XP spectra of the Pd $3p_{3/2}$, O 1s and V 2p region for a 1.3 nm V_2O_5 thin film on Pd(111) at 300 K, as well as the sample after annealing to 1000 K. All spectra were acquired at 300 K and have been corrected by satellite and Shirley background subtraction.

4.3.2.2 RAIRS

Figure 27 displays the RAIR spectra of the sample for 1.3 nm thick oxide films of Pd(111) at 300 K, as well as the sample after annealing up to 1000 K. At 300 K, two main vibrational features are observed at 940 and 1039 cm^{-1}, which are consistent with the results in Figure 25. Similar to the XPS results, apparent changes are observed for annealing temperatures between 600 and 700 K. After the sample was annealed to 600 K, the intensity of the 940 cm^{-1} feature is attenuated, and the peak position shifts to 945 cm^{-1}. The 1039 cm^{-1} peak narrows from a full width at half maximum (FWHM) of 10.0 cm^{-1} at 300 K to 5.9 cm^{-1} after annealing to 600 K. After the sample was annealed to 620 K, the 945 cm^{-1} feature disappears, while the 1039 cm^{-1} peak shifts by 2 cm^{-1} to 1041 cm^{-1} with the FWHM further reduced to 4.2 cm^{-1}. In addition, two new features at 850 cm^{-1} and 1008 cm^{-1} are observed. Upon annealing at higher temperatures up to 700 K, the intensity of the 1041 cm^{-1} peak is slightly reduced without changes in peak position and FWHM, while a weak and broad feature appears at 955 cm^{-1} after annealing to 680 K. After the sample was annealed to 800 K, the 1041 cm^{-1} peak is significantly reduced and slightly broadened to a FWHM of 4.4 cm^{-1}, accompanied by reduction in the intensity of the features at 850, 955 and 1008 cm^{-1}. After the sample was further annealed to 1000 K, no peaks are observed.

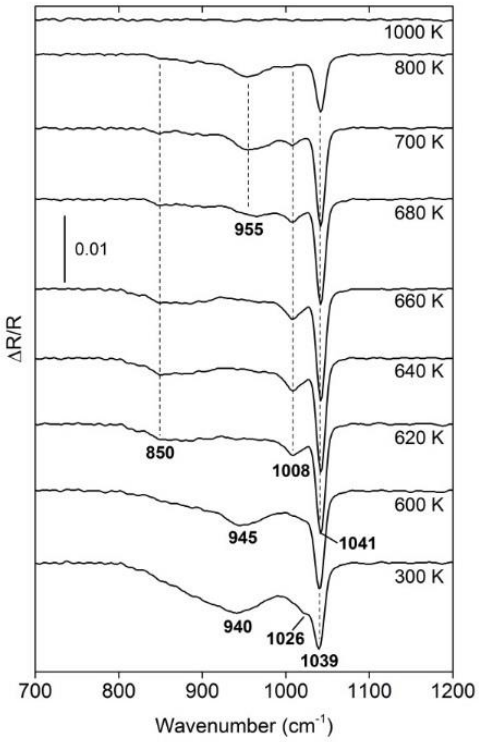

Figure 27 RAIR spectra of the sample for a 1.3 nm V_2O_5 thin film on Pd(111) at 300 K, as well as the sample after annealing up to 1000 K. All spectra were acquired at 300 K using 1024 scans and 2 cm^{-1} resolution with an MCT detector.

4.3.2.3 LEED

Figure 28 displays the LEED patterns of the sample for oxide films of 0.6 nm on Pd(111) at 300 K, as well as the sample after annealing up to 1000 K. Here we choose to present LEED patterns from the thinner 0.6 nm films instead of the 1.3 nm films investigated in XPS and RAIRS studies because 1) both films demonstrate the same results and 2) the 0.6 nm films show higher quality patterns, presumably because of weaker surface charging. A clean Pd(111) surface exhibits a sharp (1×1) LEED pattern. For the sample with a 0.6 nm thick oxide film at 300 K, a predominant diffuse background is observed, indicating that the as-grown thin films have no long range

periodicity. Similar to XPS and RAIRS results, apparent changes are observed for annealing temperatures between 600 and 700 K, where a (2×2) LEED pattern first appears. After annealing to 800 K, the (2×2) LEED pattern becomes more pronounced. After the sample was further annealed to 1000 K, a complex LEED pattern is observed consisting of the (1×1) spots from the Pd(111) substrate and additional spots forming a ring-like pattern.

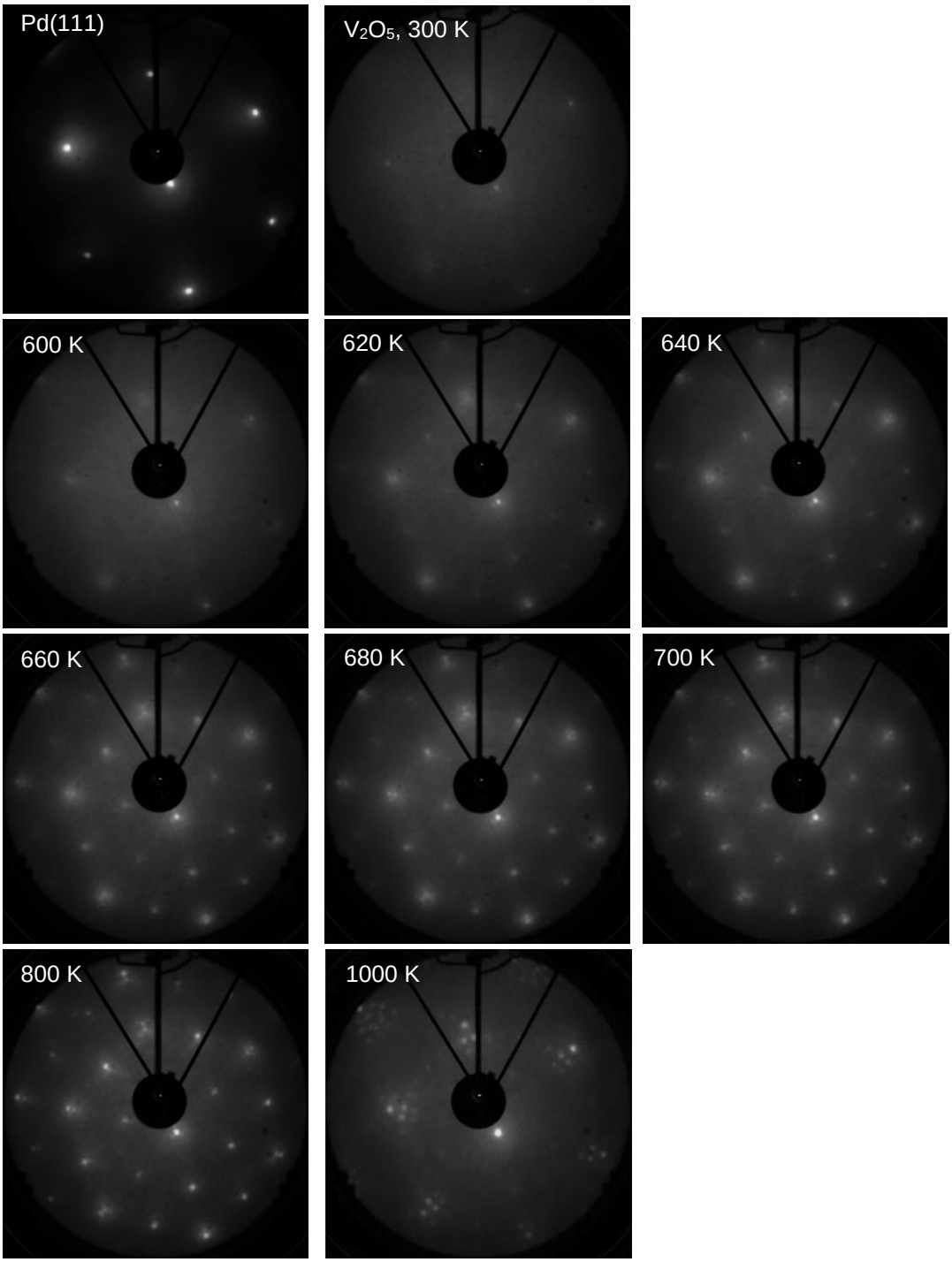

Figure 28 LEED patterns of clean Pd(111), a 0.6 nm thick V_2O_5 thin film on Pd(111) at 300 K, as well as the sample after annealing up to 1000 K. All LEED patterns were taken using a beam energy of 138 eV at 300 K. a beam energy of 138 eV at 300 K. energy of 138 eV at 300 K. a beam energy of 138 eV at 300 K.

4.4 Discussion

4.4.1 The V_2O_5 stoichiometery of the as-grown thin films

XPS has served as the primary characterization method for the stoichiometry of the vanadium oxide thin films on Pd(111). The combination of the V $2p_{3/2}$ binding energy and the difference in binding energy between O 1s and V $2p_{3/2}$ (ΔE) has been frequently used to characterize the vanadium oxidation state (110,111), while the V/O ratio has been used to establish the stoichiometry of the vanadium oxides (41).

We first consider the stoichiometry of the as-grown films with thickness $\geq$ 0.6 nm. The measured V $2p_{3/2}$ binding energy at 516.9 eV is typical for V^{5+} at 516.5 ~ 517.7 eV (34,36,41,110–113), and the ΔE of 12.9 eV is also in good agreement with those reported for V_2O_5 at 12.8 ~ 13.1 eV (110,111). In addition, the calculated XPS V/O ratio is 0.40, which perfectly matches the ideal stoichiometry of V_2O_5 (0.40). These results demonstrate unambiguously that the as-grown thin films with thickness $\geq$ 0.6 nm have the V_2O_5 stoichiometry.

The stoichiometry of the oxide films thinner than 0.6 nm requires additional consideration. For 0.07 nm thick films, the V $2p_{3/2}$ binding energy is 515.7 eV, which falls into the range of reported values for V^{4+} of 515.7 eV ~ 516.2 eV (36,41,110), suggesting that V in the as-grown films at a very low coverage is at a lower oxidation state (V^{4+}) than V^{5+}. The ΔE is 13.9 eV, which is also normally associated with the values for VO_2 of 13.7 ~ 14.4 eV. However, binding energy is not solely determined by the oxidation state. Guimond et al. (34) found the V $2p_{3/2}$ binding energy for sub-monolayer V_2O_5(001) thin films at 516.5 eV, which is 0.7 eV lower than for multilayer films. The authors argued that the V in their films was still V^{5+}, with the reduced binding energy due to an XPS final state effect where the electrons in the metal substrate provide effective screening to the XPS final state core holes of the oxides. Similar final state effects have

been reported for the growth of Nb_2O_5 thin films on $Cu_3Au(100)$ (114). Presumably, the reduced binding energy in our 0.07 nm thick films is due to similar final state effects and is therefore fully consistent with the V_2O_5 stoichiometry determined from the peak-area ratio. The same argument applies to the 0.3 nm thin film, where the XPS final state effects are weakened due to increased thickness, resulting in the shift of both the V $2p_{3/2}$ binding energy and ΔE toward the values for thicker films, while the V/O ratio stays at 0.40. Therefore, we conclude that the as-grown thin films are stoichiometric V_2O_5 in the full range of coverage investigated, while the characteristic XPS features of V_2O_5 are shown for films thicker than 0.6 nm. Assuming that the V_2O_5 film orientation is (001) on the Pd(111) substrate, a film thickness of 0.437 nm would correspond to the height of one V_2O_5 unit cell (115), which is in the thickness range of 0.3 to 0.6 nm when the film starts to show the XPS characteristics of V_2O_5. This comparison suggests that the minimum film thickness to achieve a stoichiometric monolayer of V_2O_5 is determined by the size of the V_2O_5 unit cell.

In contrast to our results, Wu et al. (41) found that the V $2p_{3/2}$ binding energy stays at 516.9 eV, characteristic of V^{5+}, in the full range of coverage for V_2O_5 thin films deposited onto highly ordered pyrolytic graphite (HOPG) by PVD. However, the graphite substrate may not affect the XPS final states to the same extent as a metal substrate. They also observed a weak V $2p_{3/2}$ shoulder around 516.0 eV in the full range of coverages and attributed it to a V^{4+} species, which suggests a small reduction of V_2O_5 in the deposition process. This feature is not present in our work.

4.4.2 Peak assignments and analysis of RAIR spectra

Two vibrational peaks at 1034 and 940 cm^{-1} are observed following the growth of 0.4 nm thick films on Pd(111). The intense peak at 1034 cm^{-1}, which gradually shifts to 1039 cm^{-1} for

thicker films, is readily assigned to the V=O stretching mode of V_2O_5 with reported frequencies at 1018 ~ 1035 cm^{-1} (116–119). A new peak at 1026 cm^{-1} appears for 1.2 nm thick oxide films, and becomes predominant for thicker films. This peak is attributed to the V=O stretching vibration mode of bulk V_2O_5.

The broad peak at 940 cm^{-1} grows without saturation with increasing V_2O_5 film thickness, and gradually diminishes at elevated temperatures and eventually disappears after annealing to 620 K. The assignment of this peak is more complicated. In the IR region of 700 ~ 1000 cm^{-1}, only a broad feature attributed to a V-O-V asymmetric stretching mode of V_2O_5 has been observed that is typically around 820 cm^{-1} (116,120), which is not a good match to the 940 cm^{-1} peak that we observe. Sanchez et al. (116) reported IR bands around 920 cm^{-1} for a V_2O_5 gel. However, the possible formation of hydrated V_2O_5 can be ruled out since we do not observe an O-H stretching mode around 3600 cm^{-1}. Magg et al. (121) observed an IR band at 945 cm^{-1} for V_2O_3/Al_2O_3 and attributed it to a $AlVO_4$ species formed at the interface of V_2O_3 and Al_2O_3. However, this is also not likely in our case since the 940 cm^{-1} feature does not saturate for thick films. Interestingly, vibrational features have been observed in Raman spectra of V_2O_5 at 900 ~ 1000 cm^{-1}. Jehng et al. (122) reported a Raman band at 920 cm^{-1} for V_2O_3/TiO_2 and V_2O_3/CeO_2 and attributed it to a polymeric V-O-V functionality. Koduru et al. (123) observed a broad Raman band at 938 cm^{-1} for amorphous V_2O_5 thin films grown at 373 K on indium tin oxide-coated flexible Kapton substrates, which is absent for crystalline V_2O_5 thin films grown at 473 K. Here we tentatively assign the 940 cm^{-1} peak to a polymeric V-O-V functionality in the amorphous V_2O_5 thin films at 300 K.

After the sample was annealed to 620 K, the V=O stretch peak at 1041 cm^{-1} is greatly sharpened, suggesting the formation of a more ordered structure. This result is supported by the evolution of a (2×2) LEED pattern in the same temperature range, which is associated with VO_2

as identified by XPS. In addition, two peaks appear at 850 and 1008 cm^{-1} along with the disappearance of the 940 cm^{-1} peak from a polymeric V-O-V functionality. The 850 cm^{-1} peak is assigned to the V-O-V asymmetric stretching mode and the 1008 cm^{-1} peak is attributed to a V=O stretch mode in VO_2 (120). These observations can reasonably result from the breakdown of polymeric V-O-V during the thermal reduction of V_2O_5 to VO_2.

4.4.3 Thermal reduction of V_2O_5 to VO_2 and V_2O_3

A few studies have been carried out concerning the thermal reduction of V_2O_5 thin films in UHV. Wu et al. (41) found that V_2O_5 on HOPG is gradually reduced due to the formation of oxygen vacancies at elevated temperatures, to a VO_2 stoichiometry after annealing to 200 °C and further to V_2O_3 after annealing to 400 °C. Ramana et al. (40) produced V_2O_5 thin films on glass and Si(100) also by physical vapor deposition of V_2O_5 powder, and observed thermal reduction of V_2O_5 above 450 °C, which yields V_2O_3 nanocrystals at 600 °C without the observation of intermediate phases such as V_6O_{13}. Guimond et al. (35) reported that V_2O_5(001) thin films on Au(111) sublimate above 500 °C. It can be seen that the thermal reduction of V_2O_5 thin films varies and is possibly influenced by multiple factors such as preparation method and substrate material.

We have also investigated the thermal reduction of the V_2O_5 thin films on Pd(111) by XPS, RAIRS and LEED. We have examined the effect of heating in small temperature increments between 600 and 700 K to observe the initial stages of the thermal reduction of V_2O_5. A V $2p_{3/2}$ shoulder around 515.8 eV on the lower binding energy side of the main V^{5+} peak appears above 600 K, which matches the reported values for V^{4+} (36,41,110), and becomes more pronounced at higher annealing temperatures. The ΔE of 14.0 eV for this feature is also typically associated with VO_2 (110,111). Both results suggest a partial reduction of V_2O_5 to VO_2 above 600 K. In addition,

the V/O ratio gradually increases from 0.40 for an ideal V_2O_5 (V^{5+}) stoichiometry at 300 K to 0.50 after the sample is annealed to 700 K, which corresponds to an ideal VO_2 (V^{4+}) stoichiometry. However, both V^{5+} and V^{4+} are identified following annealing to 700 K from the V $2p_{3/2}$ peak. This result suggests that the thermal reduction of V_2O_5 occurs by the loss of oxygen from the V_2O_5 structure while retaining the V^{5+} oxidation state, which is in agreement with the conclusion by Wu et al. (41).

Significant changes are also observed with RAIRS and LEED between 600 and 700 K. In this annealing temperature range, the RAIRS feature attributed to ν(V=O) is greatly sharpened, and a (2×2) LEED pattern emerges, both suggesting the formation of more ordered surface structures compared to the as-deposited amorphous V_2O_5 thin films.

After the sample was annealed to 800 K, the V $2p_{3/2}$ feature attributed to VO_2 is predominant in XPS with a distinct (2×2) LEED pattern, suggesting that the initial V_2O_5 thin films have been completely reduced to an ordered form of VO_2. Upon further annealing to 1000 K, only a V $2p_{3/2}$ feature around 514.7 eV is observed with XPS. The V $2p_{3/2}$ binding energy is slightly lower but fairly close to the reported values for V^{3+} at 515.0 eV ~ 515.7 eV (27,30,36,37,41,110,111), while the ΔE of 15.2 eV for this feature is also typically associated with V_2O_3 (110,111). In addition, the V/O ratio of 0.66 matches the ideal V_2O_3 stoichiometry of 0.67. Along with the observed complex, ring-like LEED pattern, these results suggest that the initial V_2O_5 thin films have been further reduced to an ordered form of V_2O_3. Based on the slight attenuation of the Pd 3d signal, the V_2O_3 film thickness was estimated to 0.07 nm. A value this low presumably corresponds to submonolayer coverage of V_2O_3 and implies that V_2O_3 is probably present as small patches or islands surrounded by bare Pd.

In the work by Leisenberger et al. (27) on the thermal reduction of V_2O_3 thin films on Pd(111), they found with XPS that the films were reduced to a stoichiometry of VO and exhibited a (2×2) LEED pattern after annealing to 350 °C. The films were further reduced to V/Pd alloys with a ring-like LEED pattern after annealing to 500 °C. In comparison, the V_2O_5 thin films in this work can only be thermally reduced to a stoichiometry of V_2O_3, while demonstrating similar trends in surface reconstruction. Our finding that V_2O_5 is reduced at elevated temperatures to lower oxides, but not to vanadium metal, may be of advantageous for catalytic applications.

4.5 Conclusion

Stoichiometric, amorphous V_2O_5 thin films were grown on Pd(111) at 300 K through physical vapor deposition by heating a fine powder of V_2O_5 in a non-oxidative, UHV environment. The V_2O_5 thin films thermally reduce to an ordered form of VO_2 in the range of 620 - 800 K, and further reduce to an ordered form of V_2O_3 below 1000 K.

Chapter 5 - Oxidative desulfurization of dibenzothiophene on V_2O_5 thin films

5.1 Outline

The use of the as-grown V_2O_5 thin films in the oxidative desulfurization of dibenzothiophene is presented in this chapter. Section 5.2 describes the variety of UHV surface analysis techniques used to analyze the oxidation reaction. Section 5.3 presents the preliminary results of this project. Finally, section 5.4 contains the conclusions drawn from the experiments conducted thus far. The results presented in this chapter are part of an ongoing study that will be considered for publication once more results are obtained. The goal of this chapter is to provide a record of the current progress to inspire the continuation of this study.

5.2 Experimental

The experiments were conducted in the XPS-System described in Chapter 2. Thiophene (≥99%) and dibenzothiophene (≥99%) were purchased from Millipore Sigma and used without further purification. Solid dibenzothiophene was inserted into a small section of the gas manifold accessible by a 1.33" CF flange. Heating the manifold to 383 K provided a sufficient vapor pressure for introducing dibenzothiophene into the analysis chamber. Thiophene in its liquid state did not require heating of the gas manifold. RAIRS was performed as described elsewhere (2). TPD spectra were collected at a linear heating rate of 1.5 K s^{-1}. XPS spectra were collected at 90 K using a 50 eV pass energy and Mg Kα radiation. The XPS spectra were processed as previously described (2).

5.3 Preliminary Results

5.3.1 Interactions between DBT and Pd(111)

The experimental results presented in this section are part of an ongoing study and may require further interpretation. XPS, TPD, and RAIRS were used to identify the formation of Ar-S=O and $Ar(S=O)_2$ species formed by oxidation of thiophene and DBT from V_2O_5. First, the interaction of DBT with the Pd(111) substrate was studied. Figure 29 shows XP spectra of increasing coverage of DBT on Pd(111). DBT adsorbs to Pd(111) at 86 K indicated by the presence of the C 1s and S 2p features in the XPS spectra. The S/C ratio is 0.08 after a 22 L exposure indicating that stoichiometric ($C_{12}H_8S$) DBT is present on the surface. The S 2p binding energy is the same as that reported in the NIST database (124) for DBT indicating no perturbation of the sulfur electronic state upon adsorption. Following a 32 L exposure the S/C ratio increases to 0.10 which provides $C_{10}S$ stoichiometry. The peak positions for C 1s and S 2p remain constant as

exposure increases indicating that no reaction is taking place between adsorbed DBT on Pd(111) at 86 K.

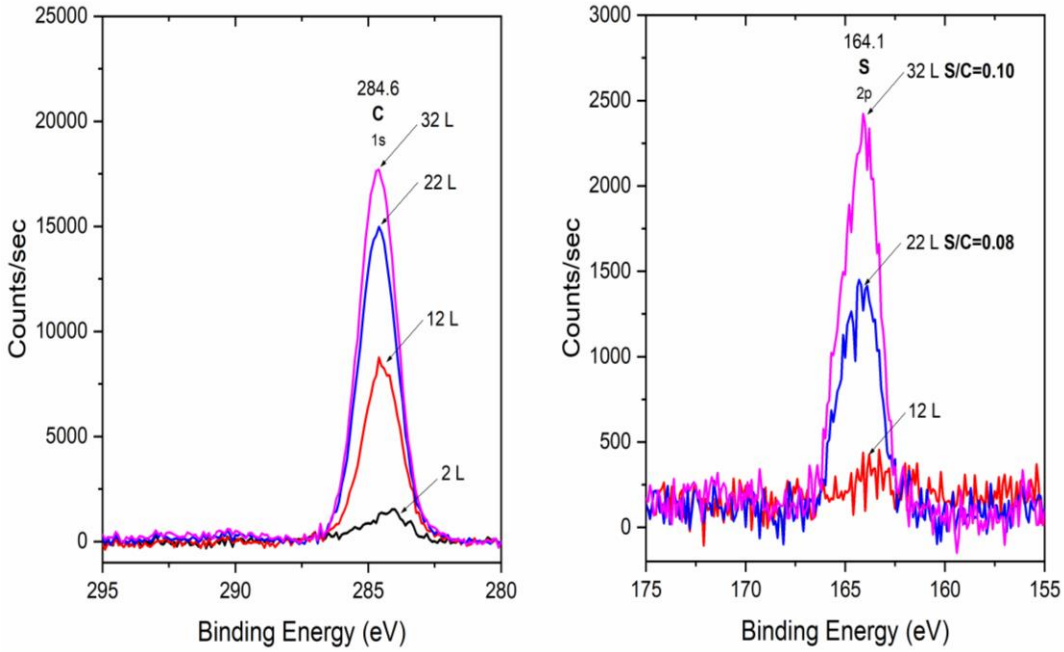

Figure 29 XP spectra of the DBT C 1s and S 2p regions after sequential deposition of DBT on Pd(111). All spectra were acquired at 86 K and corrected with satellite and Shirley background subtraction.

The bonding geometry of DBT to Pd(111) can be inferred from the vibrational spectra presented in Figure 30. The RAIR spectra show features at 701 and 747 cm^{-1} at low exposures that are attributed to the out of plane aromatic ring bending and δ(Ar-H) modes of DBT. As the exposure is increased, small features at 1027, 1075, 1231, and 1315 cm^{-1} are detected. These features are possible CC and CS stretch modes related to aromatic compounds. The δ(Ar-H)

feature at 747 cm^{-1} continues to intensify at higher exposures. The increasing intensity is possibly due to DBT at sub-monolayer coverages. Further experiments would be needed to determine if multilayer desorption occurs below 150 K.

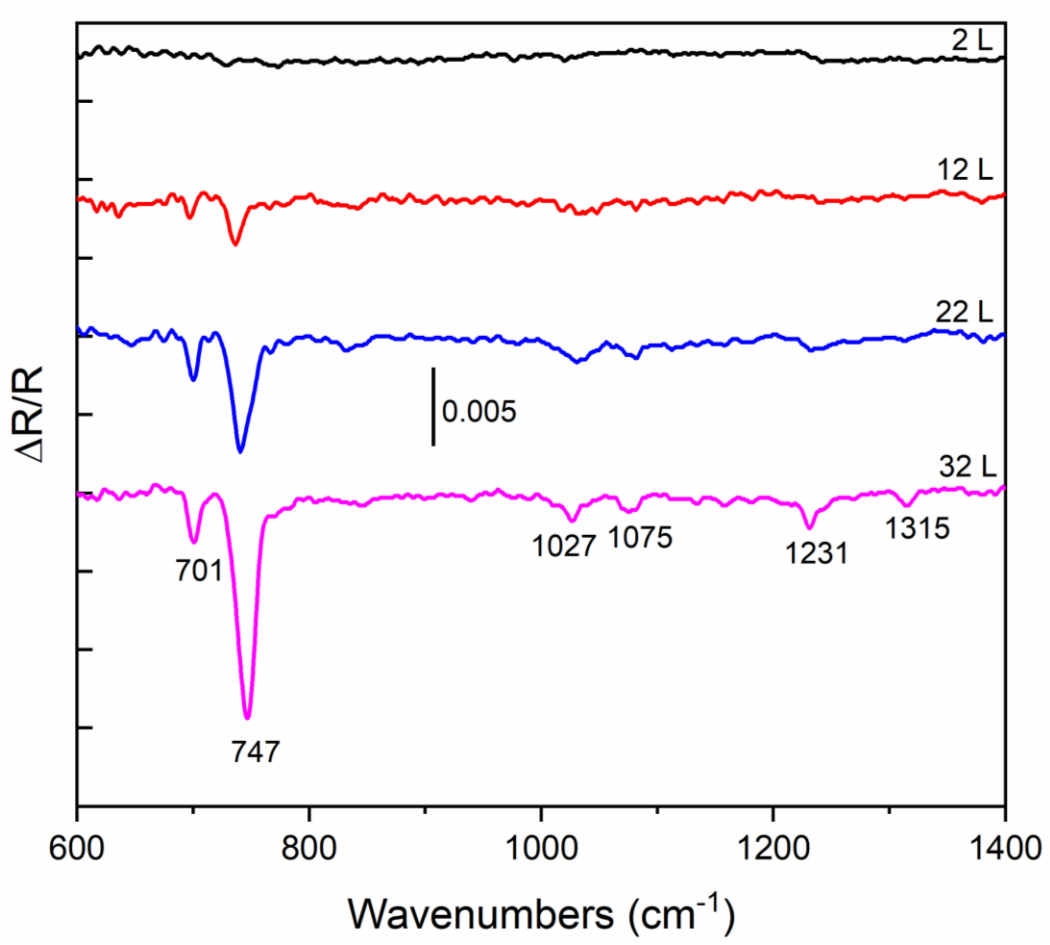

Figure 30 RAIR spectra of sequential exposures of DBT on Pd(111) taken at 86 K using 1024 scans and 4 cm^{-1} resolution.

Thermal desorption spectra are presented in Figure 31. The spectra were collected to determine the strength of the Pd-DBT interaction and to identify any possible decomposition products. The most intense unique desorption peak detected for DBT occurred at 92 amu which appears at half the parent mass (184 amu) and is attributed to the DBT^{++} fragment. Only one desorption peak is observed in the range of 90 to 1000 K. This desorption peak occurs at 150 K and is attributed to molecularly adsorbed DBT. Other masses of interest include 18, 28, 16, 32, and 64 amu. A possible assignment of the 64 amu feature is SO_2 which is desired from the oxidation of DBT. However, the peak detected at 64 amu is not due to the formation of SO_2 since there is neither a sulfur feature at 32 amu nor an oxygen feature at 16 amu. The 18 and 28 amu traces are attributed to H_2O and CO, respectively. The desorption peaks for H_2O and CO may be due to the background gases adsorbed to the DBT adlayers, which would be a plausible explanation for their desorption at the same temperature as DBT. The 64 amu trace is monitored as it is the major peak in the mass spectrum of SO_2; however, in the absence of a bountiful oxygen source, the 64 amu trace in Figure 23 is attributed to a C_xH_y fragment of DBT. A small feature with a 10% intensity relative to 92 amu is present at 64 amu in the mass spectrum of DBT (125).

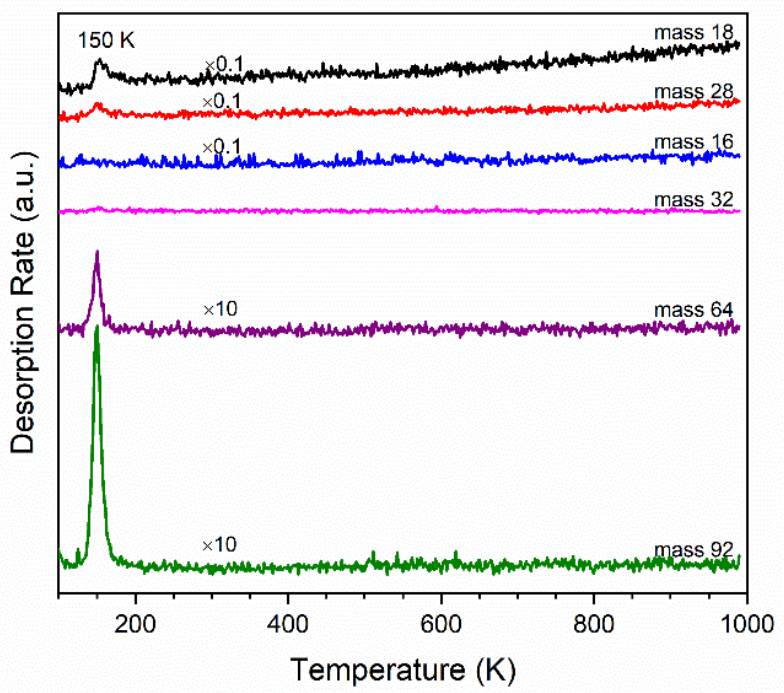

Figure 31 TPD spectra of 15 L DBT from Pd(111) heated linearly at a rate of 1.5 K s^{-1}. A single desorption feature at 150 K appears from the interaction of DBT with Pd(111).

5.3.2Interactions between DBT and V_2O_5 thin films

V_2O_5 is a desirable oxidizing agent because vanadium can easily transition between its five oxidation states. Reduction of V_2O_5 to VO_2 or V_2O_3 can be done by oxygen transfer from the thin film to DBT forming the sulfoxide (DBTO) or sulfone ($DBTO_2$) derivatives. XPS spectra of DBT annealed over V_2O_5 thin films are presented in Figure 32. The V_2O_5 thin film was annealed at 700 K for 1 minute before the addition of DBT. Some reduction of V^{5+} to V^{4+} was detected as indicated by the presence of a shoulder in the V $2p_{3/2}$ peak. DBT was deposited and a single C 1s peak is observed indicating that only one oxidation state of carbon exists at 90 K. The Pd, O, and V peaks decrease in intensity as layers of DBT inhibit photoelectrons from escaping the deeper layers of the system. After annealing to 200 K for 1 minute, a small amount of carbon is detected, and the

V $2p_{3/2}$ peak is broadened. Broadening of the V $2p_{3/2}$ peak after annealing the DBT covered film at 200 K indicates the possibility of oxygen transfer to DBT; however, no S 2p peak was detected to confirm if any oxidation occurred.

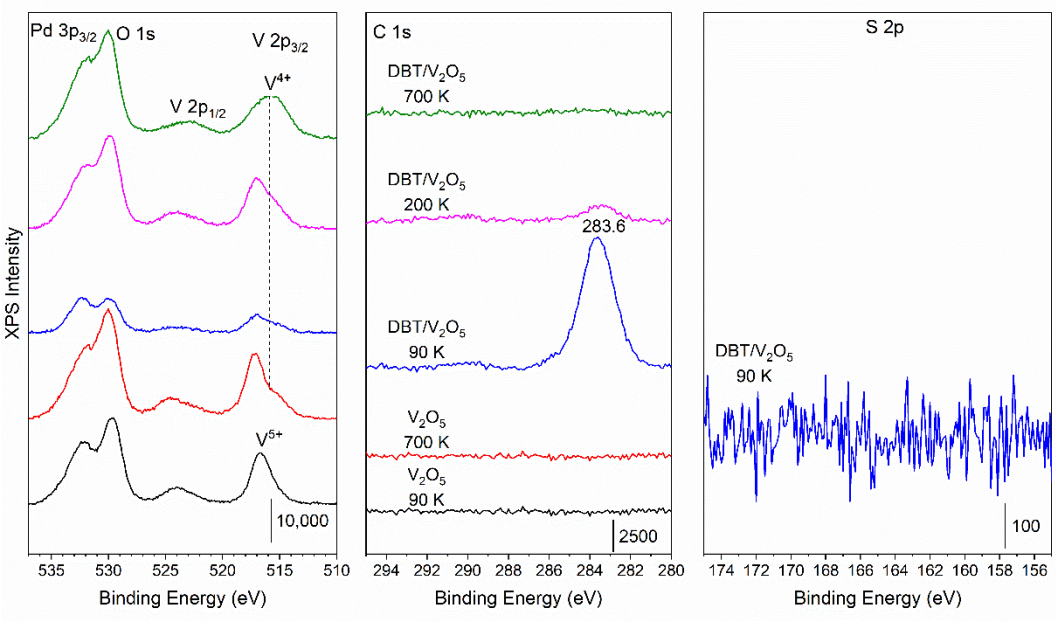

Figure 32 XPS spectra of V_2O_5 on Pd(111) and 40 L DBT on V_2O_5 taken at 90 K with 50 eV pass energy and Mg Kα radiation annealed at the indicated temperatures for 1 minute.

To probe this further, RAIRS was used as sulfoxide ($R_2S=O$) and sulfone ($R_2(S=O)_2$) functional groups exhibit strong infrared absorption features. Figure 33 shows corresponding RAIR spectra for DBT deposited on the V_2O_5 film. The DBT vibrations present at 40 L are similar to those of DBT deposited on Pd(111). Cao et al. (126) recently reported that DBT oxides were formed from reactions of DBT with H_2O_2 and a $NiMoO_3$ catalyst. They reported $DBTO_2$

(dibenzothiophene sulfone) FTIR peaks at 1286 and 1168 cm^{-1} and a DBTO (dibenzothiophene sulfoxide) peak at 1047 cm^{-1}. When annealed at 200 K and above, all DBT features in the RAIR spectrum disappear coinciding with a desorption temperature of 150 K.

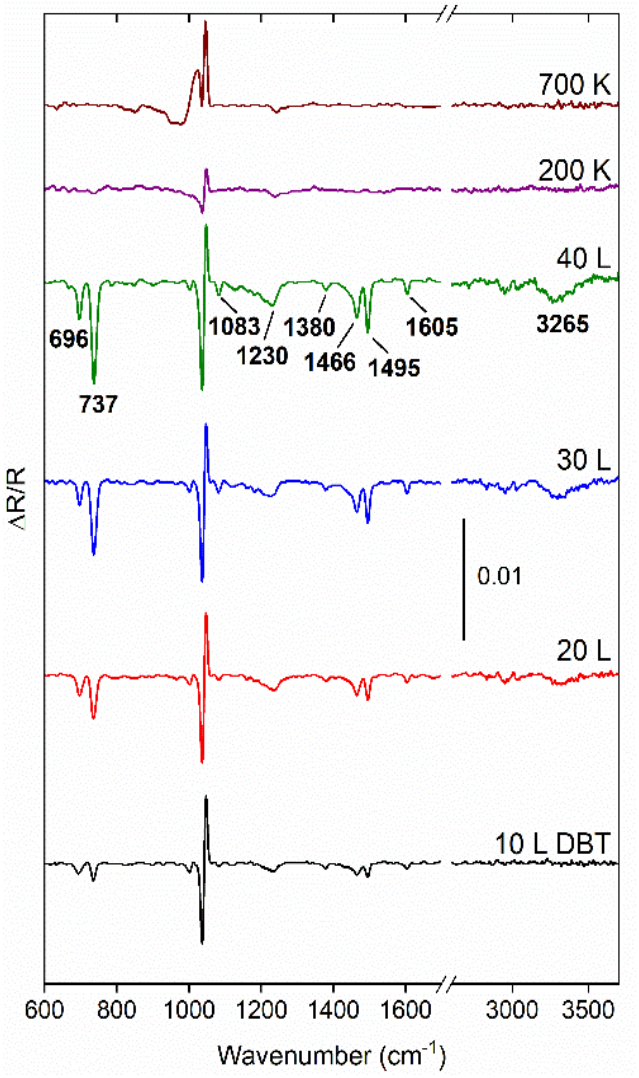

Figure 33 RAIR spectra of increasing DBT exposure on V_2O_5 covered Pd(111). The spectra were collected at 90 K with 1024 scans and 4 cm^{-1} resolution. The interferogram spectra were referenced against a V_2O_5 covered Pd(111) background. The artefact at ~1030 cm^{-1} is a result of the changes in the ν(V=O) mode when DBT is deposited.

TPD spectra of bare and DBT covered V_2O_5 films are presented in Figure 34. Heating the V_2O_5 film above 200 K produces a small peak corresponding to O_2 evolution. Background H_2O and CO desorption is also observed from the bare V_2O_5 film. DBT (92 amu) desorbs from the V_2O_5 film at 150 K indicating a weak interaction between V_2O_5 and DBT. While S (32 amu) and SO_2 (64 amu) are also observed at 150 K, this temperature is below the thermal reduction temperature of V_2O_5 on Pd(111) as described in our previous work (2) leading to the conclusion that the observed 32 and 64 amu features are fragments of DBT instead of oxidation products. Using isotopically labeled $V_2{}^{18}O_5$ thin films would shift the O_2 and SO_2 traces to 36 and 68 amu respectively, which would clarify if the 64 amu signal is due to SO_2 production or the fragmentation of DBT.

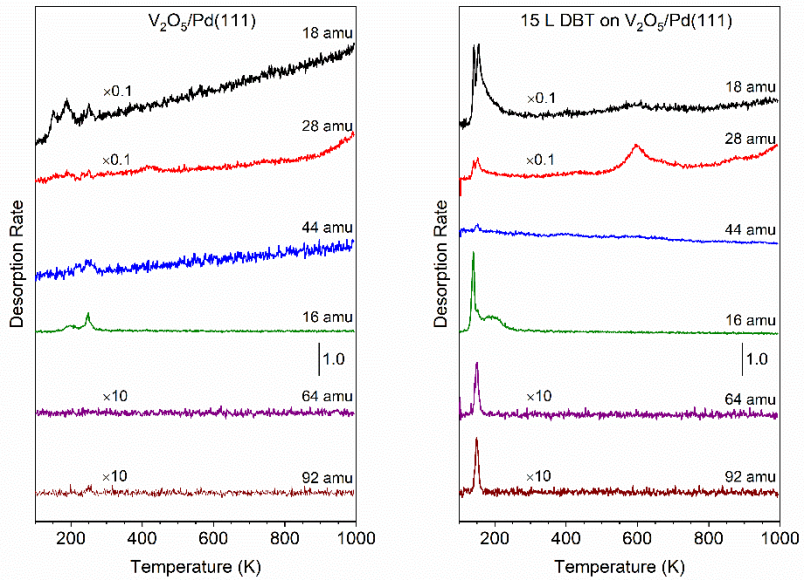

Figure 34 TPD spectra of bare and DBT covered V_2O_5 films collected with a heating rate of 1.5 K s^{-1}.

5.3.3 Interactions of Thiophene with Pd(111) and V_2O_5 Thin Films

In the previous section, it was observed that DBT has weak interactions with Pd(111) and V_2O_5 thin films. We concluded that the non-bonding S electron pairs were strongly delocalized by the large aromatic compound; therefore, the interactions of the simplest aromatic sulfur compound, thiophene (C_4H_4S), with Pd(111) and V_2O_5 thin films were studied. The thermal desorption spectra in Figure 35 indicate a weak interaction between thiophene and both Pd(111) and the V_2O_5 films. Thiophene exhibits a single desorption peak at ~140 K indicating no decomposition or other reactions occur with the Pd substrate or the V_2O_5 film.

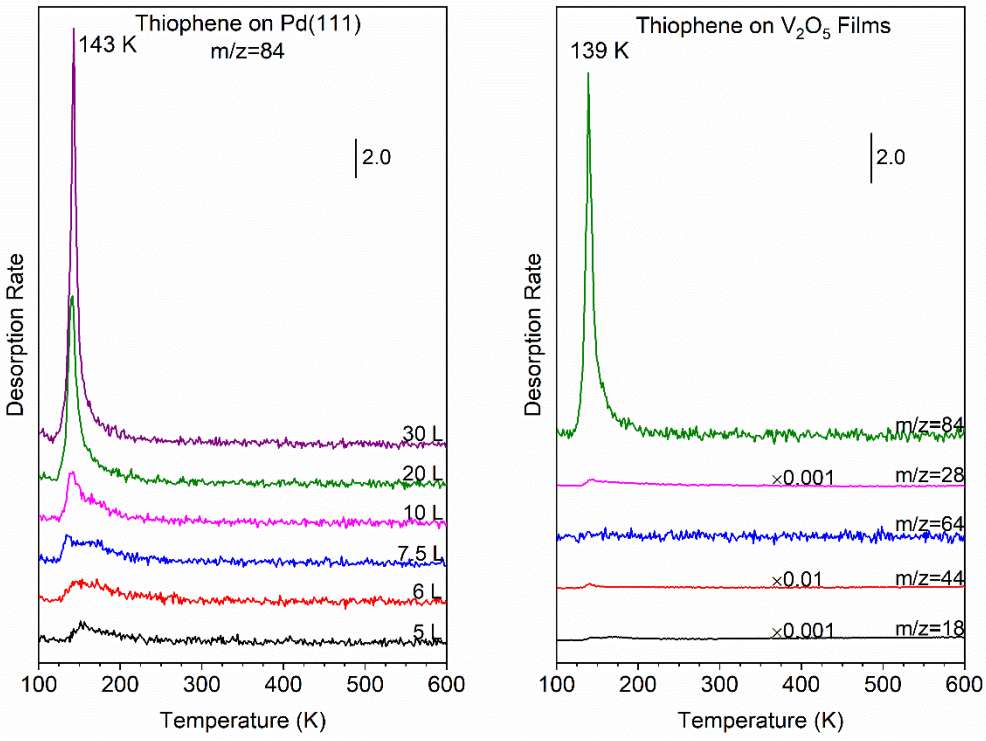

Figure 35 TPD of increasing exposures of C_4H_4S on Pd(111) and 20 L of C_2H_4S on 0.7nm V_2O_5 film. Both spectra were collected at a heating rate of 1.5 K s^{-1}.

Figure 36 displays the XP spectra of thiophene on the Pd(111) surface and V_2O_5 film. The S 2p peak of DBT was observed at 164.1 eV on Pd(111). However, the S 2p peak of thiophene was detected on both the Pd substrate and the V_2O_5 films. The S 2p peak position was observed at 163.9 eV on Pd(111) and 163.1 eV on a 0.7 nm thick V_2O_5 film. Both of these energies are lower than the reported value of 164.3 eV (124) indicating a perturbation of the electronic state of the sulfur atom. This observation implies that the electron density around sulfur becomes more delocalized upon adsorption. The greater effect of the bare Pd substrate on the S 2p binding energy demonstrates a greater overlap between the sulfur electron density and the metal surface. Either higher exposures of DBT or the same exposure of DBT to increasing V_2O_5 film thickness would aid in the determination of a screening effect from the vanadium oxide film.

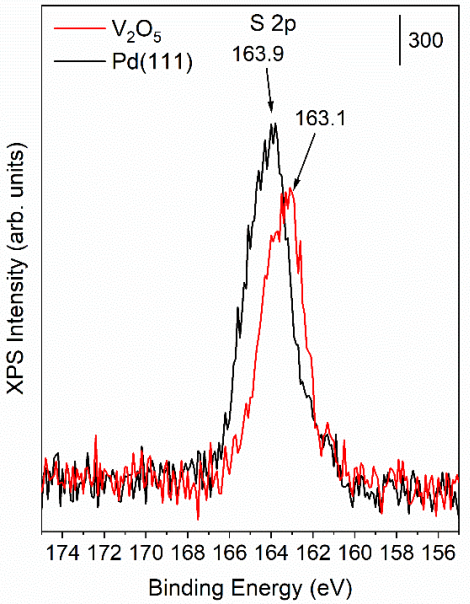

Figure 36 XPS spectra of 20 L C_4H_4S on the Pd(111) substrate and a 0.7nm V_2O_5 film. The spectra were collected at 90 K with a 50 eV pass energy and Mg Kα radiation and corrected by satellite and Shirley background subtraction. a 0.7nm V_2O_5 film. The spectra were collected at 90 K with a 50 eV pass energy and Mg Kα radiation and corrected by satellite and Shirley background subtraction.

Figure 37 shows RAIR spectra of thiophene before and after sputtering with O_2 for 15 minutes. The main features at 668 cm^{-1} is due to background CO_2 in the optical bench. The peak at 1045 cm^{-1} is due to the V=O stretching mode from the partially reduced V_2O_5 film. Thiophene IR peaks are seen after depositing 20 L of thiophene on the V_2O_5 film. The peaks at 730, 835, 1250, 1405, and 3107 cm^{-1} are assigned to the out-of-plane CH bending, out-of-plane ring bending, in-plane CH bending, CS stretching, and CH stretching modes, respectively. After sputtering with O_2 for 15 min, no sulfur oxide vibrations were detected. The intensity of the thiophene peaks did not change dramatically, indicating that O_2 sputtering had little to no effect on the thiophene layers.

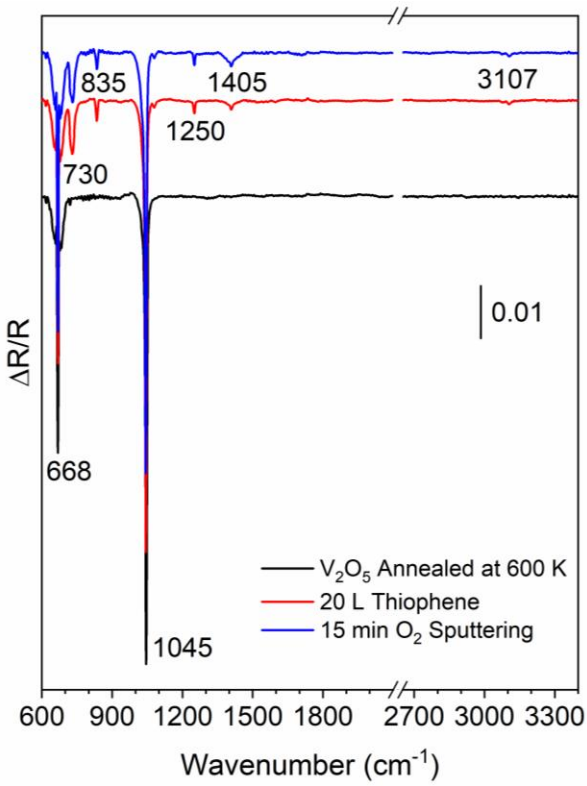

Figure 37 RAIR spectra of V_2O_5 after partial reduction (black), exposure to thiophene (red), and after 15 minutes of sputtering 4×10^{-8} Torr of O_2 at 1.5 kV. No sulfur oxides were detected by RAIRS after O_2 sputtering.

5.4 Conclusions

Oxidative desulfurization of dibenzothiophene and thiophene with V_2O_5 thin films was investigated. Thermal desorption spectra indicate a weak adsorption of DBT or thiophene to Pd(111) and V_2O_5. DBT desorbs from both surfaces at ~150 K and thiophene desorbs at ~140 K. RAIR spectra show no evidence of a reaction between the thiophenes and the surfaces, and XPS spectra show no change in the C 1s peak of DBT. The S 2p peak of thiophene shifts to lower binding energy by 0.8 eV on the V_2O_5 film and 1.5 eV on Pd(111) leading to the conclusion that there is an interaction between sulfur and Pd(111) that is inhibited by V_2O_5. As of this writing, no oxidation was observed; therefore, future studies are required to determine if V_2O_5 is capable of oxidizing thiophenes. Possible future experiments include oxidation in a background of stronger oxidizing agents such as O_2 or NO_2, isotopic substitution of thiophenes or V_2O_5 to deconvolute vibrational features and mass spectrometer traces, varying the thickness of V_2O_5 to determine if thiophene interacts with vanadium(V) oxide or with the Pd(111) substrate below the thin films.

Chapter 6 – Propyne hydrogenation over a Pd/Cu(111) single atom alloy catalyst studied with infrared spectroscopy

6.1 Outline

The partial hydrogenation of propyne to propylene over a SAA Pd/Cu(111) surface is presented in Chapter 6. Section 6.2 describes the experimental methods. The results are presented and discussed in Section 6.3. Finally, the conclusions are stated in Section 6.4.

6.2 Experimental Methods

The experiments in this chapter were conducted in the AP-RAIRS system described in Chapter 2. The IR experiments were conducted using a Bruker Vertex 70v spectrometer with an external mercury cadmium telluride (MCT) detector. Polarization dependent RAIRS (PD-RAIRS) was used to differentiate between peaks due to gas phase species from peaks associated with species adsorbed on the surface. At ambient pressures, *p*-polarized RAIR spectra contain vibrations from both adsorbed and gas phase molecules. These spectra are labeled as *p*-Absorbance. By using a rotatable polarizer, *s*-polarized spectra sensitive only to gas phase species are obtained, labeled as *s*-Absorbance. Subtracting the *s*-polarized spectrum from the *p*-polarized spectrum yields a spectrum representing vibrations of molecules adsorbed on the surface, which is labeled simply as Absorbance. According to the RAIRS selection rule, only vibrations that result in a change in dipole moment along the surface normal can be detected (66).

Absorbance is used instead of reflectance to provide a linear correlation between partial pressure and IR intensity for the gas phase species. A ten-point calibration curve was generated for propyne and propene by acquiring IR spectra as a function of pressure in 0.1 Torr increments up to 1.0 Torr. The results are presented in the supporting information. By isolating the sample in the IR cell, we can treat the latter as a small (1.2 L) reaction vessel. Its volume was determined from the expansion of a known pressure and volume of argon into the IR cell and calculated using the ideal gas law. From the volume and pressure derived from the gas phase IR intensities, the absolute amounts of propene and propyne present in the cell during hydrogenation were obtained. The Cu(111) crystal (99.9999%, Princeton Scientific) was cleaned with repeated Ar^+ ion bombardment at 800 K (1 kV) followed by annealing at 950 K. The surface was considered clean when only Cu Auger peaks were detectable. Pd deposition was performed by resistively heating

a Pd wire as described elsewhere (127). Pd coverages were determined based on AES. The existence of a single atom alloy occurs at low Pd coverages as described elsewhere (127).

TPD spectra were collected at a heating rate of 1.5 K/s. AES spectra were collected with a beam energy of 2500 eV. RAIR spectra were obtained with 1024 scans and 4 cm^{-1} resolution. For the adsorption studies, the catalyst was prepared and transferred to the IR cell, and the cell was subsequently pressurized with the reactant mixture (50 mTorr of propyne and 150 mTorr of H_2). The catalyst was annealed at various temperatures for one minute then cooled to room temperature for spectrum acquisition. The same reactant pressures were used to study the adsorption of propene on Cu(111) and Pd/Cu SAA under ambient pressure conditions. The hydrogenation reactions were conducted using 500 mTorr of propyne and 1500 mTorr of H_2 at a constant temperature to study catalyst lifetime and perform a kinetic analysis for the reaction over the Cu(111) and Pd/Cu(111) SAA surfaces. Propyne (≥99.9%), propene (≥99.9%), and propane (99.97%) were purchased from Millipore Sigma and used without further purification.

6.3 Results and Discussion

6.3.1 Propyne interaction with Cu(111) and Pd/Cu(111)

Figures 38 and 39 show RAIR spectra from 800 to 1700 cm^{-1} and from 2700 to 3200 cm^{-1}, respectively, for Cu(111) and 2% Pd/Cu(111) in the presence of 50 mTorr of propyne and 150 mTorr of H_2 at room temperature (300 K) and after annealing to the indicated temperatures. In Figure 38, the 300 K spectrum is dominated by a single peak at 1360 cm^{-1}. The negative peak just below 950 cm^{-1} is an artifact. In Figure 39, the 300 K spectrum features three strong peaks in the C-H stretch region at 2823, 2850, and 2883 cm^{-1}. Essentially the same spectrum was reported by Chesters and McCash for propyne adsorbed in UHV on Cu(111) at 150 K (128). They found that propyne adsorbs as a monolayer at 150 K, and desorbs without reaction at 270 K. They found that

propyne multilayers formed for exposures at 120 K. They concluded that propyne bonds to Cu(111) in di-σ/di- π fashion with the $C_1 \equiv C_2$ bond parallel to the surface and with the alkynic hydrogen and methyl group tilted away from the surface. This structure, shown in Figure 40, was confirmed through a subsequent photoelectron diffraction study (129) as well as by later DFT calculations (130–133). Chesters and McCash concluded that the 1360 cm^{-1} peak was due primarily to the C_1-C_2 stretch as it shifted from 1361 to 1353 cm^{-1} when CH_3CCH was replaced with CH_3CCD, whereas they expected essentially no shift if it were assigned to the CH_3 deformation mode (128). In contrast, in a RAIRS study of propyne on Cu(110), Roberts et al. (134) showed that a 1354 cm^{-1} peak seen for CH_3CCH shifts to 1072 cm^{-1} for CD_3CCH, which led them to conclude that the peak is best assigned to a $\delta(CH_3)$ mode. In fact, the peak that we observed at 1360 cm^{-1} corresponds to a normal mode with mixed C_1-C_2 stretch and $\delta(CH_3)$ character, as confirmed by the DFT calculations of the RAIR spectrum of propyne on Cu(111) by Valcárcel et al. (132). In the C-H stretch regions, we follow Chesters and McCash (128) and assign the peaks at 2823, 2850, and 2883 cm^{-1} to the overtone of $\delta_{asym}(CH_3)$, the alkynic C-H stretch, and the symmetric CH_3 stretch, respectively.

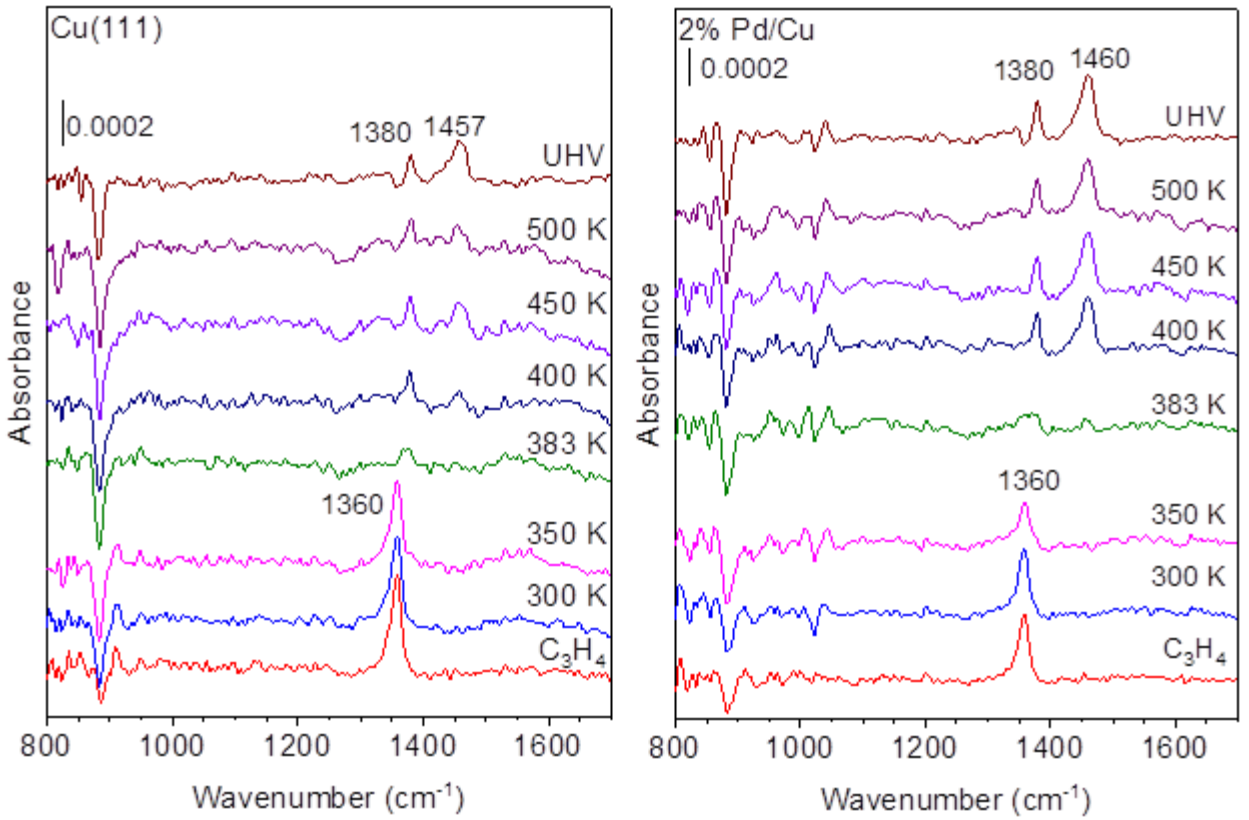

Figure 38 PD-RAIR spectra of 50 mTorr of propyne (red) followed by 150 mTorr of H_2 (blue) exposed to Cu(111) (left) and 2% Pd/Cu(111) (right) at 300 K and after annealing at the indicated temperatures for one minute.

Our observation of the same RAIR spectrum of propyne on Cu(111) at room temperature as observed by Chesters and McCash (128) at 150 K indicates that it has the same di-σ/di-π structure in both cases. Although under UHV conditions propyne desorbs from Cu(111) at 270 K, under an ambient pressure of 50 mTorr, the adsorbed state is evidently in equilibrium with gas-phase propyne. At 300 K, neither the presence of 150 mTorr of H_2 in the gas phase nor of 2% Pd on the Cu(111) surface appears to have any effect on the structure on adsorbed propyne.

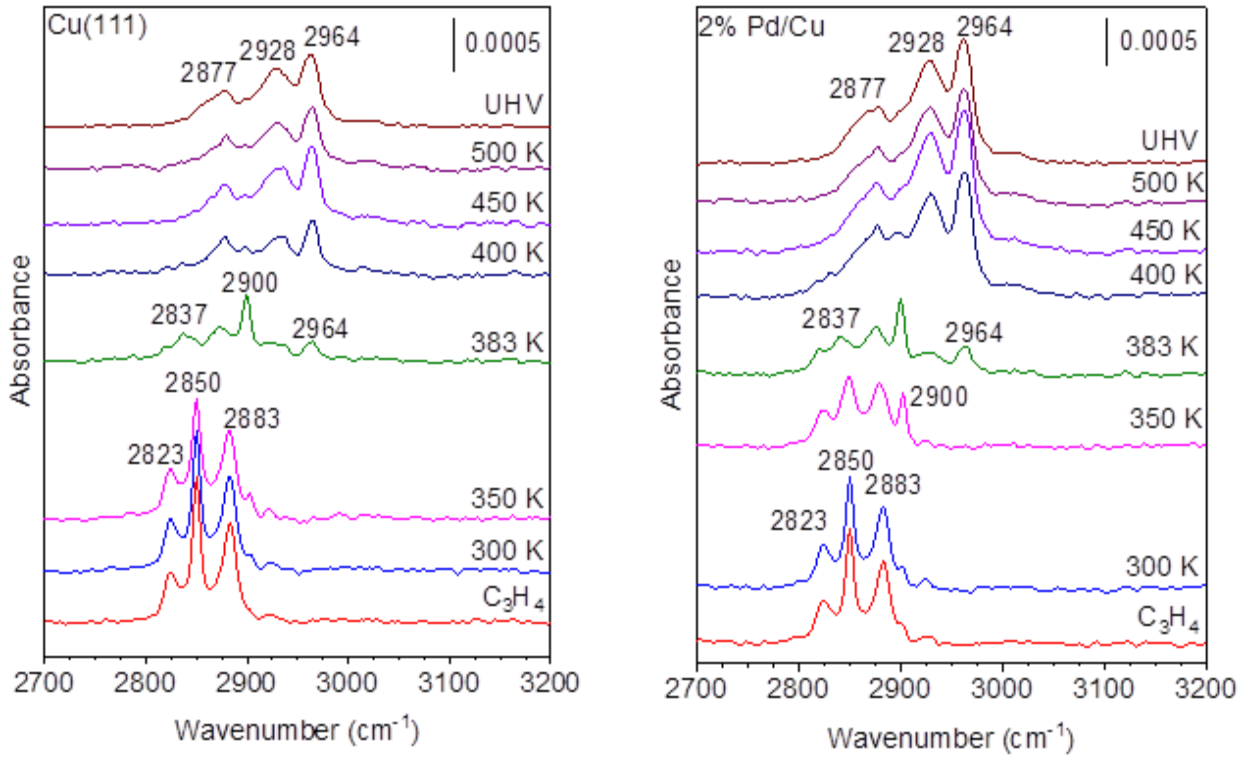

Figure 39 PD-RAIR spectra in the C-H stretch region of 50 mTorr of propyne (red) followed by 150 mTorr of H_2 (blue) exposed to Cu(111) (left) and 2% Pd/Cu(111) (right) at 300 K and after annealing at the indicated temperatures for one minute.

Annealing the surfaces to higher temperatures results in several changes in the spectra shown in Figures 38 and 39. On Cu(111), annealing to 350 K causes no discernible change in the spectra, whereas for the 2% Pd/Cu(111) surface there is a slight decrease in intensity of the peaks associated with adsorbed propyne and the appearance of a new species revealed most clearly by the rise of a peak at 2900 cm^{-1}. For a slightly higher annealing temperature of 383 K, an additional peak appears at 2964 cm^{-1}, and on both surfaces the 2900 cm^{-1} peak is most intense.

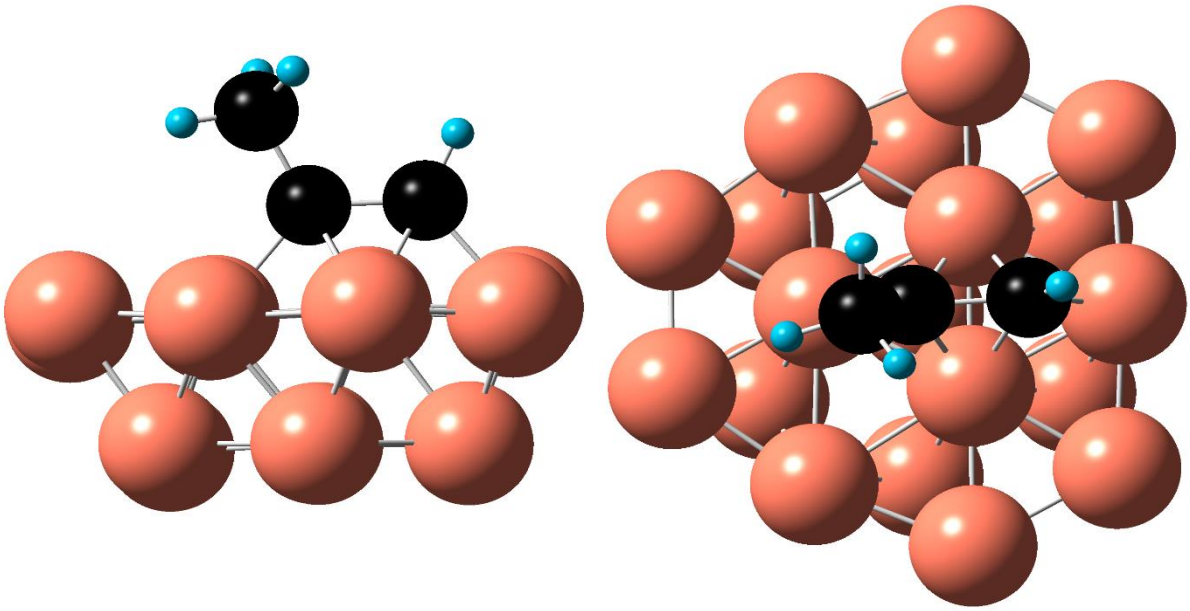

Figure 40 Side (left) and top (right) views of di-σ/di-π bound propyne to Cu(111)

Annealing to 400, 450, and 500 K produces essentially the same spectra on both surfaces, with peaks at 2877, 2928, and 2964 cm^{-1} in the C-H stretch region. In the lower wavenumber region, annealing to 400, 450, and 500 K produces peaks at 1380 and 1457-1460 cm^{-1}. The 383 K anneal produces peaks that are a mix of those due to adsorbed propyne and the higher temperature species. The stability of the species produced by annealing to 400 K and above is further indicated by the absence of any change upon evacuating the IR cell to UHV. We therefore conclude that propyne coupling reactions have occurred to produce a carbonaceous layer on the surface. Although the spectra for the Cu(111) and Pd/Cu(111) surfaces are similar, the intensities of the peaks for the Pd/Cu(111) surface are higher, indicating that the presence of Pd facilitates the formation of the carbonaceous layer from propyne.

We can compare our ambient pressure results with the known surface chemistry of propyne on Cu(111). Middleton and Lambert (135) used temperature programmed reaction (TPR) under UHV conditions to show that most propyne desorbs without reaction at 265 K, but that some coupling reactions occur leading to the desorption of benzene, butadiene, and a species at mass 82, which they conclude is most likely a non-cyclic diene, such as 1,4-hexadiene. In contrast to acetylene, which trimerizes on Cu(111) to form benzene, no evidence for propyne trimerization, which would yield a trimethyl benzene, was found. All species detected with TPR desorb by 400 K. They also conclude that approximately 5% of the adsorbed propyne decomposes to produce surface carbon and hydrogen, with the latter leading to the hydrogenation of propyne to propene (135). These TPR results imply that if RAIRS had been used to study propyne adsorbed on Cu(111) at low temperature in UHV and then annealed to 400 K or above, a featureless spectrum would have been obtained. Our results therefore reveal that additional reaction pathways are available under ambient pressure conditions that yield a stable carbonaceous surface layer. Nevertheless, the mechanism by which propyne couples on Cu(111) under UHV may be relevant to the initial stages of the reactions that we detect.

Middleton and Lambert (135) proposed that the main desorption products were produced from the coupling of two propyne molecules. They propose that benzene would form by H_2 elimination from a cyclohexadiene intermediate. In contrast, addition of two H atoms to a C_6H_8Cu dimethyl-metallopentacycle would lead to 1,4-hexadiene. In a subsequent DFT study of the propyne coupling mechanism on Cu(111), Clotet et al. (130) found that propyne isomerization to vinylcarbene, CH_2CHCH, would precede dimerization to form benzene. Martorell and Clotet (133) used DFT calculations to explore in detail the possible structures of adsorbed vinylcarbene for different unit cell sizes as a way to account for coverage effects. Furthermore, they simulated

IR spectra for vinylcarbene on Cu(111), which can be compared with our experimental spectra. The calculated RAIR spectrum for vinylcarbene on Cu(111) predicts many peaks, whereas our spectra show only a single peak at 2900 cm^{-1} that cannot be assigned to either adsorbed propyne, or to the highly stable carbonaceous layer. Therefore, there is insufficient evidence to assign the 2900 cm^{-1} peak to vinylcarbene.

The peaks that we observe with RAIRS for the carbonaceous deposit on our single crystal surfaces are remarkably similar to the IR spectra reported for propyne oligomers that form on high-area Cu catalysts. Bridier et al. (56) reported diffuse reflectance IR during propyne hydrogenation at 473 K over a Cu-hydrotalcite catalyst. The dominant peaks in their spectra were at 2960, 2925, 2870, 1445, and 1355 cm^{-1}, and showed similar intensity ratios as our peaks at 2964, 2928, 2877, 1460 and 1380 cm^{-1}. There is an even better match between our spectra and the IR spectra of Ossipoff and Cant (55) for oligomers formed from propyne over a Cu/SiO_2 catalyst. Following the assignments of Bridier et al., the peaks in Figure 31 at 2877, 2928, and 2960 cm^{-1} are due to the symmetric C-H stretch of a CH_3 group, and asymmetric C-H stretches of CH_2 and CH_3 groups, respectively. These comparisons indicate that essentially the same oligomer forms from propyne over Cu surfaces, regardless of the structure of the catalyst.

The comparison with the UHV results on Cu(111) indicates that in an ambient pressure of propyne, buildup of the oligomer on the surface occurs through reaction channels that are too minor to be detected in UHV experiments Identification of the products formed from the thermal decomposition of the carbonaceous layer is important for understanding the overall chemistry of propyne hydrogenation. Thermal desorption spectra are presented in Figure 41 after the surfaces had been annealed to 500 K in an ambient of 50 mTorr of propyne and 150 mTorr of H_2 and then transferred from the evacuated IR cell to the analysis chamber. There is no evidence of desorption

below 525 K at which temperature Pd diffuses into the subsurface of the Cu(111) crystal. The masses of interest are H_2 (m/z = 2), C_3H_4 (m/z = 40), C_3H_6 (m/z = 41), C_3H_8 (m/z = 29), and C_5H_7 (m/z = 67). The C_5H_7 could be from C_6 dienes (C_6H_{10}, m/z = 82), which lose a methyl group during ionization. From the Cu(111) surface, there is a main desorption peak at 650 K for the selected masses. The largest desorption is H_2 from the decomposition of the carbonaceous layer. This peak is accompanied by a C_2H_3 fragment (m/z = 27), which can be a fragment of propyne, propene, or any of the possible oligomers, and a CH_3 fragment (m/z = 15). Interestingly, propyne is not detected from the Cu surface indicating that all the adsorbed propyne reacted to form polymers, hydrogenation products, or surface carbon. The major hydrogenated C_3H_x species is propene since the intensity of its desorption is greater than that of propane. Small amounts of coupling products were detected; however, there was no indication of benzene (m/z = 78) from Cu(111) or from Pd/Cu. According to the earlier TPD study of propyne on Cu(111), propyne coupling to form benzene and C_6 dienes is favored at low initial propyne coverages, whereas at higher propyne coverages no desorption of benzene or C_6 dienes was observed (135). As our conditions correspond to their high propyne coverages, we would not expect to observe any benzene desorption.

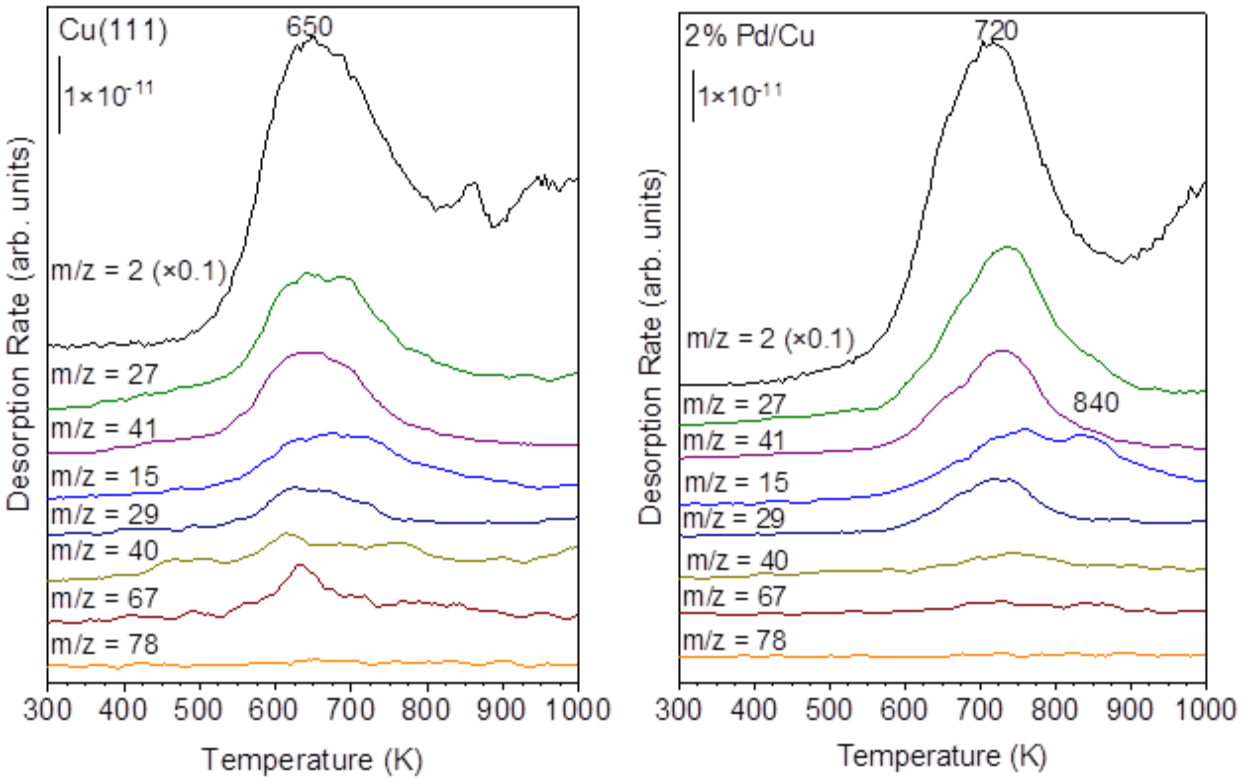

Figure 41 Thermal desorption spectra after annealing the surface to 500 K in an ambient of 50 mTorr of propyne and 150 mTorr of H_2 for Cu(111) (left) and 2% Pd/Cu(111) (right). The notable differences between the spectra is the absence of a peak at m/z = 67 and the presence of a shoulder at m/z = 15 from the alloy surface.

From the Pd/Cu SAA surface, there are no desorption peaks below 500 K. In a study characterizing PdCu surface alloys, Pd was found to diffuse into subsurface layers of Cu(111) between 490-570 K (136). There are small differences in the decomposition of the carbonaceous layer over Pd/Cu(111) and Cu(111). The m/z = 67 peak observed for Cu(111) is absent for Pd/Cu(111), and there is a distinct methyl peak at 840 K for Pd/Cu(111) that is not apparent for Cu(111). The second peak for the methyl group overlaps with a small shoulder on the peak for C_2H_3 fragments. Given that no propyne or propene features are detected at 840 K, it is plausible that the CH_3 fragment comes from the dissociation of C_2H_3 in the ion source of the mass

spectrometer. If this is the case, then this C_2H_3 peak would be identified as CCH_3 which arises from propyne or some other species with either a fully substituted carbon atom or an unsaturated carbon atom.

The deposition of the carbonaceous layer was also studied with AES. Whereas AES is sensitive to the amount of carbon present, RAIRS intensities of the CH_3 peaks will depend on the hydrogen content of the carbonaceous layer. For Cu(111), the surface composition becomes 71% C and 29% Cu after annealing the catalyst at 500 K under reaction conditions. After heating to 1000 K, the surface composition changes to 56% C and 44% Cu. This demonstrates that a stable carbon-containing deposit is formed from decomposition of the carbonaceous layer. Similar results are obtained on the SAA surface as evidenced by a composition of 68% C, 0.9% Pd, and 31.1% Cu after annealing at 500 K. After heating to 1000 K, the amount of C detected by AES decreases to 62%. Although the amount of carbon detected by AES on the Cu(111) and Pd/Cu(111) surfaces are similar, the more intense C-H stretches of the carbonaceous deposit seen in Figure 39 for Pd/Cu(111) suggests that the latter deposit has a higher H:C ratio.

6.3.2 Propene interaction with Cu(111) and Pd/Cu(111)

Since gas phase propene is detected as a hydrogenation product, it is important to characterize the surfaces in the presence of gas phase propene. Figures 42 and 43 show PD-RAIR spectra of the Cu(111) and 2% Pd/Cu(111) surfaces in the presence of 50 mTorr of propene and 150 mTorr of H_2. These results differ significantly from those reported previously for propene adsorbed at low temperatures under UHV conditions on Ag(111) (137) and Cu(111) (138,139). When propene adsorbs onto the Cu surface, Street and Gellman (139) found that the CH_2 wagging mode at 912 cm^{-1} dominates the spectrum for monolayer coverage. In contrast, we find that under a static total (propene + H_2) pressure of 200 mTorr, propene adsorbs at room temperature and the

RAIR spectra do not exhibit propene-specific features such as the CH_2 wagging mode at 912 cm^{-1}. At room temperature, adsorbed propene exhibits the same RAIR spectrum as adsorbed propyne. Since it was established above that propyne adsorbs in a di-σ/di-π fashion on Cu(111), we conclude that propene undergoes a dehydrogenation reaction to produce the same surface species as propyne. A peak at 1360 cm^{-1} is detected at room temperature, which is assigned to the coupling of the symmetric methyl deformation and the C_1C_2 stretching mode. This feature is evidence for di-σ/di-π bonded propyne as opposed to π-bonded propene. As the Cu(111) surface is heated to 400 K and above, the peaks seen at 1380 and 1457 cm^{-1} in Figure 38 and attributed to the carbonaceous layer are visible in Figure 42 but are much weaker. This is consistent with the weakness of the corresponding peaks in the C-H stretch region in Figure 43. For the Pd-Cu(111) surface, the only evidence for carbonaceous species from propene are very weak C-H stretches. Thus, although both propyne and propene give similar spectra at 300 K, there is much less carbonaceous material formed from propene, particularly on the Pd-Cu(111) SAA surface. This is consistent with past UHV studies on Cu(111) that show propyne coupling and decomposition (135), whereas propene desorbs molecularly at 120-140 K (138–140). However, in an ambient of 0.1 Pa of propene, slow carbon deposition occurs at temperatures of 475 K and above (141).

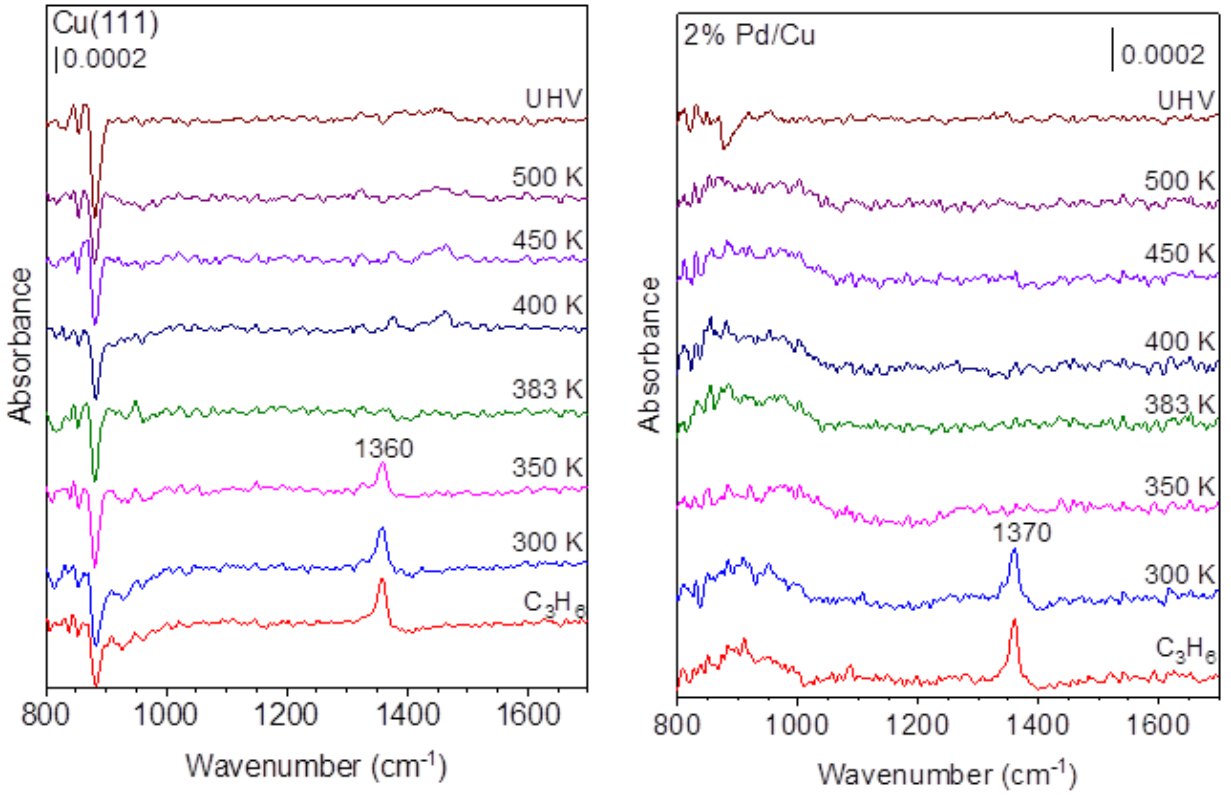

Figure 42 PD-RAIR spectra of 50 mTorr propene (red) followed by 150 mTorr H_2 (blue) exposed to Cu(111) (left) and 2% Pd/Cu(111) (right) at 300 K and after annealing at the indicated temperatures for one minute.

A peak at 2900-2902 cm^{-1} is seen in Figures 39 and 43 for both propyne and propene on both Cu(111) and Pd-Cu(111), but its intensity and behavior with temperature are different in each case. For propene on the Pd-Cu(111) surface, the 2902 cm^{-1} peak in Figure 43 appears in the 300 K spectrum but disappears upon heating to 350 K, whereas for Cu(111), the peak at 2900 cm^{-1} is most intense after heating to 383 K. In Figure 39, the 2900 cm^{-1} peak is most intense for the 383 K spectrum for both Cu(111) and Pd-Cu(111). Although the appearance of this peak precedes the formation of the carbonaceous layer, it does not seem to be an intermediate in that reaction as its intensity does not correlate with the intensity of the peaks seen after the 500 K anneal. As the

presence of Pd seems to favor both the formation and reaction of the intermediate, a reasonable hypothesis is that it forms from the dehydrogenation of propene and from the hydrogenation of propyne. We therefore speculate that the 2900 cm^{-1} peak is due to a *CH=CH-CH_3 surface species. Other possibilities are propylidyne CH_3H_2CC, which when formed from propene on Pd(111), features a C-H stretch at 2924 cm^{-1} as by far the most intense peak in the RAIR spectrum (142). However, there is no evidence in the literature of propylidyne formation on Cu(111).

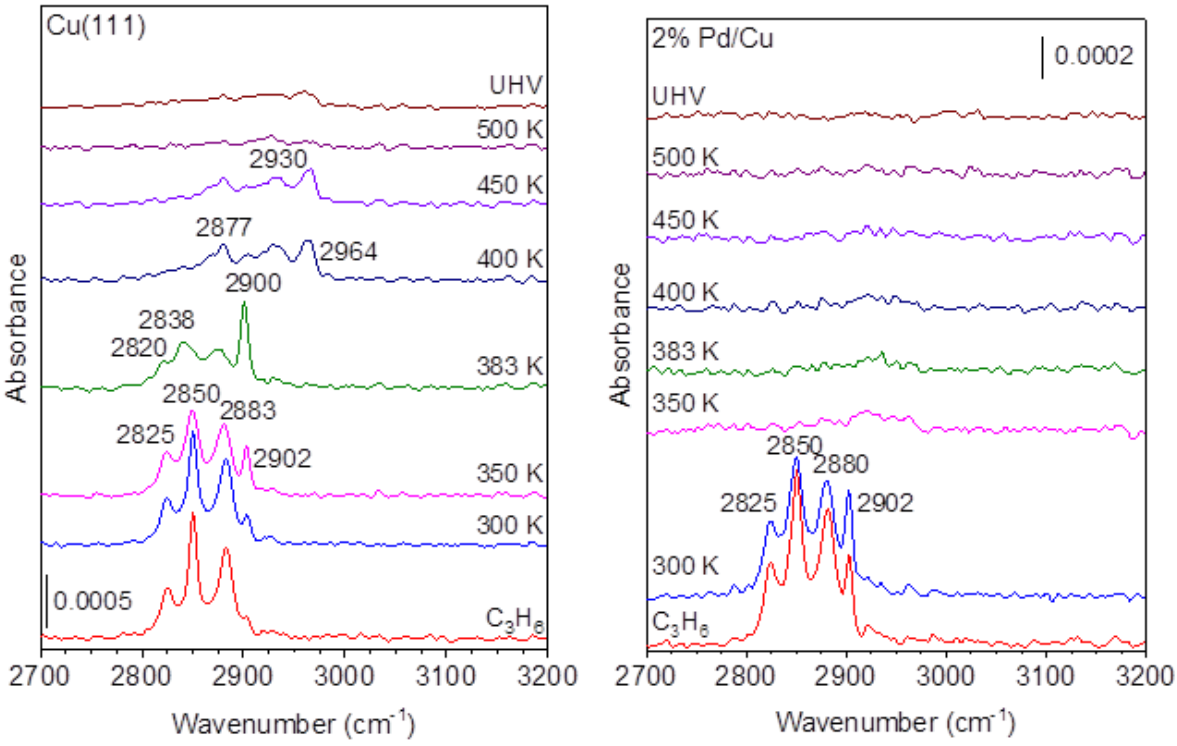

Figure 43 PD-RAIR spectra in the C-H stretch region of 50 mTorr propene (red) followed by 150 mTorr H_2 (blue) exposed to Cu(111) (left) and 2% Pd/Cu(111) (right) at 300 K and after annealing at the indicated temperatures for one minute.

Figure 44 shows TPD spectra of the carbonaceous layer after the surface had been annealed to 500 K for 1 min in an ambient of 50 mTorr of propene and 150 mTorr of H_2. Consistent with the RAIRS results in Figures 39 and 43, there is less carbonaceous deposit from propene than from propyne, and hence weaker desorption peaks in Figure 44 than in Figure 41. From the Cu surface, the major desorption peaks are H_2 and C_3H_6 at 800 K and C_2H_4 and CH_4 at 690 K. From the SAA surface, the major desorption peaks are H_2 at 670 K, propene at 580 and 820 K, and propyne at 615 K. The presence of a propyne desorption peak indicates that some dehydrogenation of propene occurred on the SAA surface. No propane (m/z = 29) or coupling products (m/z = 67) were detected by TPD from the SAA surface. After the Cu surface was annealed to 500 K, the surface composition from AES was 50% carbon and 50% Cu. After heating to 1000 K, the carbon layer becomes slightly denser as H_2 is evolved; thus, the AES results indicate a surface composition of 51% carbon and 49% Cu. Interestingly, the SAA surface composition is 14% carbon, 1.6% Pd, and 84.4% Cu after annealing to 500 K. After heating to 1000 K, the Pd diffuses into the bulk of the crystal and the surface composition is 11% carbon and 89% Cu. The lower amount of carbon on the SAA surface indicates that the presence of Pd promotes either propene desorption or hydrogenation to propane, although the latter was not detected by gas phase IR. In either case, the results indicate that the presence of Pd suppresses formation of the carbonaceous layer. This is indicated both by the lower amount of carbon detected with AES and by the much weaker C-H stretches seen in the RAIR spectra in Figure 43 after annealing to 500 K.

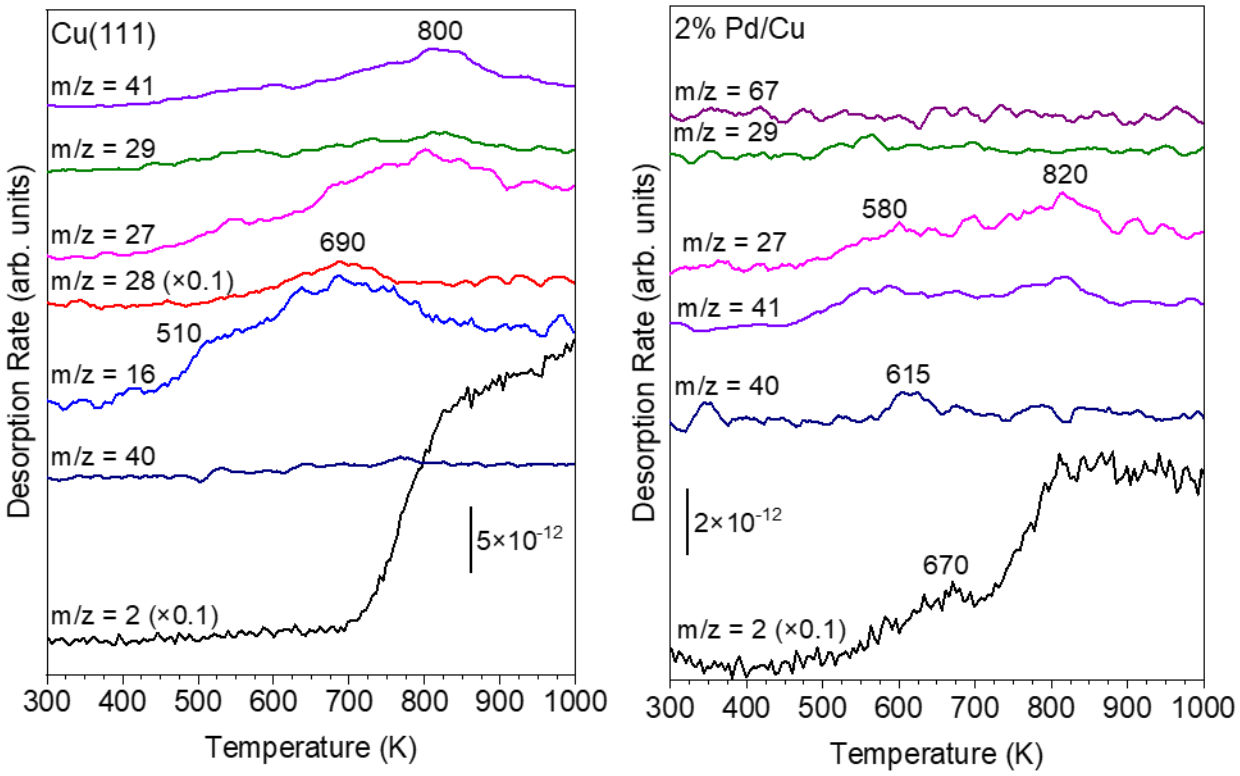

Figure 44 Thermal desorption spectra from Cu(111) (left) and 2% Pd/Cu(111) (right) after annealing to 500 K for 1 min in an ambient of 50 mTorr of propene and 150 mTorr of H_2.

6.3.3 Reaction kinetics of propyne hydrogenation over a 2% Pd/Cu(111) single atom alloy catalyst

In the previous sections, it was confirmed that propyne adsorbs to both the Cu and SAA surfaces. To determine if propene was produced as the hydrogenation product, the gas phase RAIR spectra must be considered. Under the reaction conditions in section 6.3.1, no gas phase propene was detected when annealed for 1 minute at temperatures ranging from 350 to 500 K. The experiment was repeated with a reactant pressure higher by a factor of 10 and the resulting gas phase RAIR spectra are presented in Figure 45. At the higher pressure, the P and R branches of the C_2—C_3 stretch of gas phase propyne are resolved at 920 and 940 cm^{-1}, respectively.

The reaction over the Cu surface does not yield any propene features when annealed up to 450 K for one minute. However, over the SAA surface, broadening of the 920 cm^{-1} peak begins at 383 K, and the CH_2 wagging mode of gas phase propene at 912 cm^{-1} can be seen at 400 K. At 450 K, the propene allylic CH bend at 991 cm^{-1} becomes prominent. The spectra in Figure 46 show the gas phase RAIR spectra for a mixture of 500 mTorr propyne and 1500 mTorr H_2 taken at 383 K at 4 hour intervals. The time dependence of the gas-phase propyne and propene IR peaks at 3323 and 912 cm^{-1}, respectively, were used to determine the kinetics of the hydrogenation reaction. From measurements of the kinetics and the temperature dependence of the rate constants, the activation energy, reaction order, and turnover frequency were determined. In addition to showing the spectral region for the propene peak at 912 cm^{-1} and the propyne ≡C–H peak at 3323 cm^{-1}, the CH_3 stretch region, containing peaks from both molecules, is also shown. In the CH_3 stretch region, the propyne peaks show resolvable rotational fine structure, whereas the propene peaks do not. In principle, this could be used as basis for monitoring the reaction in this spectral region alone, despite the overlap of the peaks. For this reaction, however, the molecules are best distinguished by the other two spectral regions. The ≡C–H stretching peak for propyne decreased until it was no longer detectable. It can be concluded from this that the SAA catalyst is robust, with its catalytic activity lasting for at least 12 hours. If the catalyst lost activity, gas phase propyne would have still been present after 12 hours. The same reaction was conducted over the Cu catalyst for 12 hours as a control experiment.

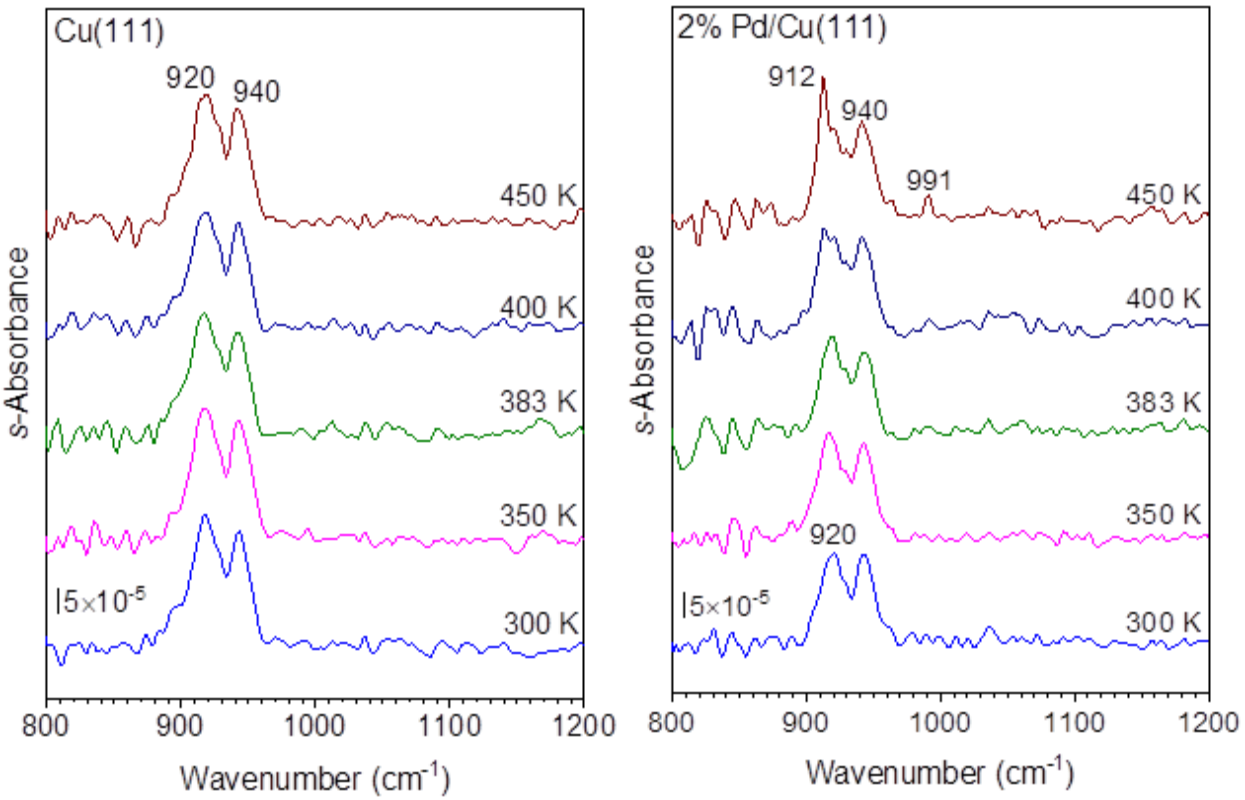

Figure 45 Gas phase RAIR spectra of 500 mTorr of propyne and 1500 mTorr of H_2 over Cu(111) (left) and 2% Pd/Cu(111) (right) at 300 K and after annealing at the indicated temperatures for one minute.

From the RAIR spectra, the conversion and selectivity of the reaction was calculated as follows:

$$\%\ conversion = \frac{\mu mol\ C_3H_4\ consumed}{\mu mol\ C_3H_4 introduced} \times 100 \qquad \text{Equation 6.1}$$

$$\%\ selectivity = \frac{\mu mol\ C_3H_6\ produced}{\mu mol\ C_3H_4\ consumed} \times 100 \qquad \text{Equation 6.2}$$

Over the Cu catalyst, there was a 4.8% conversion of propyne after 12 hours, which led to a 28% selectivity to propene; whereas, there was a 100% conversion over the SAA catalyst with a 50% selectivity to propene. TPD and AES were used to determine the nature of the missing 50% of the

propyne. From the TPD spectra in Figure 47, there are many carbon containing species that desorb from the SAA surface at 640 K with ethylene being the most intense carbon-containing peak followed by propene. The peaks at 67, 78, and 82 are indicative of carbon-carbon coupling reactions; however, they appear with a low intensity indicating that the carbonaceous layer is more likely to decompose to smaller hydrocarbons than desorb as larger hydrocarbons.

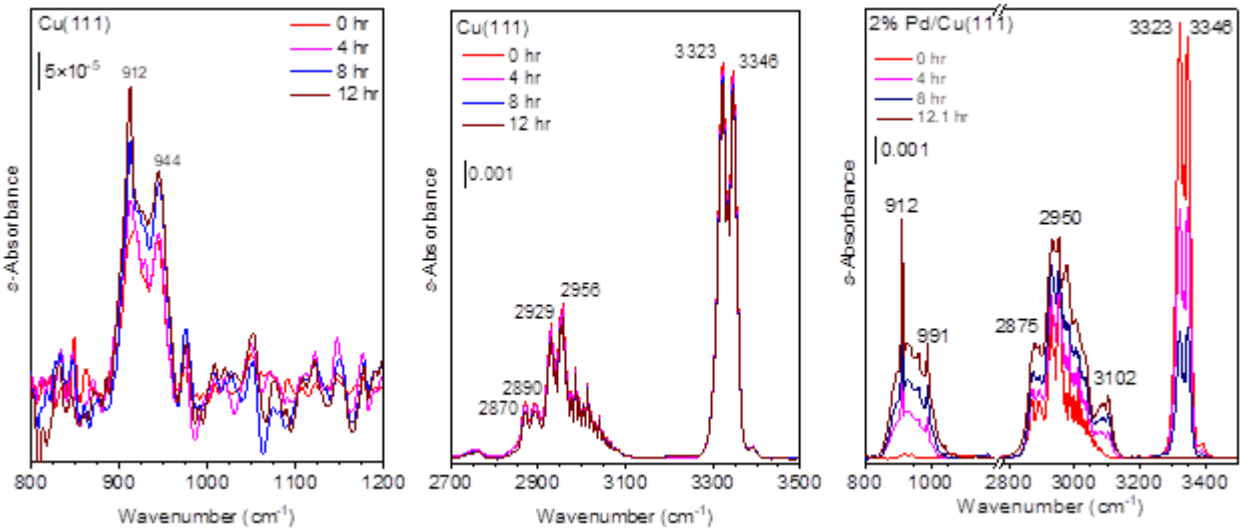

Figure 46 IR spectra for 500 mTorr of propyne and 1500 mTorr of H_2 at 383 K over Cu(111) (left and middle) and 2% Pd/Cu(111) (right) taken at four-hour intervals.

On the Cu surface, the desorption peaks are the same as the SAA surface; however, the peaks are shifted to higher temperatures. The Auger spectra of both surfaces after the reaction contains only the C KVV peak indicating that the reaction proceeds even in the presence of a thick carbon layer. This implies that while the carbonaceous layer is thicker than the mean-free path of

the Auger electrons (hence only carbon is seen with AES), the layer is still quite porous for diffusion of reactants and products to and from the metal surface. After the Auger spectra were collected, the carbon layer became visible as a black spot on the crystal due to interaction with the electron beam.

Table VII Propyne hydrogenation at 383 K over 2% Pd/Cu under different reactant amounts.

C_3H_4 (μmol)	32	3.2	3.2
H_2 (μmol)	96	9.6	96
H_2:C_3H_4	3:1	3:1	30:1
Time (min)	720	400	40
Selectivity	50 %	50 %	68%

To determine the rate order with respect to propyne and H_2, as well as the selectivity to propene, the reaction was studied at three different pressures as presented in Table VII. With a 30:1 ratio of H_2:C_3H_4, the reaction was more selective (68%) to propene at 383 K. McCue et al. (60) were able to achieve 70% selectivity to propene at 383 K with a 3:1 H_2:propyne ratio, which was reproduced in this study with a 30:1 ratio. The reaction may be driven by the ratio of adsorbed H atoms to adsorbed propyne. With a greater H_2 pressure, the dissociation of H_2 to H_{ads} is favored. Tierney et al. (65) have shown that H atoms are most stable in the fcc site shared by one Pd atom and two Cu atoms on Pd/Cu(111) SAAs. To determine if H_{ads} is present in concentrated areas near the Pd sites or distributed across the entire surface, imaging techniques such as ambient pressure atomic force microscopy (AFM) or scanning tunneling microscopy (STM) under reaction

conditions would best provide an explanation for the enhanced selectivity with large excesses of H_2. Given the reversibility of H_2 dissociation at reaction temperatures, H_2 desorption must be considered as a competing reaction in the hydrogenation of alkynes. To maintain a large quantity of H_{ads} available for hydrogenation, H_2 should be used in large excess >30:1 to enhance the selectivity of the reaction over single crystal catalysts.

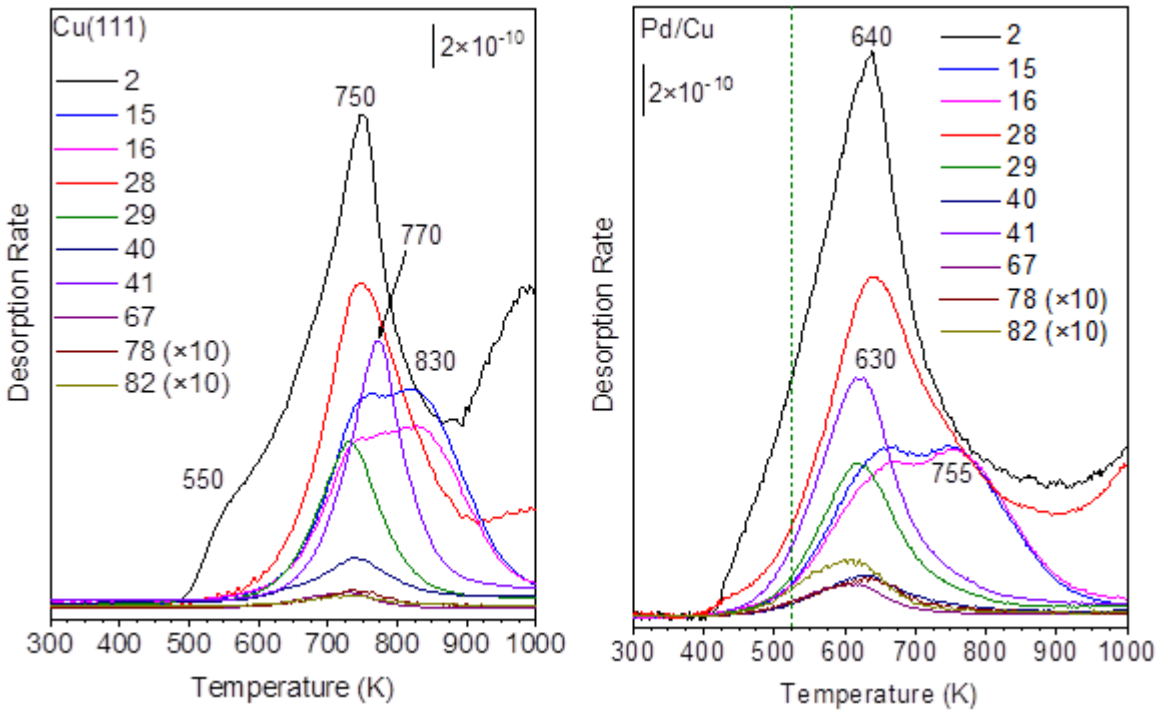

Figure 47 TPD spectra of the carbonaceous layer formed after the propyne hydrogenation reaction is completed. The green dotted line indicates the temperature at which Pd diffuses into the Cu(111) crystal.

By comparing the reaction rates at each condition, the reaction orders were determined to be -0.36 with respect to propyne and 1.05 with respect to H_2. The propyne rate order agrees with that reported by Mann and Khulbe (62) for a Pd powder catalyst (-0.24±0.13), and the H_2 rate order falls between the values reported by Mann and Khulbe (63) for Cu powder (0.97±0.04) and Pd powder (1.25±0.05) catalysts. The slightly negative reaction order with respect to propyne is ascribed to the formation of an ordered structure on the surface that limits the diffusion of gases to and from the surface.

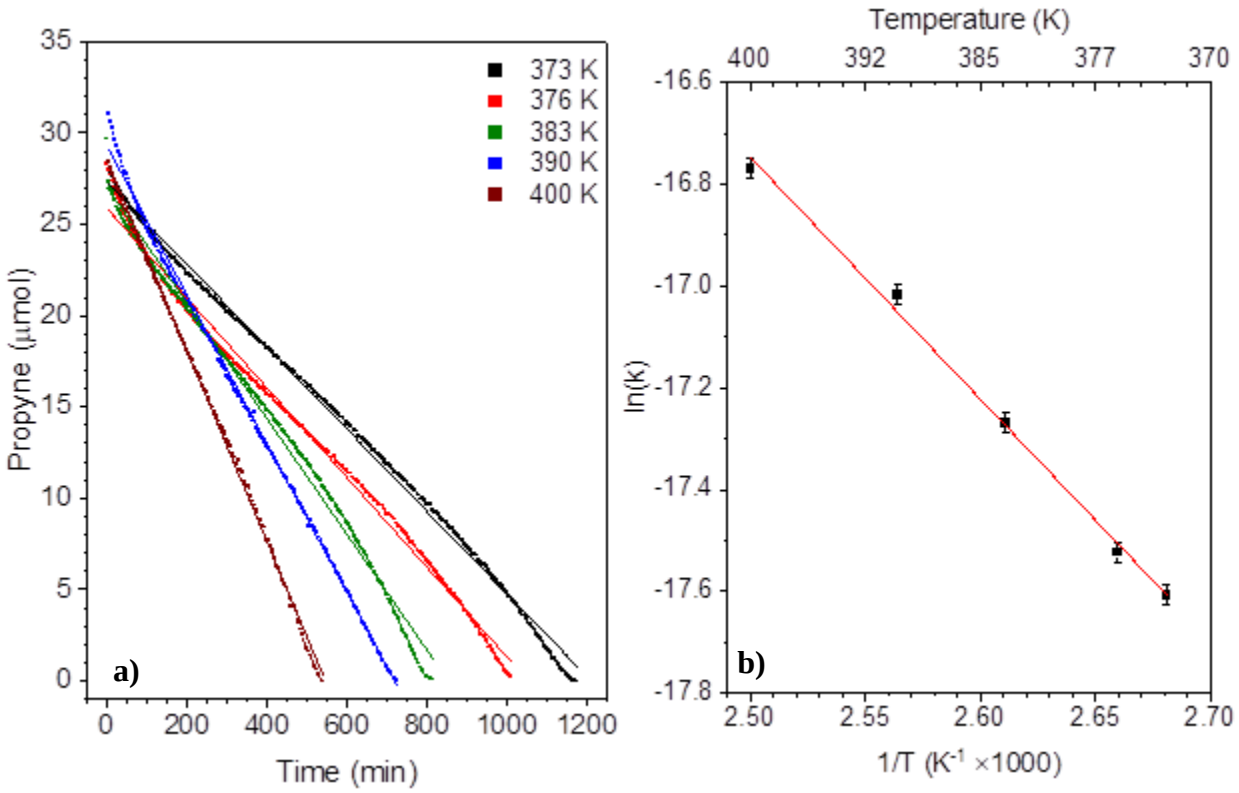

Figure 48 Amount of propyne versus time at three different temperatures and linear fits to the data (a). The rates constants from (a) were used to determine the activation energy from the Arrhenius plot in (b).

Plots of the propyne amount versus time are presented in Figure 48a along with linear fits to the data. At each temperature, the amount of propyne falls approximately linearly with time after 60 minutes. Propene is produced more rapidly in the first 60 minutes of the reaction until a steady state is achieved. A turnover frequency (TOF) for propene production was determined for the reaction over the 2% Pd/Cu(111) catalyst at each temperature by the equation $TOF = \frac{amt\ propene\ produced}{amt\ Pd\ sites \times reaction\ time}$. The TOF calculated in this work (25.4 s^{-1} at 383 K) is significantly greater than the value estimated by McCue et al (60). (0.050 s^{-1} at 383 K). McCue et al. (60) based their TOF on the number of Cu sites claiming that the reaction is catalyzed by Cu. Since little propene is produced with the Pd-free Cu(111), Pd is considered to be the active site here, which accounts for the higher TOF.

Figure 48b shows an Arrhenius plot of the rate constants versus temperature. The slope yields an activation energy for the hydrogenation of propyne over a 2% Pd/Cu(111) catalyst of 39.4±0.9 kJ/mol. This is within the experimental error of that of a pure Pd catalyst as determined by Mann and Khulbe, who reported activation energies of 21.2 kcal/mol (88.7 kJ/mol) and 9.5 kcal/mol (39.7 kJ/mol) for unsupported Cu (63) and Pd (62) catalysts, respectively. A comparison of the activation energies determined in this work and for pure Cu and pure Pd catalysts is given in Table VIII. The fact that the reaction over the SAA catalyst behaves like the reaction over a pure Pd catalyst is consistent with the Pd atoms being the active site in the SAA catalyst.

Table VIII A comparison of the kinetic constants from the SAA catalyst to the pure catalysts.

Catalyst	Cu[a]	Pd[b]	2% Pd/Cu[c]
E_A (kJ/mol)	88.7±0.8	39.7±0.8	39.4±0.9
C_3H_4 order	0.49±0.02	-0.24±0.13	-0.36
H_2 order	0.97±0.04	1.25±0.05	1.05

[a]Ref. (62), [b]Ref.(63), [c]This work

6.4. Conclusions

By monitoring the gas-phase IR spectra of propyne and propene, it was found that a 2% Pd-Cu(111) single-atom alloy has a much higher hydrogenation activity than a Cu(111) surface under ambient pressure conditions. Alkyne coupling occurs on both surfaces to form a carbonaceous layer. However, the presence of this carbonaceous layer does not inhibit the hydrogenation activity. Over the 2% Pd-Cu(111) surface at 383 K and above, propene is produced with a 50% selectivity (68% in a large H_2 excess). Moreover, when compared to results in the literature for pure Cu and pure Pd catalysts, the reaction over the SAA exhibits kinetic properties comparable to those of Pd as evidenced by an activation energy of 39.4±0.9 kJ/mol and a rate order of -0.36 with respect to propyne and 1.05 with respect to H_2. Based on these findings, we conclude that the Pd atoms are the active sites of the SAA catalyst. The turnover frequency at the Pd sites is 25.4 s^{-1} at 383 K. We conclude that the SAA catalyst successfully combines the activity of Pd with the selectivity of Cu for the selective hydrogenation of propyne to propene.

Chapter 7 – Conclusions and Future Outlook

The analysis of chemical reactions occurring on catalyst surfaces is vital for understanding the elementary steps of industrially important reactions. Surface science techniques allow researchers to study the key steps and intermediates of these reactions. The major drawback of surface science techniques is that they require ultra-high vacuum and low temperature conditions which are not used in industrial processes. Ambient pressure techniques were developed to overcome this barrier. The presented work demonstrates the versatility of infrared spectroscopy as a surface analysis tool across a wide range of temperatures and pressures. Important reactions, such as selective hydrogenation or oxidative desulfurization, studied under ambient pressures provide insight to the reaction dynamics that would not be observed under UHV conditions. For example, in Chapter 6, it was demonstrated that propyne adsorbs to Cu(111) under ambient pressures at room temperature. Moreover, propyne adsorbs to Cu with the same geometry under ambient pressure as it does under UHV conditions at low temperatures. By understanding how molecules adsorb on catalyst surfaces, reaction pathways can be predicted. These types of studies are usually done under UHV; however, with ambient pressure techniques, the reaction pathways can be inferred under the conditions used in industrial processes.

Cited Literature

1. Abdel-Rahman M, Feng X, Muir M, Ghale K, Xu Y, Trenary M. Reaction pathways for HCN on transition metal surfaces. Phys Chem Chem Phys. 2019;21(9):5274–84.
2. Feng X, Abdel-Rahman MK, Kruppe CM, Trenary M. Deposition and characterization of stoichiometric films of V2O5 on Pd(111). Surf Sci. 2017;664:1–7.
3. Abdel-Rahman MK, Trenary M. Propyne hydrogenation over a Pd/Cu(111) single-atom alloy studied using ambient pressure infrared spectroscopy. ACS Catal. 2020;(111):9716–24.
4. Kordesch ME, Lindner T, Somers J, Stenzel W, Conrad H, Bradshaw AM, et al. The surface chemistry of the CN group: geometry and bonding. Spectrochim Acta - Part A Mol Spectrosc. 1987;43(12):1561–6.
5. Kordesch ME, Stenzel W, Conrad H. A comparison of single-, double-, triple-bonded and aromatic CN compounds on Pd(111) and (100). II. HREELS and TDS of HCN on Pd(111). Surf Sci. 1988;205:100–16.
6. Jentz D, Celio H, Mills P, Trenary M. Formation of aminomethylidyne from hydrogen cyanide on Pt(111). Surf Sci. 1995;341:1–8.
7. Jentz D, Mills P, Celio H, Belyansky M, Trenary M. Formation of hydrogen bonded aggregates of aminomethylidyne on Pt(111). J Chem Phys. 1996;105:3250–7.
8. Jentz D, Mills P, Celio H, Trenary M. The surface chemistry of CN and H on Pt(111). Surf Sci. 1996;368(1–3):354–60.
9. Celio H, Mills P, Jentz D, Pae YI, Trenary M. Molecular adsorption of HCN on Pt(111) and Cu(100). Langmuir. 1998;14:1379–83.
10. Hu X, Trenary M. Kinetics of HCN decomposition on the Pt(111) surface by time-dependent infrared spectroscopy. J Phys Chem C. 2012;116:4091–6.
11. Hu X, Yin J, Meyer RJ, Trenary M. Kinetics of aminocarbyne formation on Pt(111). J Phys Chem C. 2015;119(26):14506–12.
12. Hyde GE, Hornig DF. The measurement of bond moments and derivatives in HCN and DCN from infrared intensities. J Chem Phys. 1952;20:647–52.
13. Nakagawa T, Morino Y. Anharmonic potential constants and vibrational and rotational parameters for hydrogen cyanide. Bull Chem Soc Jpn. 1969;42:2212–9.
14. Pacansky J, Calder GV. The infrared spectra of HCN isotopes in argon matrices. An examination of the assumptions of matrix isolation spectroscopy. J Mol Struct. 1972;14:363–83.
15. Bohn RB, Andrews L. Matrix infrared spectra of the NH_3--HCN and NH_3--$(HCN)_2$ complexes in solid argon. J Phys Chem. 1989;93:3974–9.

16. Chatterjee B, Kang DH, Herceg E, Trenary M. Comparison of experimental and calculated infrared spectra of aminocarbynes on the Pt(111) surface. J Chem Phys. 2003;119:10930–40.

17. Ford DC, Xu Y, Mavrikakis M. Atomic and molecular adsorption on Pt(111). Surf Sci. 2005;587:159–74.

18. Gómez-Díaz J, López N. Mechanistic switch between oxidative (andrussow) and nonoxidative (degussa) formation of HCN on Pt(111) by density functional theory. J Phys Chem C. 2011;115:5667–74.

19. Bol CWJ, Kovacs JD, Chen M, Friend CM. Control of reaction selectivity via surface oxygen coverage: Thermal decomposition of azomethane on Rh(111). J Phys Chem B. 1997;101:6436–42.

20. Kis A, Barthos R, Kiss J. Thermal and UV photo-induced decomposition of azomethane on Rh(111). Phys Chem Chem Phys. 2000;2:4237–41.

21. Bond GC, Vedrine JC. Vanadia catalysts for selective oxidation of hydrocarbons and their derivatives. Appl Catal A Gen. 1997;157:1–425.

22. Weckhuysen BM, Keller DE. Chemistry, spectroscopy and the role of supported vanadium oxides in heterogeneous catalysis. Catal Today. 2003;78:25–46.

23. Wachs IE. Catalysis science of supported vanadium oxide catalysts. Dalt Trans. 2013;42:11762–9.

24. Ramos-Luna MA, Cedeño-Caero L. Effect of sulfates and reduced-vanadium species on oxidative desulfurization (ODS) with V_2O_5/TiO_2 catalysts. Ind Eng Chem Res. 2011;50:2641–9.

25. Zhang XF, Wang KX, Wei X, Chen JS. Carbon-coated V_2O_5 nanocrystals as high performance cathode material for lithium ion batteries. Chem Mater. 2011;23:5290–2.

26. Levi E, Gofer Y, Aurbach D. On the way to rechargeable Mg batteries: The challenge of new cathode materials. Chem Mater. 2010;22:860–8.

27. Leisenberger FP, Surnev S, Vitali L, Ramsey MG, Netzer FP. Nature, growth, and stability of vanadium oxides on Pd(111). J Vac Sci Technol A Vacuum, Surfaces, Film. 1999;17:1743–9.

28. Surnev S, Vitali L, Ramsey M, Netzer F, Kresse G, Hafner J. Growth and structure of ultrathin vanadium oxide layers on Pd(111). Phys Rev B - Condens Matter Mater Phys. 2000;61(20):13945–54.

29. Surnev S, Kresse G, Sock M, Ramsey MG, Netzer FP. Surface structures of ultrathin vanadium oxide films on Pd(111). Surf Sci. 2001;495:91–106.

30. Wong GS, Vohs JM. An XPS study of the growth and electronic structure of vanadia films supported on CeO_2(111). Surf Sci. 2002;498:266–74.

31. Wong GS, Concepcion MR, Vohs JM. Reactivity of monolayer V_2O_5 films on TiO_2(110) produced via the oxidation of vapor-deposited vanadium. Surf Sci. 2003;526:211–8.

32. Agnoli S, Sambi M, Granozzi G, Castellarin-Cudia C, Surnev S, Ramsey MG, et al. The growth of ultrathin films of vanadium oxide on TiO_2(110). Surf Sci. 2004;562:150–6.

33. Kim CY, Bedzyk MJ. Study of growth and oxidation of vanadium films on α-Fe_2O_3(0001). Thin Solid Films. 2006;515:2015–20.

34. Guimond S, Göbke D, Romanyshyn Y, Sturm JM, Naschitzki M, Kuhlenbeck H, et al. Growth and characterization of ultrathin V_2O_y ($y \approx 5$) Films on Au(111). J Phys Chem C. 2008;112:12363–73.

35. Guimond S, Sturm JM, Göbke D, Romanyshyn Y, Naschitzki M, Kuhlenbeck H, et al. Well-ordered V_2O_5(001) thin films on Au(111): Growth and thermal stability. J Phys Chem C. 2008;112:11835–46.

36. Wang Q, Madix RJ. Preparation and reactions of V_2O_5 supported on TiO_2(110). Surf Sci. 2001;474:3–6.

37. Silversmit G, Poelman H, Depla D, Barrett N, Marin GB, De Gryse R. A fully oxidized V_2O_5/TiO_2(001)-anatase system studied with in situ synchrotron photoelectron spectroscopy. Surf Sci. 2005;584:179–86.

38. Julien C, Guesdon JP, Gorenstein A, Khelfa A, Ivanov I. The growth of V_2O_5 flash-evaporated films. J Mater Sci Lett. 1995;14:934–6.

39. Julien C, Guesdon JP, Gorenstein A, Khelfa A, Ivanov I. The influence of the substrate material on the growth of V_2O_5 flash-evaporated films. Appl Surf Sci. 1995;90:389–91.

40. Ramana C V., Utsunomiya S, Ewing RC, Becker U. Formation of V_2O_3 nanocrystals by thermal reduction of V_2O_5 thin films. Solid State Commun. 2006;137:645–9.

41. Wu QH, Thissen A, Jaegermann W, Liu M. Photoelectron spectroscopy study of oxygen vacancy on vanadium oxides surface. Appl Surf Sci. 2004;236:473–8.

42. Wu QH, Thißen A, Jaegermann W. XPS and UPS study of Na deposition on thin film V_2O_5. Appl Surf Sci. 2005;252:1801–5.

43. Wu QH, Thißen A, Jaegermann W. Photoelectron spectroscopic study of Li intercalation into V_2O_5 thin films. Surf Sci. 2005;578:203–12.

44. Houda S, Lancelot C, Blanchard P, Poinel L, Lamonier C. Oxidative desulfurization of heavy oils with high sulfur content: A review. Catalysts. 2018;8:344–70.

45. Wang J, Zhao D, Li K. Oxidative desulfurization of dibenzothiophene using ozone and hydrogen peroxide in ionic liquid. Energy Fuels. 2010;24:2527–9.

46. Te M, Fairbridge C, Ring Z. Oxidation reactivities of dibenzothiophenes in polyoxometalate/H_2O_2 and formic acid/H_2O_2 systems. Appl Catal A Gen. 2001;219:267–80.

47. Hulea V, Fajula F, Bousquet J. Mild oxidation with H_2O_2 over Ti-containing molecular sieves - A very efficient method for removing aromatic sulfur compounds from fuels. J Catal. 2001;198:179–86.

48. Collins FM, Lucy AR, Sharp C. Oxidative desulphurisation of oils via hydrogen peroxide and heteropolyanion catalysis. J Mol Catal A Chem. 1997;117:397–403.

49. Tomskii IS, Vishnetskaya M V., Vakhrushin PA, Tomskaya LA. Oxidative desulfurization of straight-run diesel fraction on vanadium–molybdenum catalysts. Pet Chem. 2017;57:908–13.

50. Cedeño-Caero L, Gomez-Bernal H, Fraustro-Cuevas A, Guerra-Gomez HD, Cuevas-Garcia R. Oxidative desulfurization of synthetic diesel using supported catalysts. Part III. Support effect on vanadium-based catalysts. Catal Today. 2008;133–135:244–54.

51. Luo Z, Cao Z, Su Y. Monte Carlo simulation of propylene polymerization (I) Effects of impurity on propylene polymerization. Chinese J Chem Eng. 2006;14:194–9.

52. García-Mota M, Bridier B, Pérez-Ramírez J, López N. Interplay between carbon monoxide, hydrides, and carbides in selective alkyne hydrogenation on palladium. J Catal. 2010;273:92–102.

53. Kennedy DR, Webb G, Jackson SD, Lennon D. Propyne hydrogenation over alumina-supported palladium and platinum catalysts. Appl Catal A Gen. 2004;259:109–20.

54. Jackson SD, Casey NJ. Hydrogenation of propyne over palladium catalysts. J Chem Soc Faraday Trans. 1995;91:3269–74.

55. Ossipoff NJ, Cant NW. The hydrogenation and oligomerisation of propyne over an ion-exchanged copper on silica catalyst. J Catal. 1994;148:125–33.

56. Bridier B, Hevia MAG, López N, Pérez-Ramírez J. Permanent alkene selectivity enhancement in copper-catalyzed propyne hydrogenation by temporary CO supply. J Catal. 2011 Feb 14;278:167–72.

57. Bridier B, López N, Pérez-Ramírez J. Partial hydrogenation of propyne over copper-based catalysts and comparison with nickel-based analogues. J Catal. 2010;269:80–92.

58. Darby MT, Stamatakis M, Michaelides A, Sykes ECH. Lonely atoms with special gifts: breaking linear scaling relationships in heterogeneous catalysis with single-atom alloys. J Phys Chem Lett. 2018;9:5636–46.

59. Kruppe CM, Krooswyk JD, Trenary M. Selective hydrogenation of acetylene to ethylene in the presence of a carbonaceous surface layer on a Pd/Cu(111) single-atom alloy. ACS Catal. 2017;7:8042–9.

60. McCue AJ, Gibson A, Anderson JA. Palladium assisted copper/alumina catalysts for the selective hydrogenation of propyne, propadiene and propene mixed feeds. Chem Eng J. 2016 Feb 1;285:384–91.

61. Mann RS, Khulbe KC. Hydrogenation of methylacetylene over platinum and iridium catalysts. J Phys Chem. 1969;73:2104–10.

62. Mann RS, Khulbe KC. Hydrogenation of methylacetylene. IV. The reaction of methylacetylene with hydrogen catalyzed by palladium, platinum, iridium, rhodium, and ruthenium catalysts. Can J Chem. 1969;47:215–21.

63. Mann RS, Khulbe KC. Hydrogenation of methylacetylene. III. The reaction of methylacetylene with hydrogen catalyzed by nickel, copper, and their alloys. Can J Chem. 1968;46:623–31.

64. Wehrli JT, Thomas DJ, Wainwright MS, Trimm DL, Cant NW. Selective hydrogenation of propyne over an ion-exchanged copper on silica catalyst. Appl Catal. 1990;66:199–208.

65. Tierney HL, Baber AE, Kitchin JR, Sykes ECH. Hydrogen Dissociation and Spillover on Individual Isolated Palladium Atoms. Phys Rev Lett. 2009;103:1–4.

66. Fan J, Trenary M. Symmetry and the Surface Infrared Selection Rule for the determination of the Structure of Molecules on Metal Surfaces. Langmuir. 1994;10:3649–57.

67. Michelson AA, Morley EW. On the relative motion of the earth and luminiferous ether. Am. J. Sci. 1887. p. 332–45.

68. Moulder JF, Stickle WF, Sobol PE, Bomben KD. Handbook of X-ray Photoelectron Spectroscopy. Chastain J, editor. Perkin-Elmer Corporation; 1992.

69. Marchon B, Carrazza J, Heinemann H, Samorjai GA. TPD and XPS studies of O2, CO2, and H2O adsorption on clean polycrystalline graphite. Carbon N Y. 1988;26:507–14.

70. Ratner BD, Castner DG. Electron Spectroscopy for Chemical Analysis. In: Vickerman JC, Gilmore IS, editors. Surface Analysis The Principal Techniques. Second Edi. John Wiley & Sons Ltd.; 2009. p. 47–113.

71. Raff LM. Spin-Orbit Coupling. In: Challice J, editor. Principles of Physical Chemistry. Upper Saddle River, NJ: Prentice-Hall Inc.; 2001. p. 712–4.

72. Mathieu HJ. Auger Electron Spectroscopy. In: Vickerman JC, Gilmore IS, editors. Surface Analysis The Principal Techniques. Second Edi. John Wiley & Sons Ltd.; 2009. p. 9–47.

73. Lucas CA. Surface Structure Determination by Interference Techniques. In: Vickerman JC, Gilmore IS, editors. Surface Analysis The Principal Techniques. Second Edi. 2009. p. 391–479.

74. King DA. Thermal desorption from metal surfaces: a review. Surf Sci. 1975;47:384–402.

75. Attard G, Barnes C. Surfaces. Compton RG, Davies SG, Evans J, Gladden LF, editors. Oxford University Press; 1998.

76. Jones JE. Reactions and Synthesis of Isocyanate on Pt(111). University of Illinois at Chicago; 2010.

77. Waluyo I, Ren Y, Trenary M. Observation of tunneling in the hydrogenation of atomic nitrogen on the Ru(001) surface to form NH. J Phys Chem Lett. 2013;4(21):3779–86.

78. Hagans PL, Chorkendorff I, Yates JT. Scanning kinetic spectroscopy and temperature-programmed desorption studies of the adsorption and decomposition of HCN on the Ni(111) surface. J Phys Chem. 1988;92(2):471–6.

79. Kresse G, Furthmüller J. Efficient iterative schemes for ab initio total-energy calculations

using a plane-wave basis set. Phys Rev B - Condens Matter Mater Phys. 1996;54:11169–86.

80. Klimeš J, Bowler DR, Michaelides A. Chemical accuracy for the van der Waals density functional. J Phys Condens Matter. 2010;22:1–5.

81. Klimeš J, Bowler DR, Michaelides A. Van der Waals density functionals applied to solids. Phys Rev B - Condens Matter Mater Phys. 2011;83:1–13.

82. Hammer B, Hansen LB, Nørskov JK. Improved adsorption energetics within density-functional theory using revised Perdew-Burke-Ernzerhof functionals. Phys Rev B - Condens Matter Mater Phys. 1999;59(11):7413–21.

83. Blöchl PE. Projector augmented-wave method. Phys Rev B. 1994;50:17953–79.

84. Kresse G, Joubert D. From ultrasoft pseudopotentials to the projector augmented-wave method. Phys Rev B - Condens Matter Mater Phys. 1999;59:1758–75.

85. Methfessel M, Paxton AT. High-precision sampling for Brillouin-zone integration in metals. Phys Rev B. 1989;40:3616–21.

86. Ashcroft NW, Mermin ND. Solid State Physics. Solid State Physics. New York: Holt, Rinehart and Winston; 1976.

87. Neugebauer J, Scheffler M. Adsorbate-substrate and adsorbate-adsorbate interactions of Na and K adlayers on Al(111). Phys Rev B. 1992;46(24):16067–80.

88. Henkelman G, Uberuaga BP, Jónsson H. Climbing image nudged elastic band method for finding saddle points and minimum energy paths. J Chem Phys. 2000;113:9901–4.

89. Henkelman G, Jónsson H. A dimer method for finding saddle points on high dimensional potential surfaces using only first derivatives. J Chem Phys. 1999;111:7010–22.

90. Bahn SR, Jacobsen KW. An Object-Oriented Scripting Interface to a Legacy Electronic Structure Code. Comput Sci Eng. 2002;4:56–66.

91. Hoffman RE, Hornig DF. The infra-red spectrum of solid hydrogen cyanide. J Chem Phys. 1949;17:1163.

92. Friedrich HB, Krause PF. Internal vibrational modes and hydrogen bonding in mixed crystals of HCN and DCN. J Chem Phys. 1973;59:4942–8.

93. Gerakines PA, Moore MH, Hudson RL. Ultraviolet photolysis and proton irradiation of astrophysical ice analogs containing hydrogen cyanide. Icarus. 2004;170:202–13.

94. Couturier-Tamburelli I, Piétri N, Letty V Le, Chiavassa T, Gudipati M. UV–Vis Light-induced Aging of Titan's Haze and Ice. Astrophys J. 2018;852:117.

95. Choi KN, Barker EF. Spectrum of Hydrogen Cyanide. Phys Rev. 1932;42:777–85.

96. Momma K, Izumi F. VESTA: A three-dimensional visualization system for electronic and structural analysis. J Appl Crystallogr. 2008;41:653–8.

97. Herron JA, Tonelli S, Mavrikakis M. Atomic and molecular adsorption on Pd(111). Surf

Sci. 2012;606:1670–9.

98. Kordesch ME, Stenzel W, Conrad H. A comparison of single-, double-, triple-bonded and aromatic CN compounds on Pd(111) and (100) I. HREELS of NCCN, ethylenediamine and s-triazine. Surf Sci. 1987;186:601–23.

99. Hensley AJR, Ghale K, Rieg C, Dang T, Anderst E, Studt F, et al. DFT-Based Method for More Accurate Adsorption Energies: An Adaptive Sum of Energies from RPBE and vdW Density Functionals. J Phys Chem C. 2017;121:4937–45.

100. Guo X, Huffman A, Yates JT. HCN adsorption on the Pd(111) surface: Surface temperature and coverage dependence. J Phys Chem. 1989;93:4253–8.

101. Wellendorff J, Silbaugh TL, Garcia-Pintos D, Nørskov JK, Bligaard T, Studt F, et al. A benchmark database for adsorption bond energies to transition metal surfaces and comparison to selected DFT functionals. Surf Sci. 2015;640:36–44.

102. Fermann JT, Auerbach S. Modeling proton mobility in acidic zeolite clusters. II. Room temperature tunneling effects from semiclassical rate theory. J Chem Phys. 2000;112:6787–94.

103. Rasmussen PB, Holmblad PM, Christoffersen H, Taylor PA, Chorkendorff I. Dissociative adsorption of hydrogen on Cu(100) at low temperatures. Surf Sci. 1993;287–288:79–83.

104. Mills P, Jentz D, Trenary M. Formation of iminium ($C = NH_2$) species from cyanogen (C_2N_2) and hydrogen on Pt(111). J Am Chem Soc. 1997;119:9002–9.

105. Somers JS, Kordesch ME, Hemmen R, Lindner T, Conrad H, Bradshaw AM. An angle-resolved photoemission investigation of CN, HCN and C_2N_2 adsorbed on Pd{111} using synchrotron radiation. Surf Sci. 1988;198:400–12.

106. Shirley DA. High-resolution x-ray photoemission spectrum of the valence bands of gold. Phys Rev B. 1972;5(12):4709–14.

107. Powell CJ, Jablonski A. NIST Electron Inelastic Mean Free Path Database Version 1.2. Gaithersburg, MD: National Institute of Standards and Technology; 2010.

108. Kanama D, Oyama ST, Otani S, Cox DF. Photoemission and LEED characterization of $Ni_2P(0001)$. Surf Sci. 2004;552:8–16.

109. Yeh JJ, Lindau I. Atomic subshell photoionization cross sections and asymmetry parameters: 1<= Z <= 103. At Data Nucl Data Tables. 1985;32:1–155.

110. Mendialdua J, Casanova R, Barbaux Y. XPS studies of V_2O_5, V_6O_{13}, VO_2 and V_2O_3. J Electron Spectros Relat Phenomena. 1995;71:249–61.

111. Silversmit G, Depla D, Poelman H, Marin GB, De Gryse R. Determination of the V2p XPS binding energies for different vanadium oxidation states (V^{5+} to V^{0+}). J Electron Spectros Relat Phenomena. 2004;135:167–75.

112. Zhang Z, Henrich VE. Surface electronic structure of $V_2O_5(001)$: defect states and chemisorption. Surf Sci. 1994;321:133–44.

113. Heber M, Grünert W. Application of ultraviolet photoelectron spectroscopy in the surface characterization of polycrystalline oxide catalysts. 2. Depth variation of the reduction degree in the surface region of partially reduced V_2O_5. J Phys Chem B. 2000;104:5288–97.

114. Starr DE, Mendes FMT, Middeke J, Blum RP, Niehus H, Lahav D, et al. Preparation and characterization of well-ordered, thin niobia films on a metal substrate. Surf Sci. 2005;599:14–26.

115. Enjalbert R, Galy J. A refinement of the structure of V_2O_5. Acta Crystallogr C. 1986;42:68–72.

116. Sanchez C, Livage J, Lucazeau G. Infrared and Raman Study of Amorphous V_2O_5. J Raman Spectrosc. 1982;12:68–72.

117. Wachs IE. Raman and IR studies of surface metal oxide species on oxide supports: Supported metal oxide catalysts. Catal Today. 1996;27:437–55.

118. Šurca A, Orel B. IR spectroscopy of crystalline V_2O_5 films in different stages of lithiation. Electrochim Acta. 1999;44:3051–7.

119. Ryczkowski J. IR spectroscopy in catalysis. Catal Today. 2001;68:263–381.

120. Botto IL, Vassallo MB, Baran EJ, Minelli G. IR spectra of VO_2 and V_2O_3. Mater Chem Phys. 1997;50:267–70.

121. Magg N, Giorgi JB, Schroeder T, Bäumer M, Freund HJ. Model catalyst studies on vanadia particles deposited onto a thin-film alumina support - 1. Structural characterization. J Phys Chem B. 2002;106:8756–61.

122. Jehng JM, Deo G, Weckhuysen BM, Wachs IE. Effect of water vapor on the molecular structures of supported vanadium oxide catalysts at elevated temperatures. J Mol Catal A Chem. 1996;110:41–54.

123. Koduru HK, Obili HM, Cecilia G. Spectroscopic and electrochromic properties of activated reactive evaporated nano-crystalline V_2O_5 thin films grown on flexible substrates. Int Nano Lett. 2013;3:1–8.

124. NIST X-ray photoelectron spectroscopy database. In: NIST Standard Reference Database Number 20. Gaithersburg, MD: National Institute of Standards and Technology; 2000.

125. NIST Mass Spectrometry Data Center, Wallace WE. Mass Spectra. In: Winstrom P., Mallard WG, editors. NIST Chemistry Webbook, NIST Standard Reference Database Number 69. Gaithersburg, MD: National Institute of Standards and Technology;

126. Cao Y, Wang H, Ding R, Wang L, Liu Z, Lv B. Highly efficient oxidative desulfurization of dibenzothiophene using Ni modified MoO_3 catalyst. Appl Catal A Gen. 2020;589:1–8.

127. Kruppe CM, Krooswyk JD, Trenary M. Polarization-Dependent Infrared Spectroscopy of Adsorbed Carbon Monoxide to Probe the Surface of a Pd/Cu(111) Single-Atom Alloy. J Phys Chem C. 2017;121:9361–9.

128. Chesters MA, McCash EM. A fourier-transform reflection-absorption infrared

spectroscopic study of alkyne adsorption on Cu(111). J Electron Spectros Relat Phenomena. 1987;44:99–108.

129. Toomes RL, Lindsay R, Baumgärtel P, Terborg R, Hoeft JT, Koebbel A, et al. Structure determination of propyne and 3,3,3-trifluoropropyne on Cu(111). J Chem Phys. 2000;112:7591–9.

130. Clotet A, Ricart JM, Illas F, Pacchioni G, Lambert RM. A theoretical study of catalytic coupling of propyne on Cu{111}. J Am Chem Soc. 2000;122:7573–8.

131. Valcarcel A, Ricart JM, Clotet A, Markovits A, Minot C, Illas F. Structure and bonding of propyne on Cu(111) from density functional periodic and cluster models. J Chem Phys. 2002;116:1165–70.

132. Valcárcel A, Ricart JM, Illas F, Clotet A. Theoretical interpretation of the IR spectrum of propyne on Cu(111). J Phys Chem B. 2004;108(47):18297–305.

133. Martorell BJ, Clotet A. CH_2CHCH: A key isomer of propyne. adsorption structures and IR spectra on Cu(111). J Phys Chem C. 2009;113:950–64.

134. Roberts AJ, Haq S, Raval R. Propyne chemistry on Ni(111) and Cu(110); analogies with ethyne adsorption. J Chem Soc Faraday Trans. 1996 Apr 15;92:4823–7.

135. Middleton RL, Lambert RM. Catalytic coupling of propyne on Cu{111}. Catal Letters. 1999;59:15–20.

136. Aaen AB, Lægsgaard E, Ruban A V, Stensgaard I. Submonolayer growth of Pd on Cu (111) studied by scanning tunneling microscopy. Surf Sci. 1998;408:43–56.

137. Huang WX, White JM. Propene adsorption on Ag(111): A TPD and RAIRS study. Surf Sci. 2002;513:399–404.

138. Meyers JM, Gellman AJ. The investigation of fluorinated propenes on the Cu(111) surface. Surf Sci. 1995;339:57–67.

139. Street SC, Gellman AJ. Orientation of physisorbed fluoropropenes on Cu(111). J Phys Chem B. 1997;101:1389–95.

140. Miller BP, Furlong OJ, Tysoe WT. The desorption and reaction of 1-alkenes and 1-alkynes on Cu(111) and copper foils. Surf Sci. 2013;616:143–8.

141. van Kooten WEJ, Kragten DD, Gijzeman OLJ, Geus JW. Hydrocarbon interaction with clean and oxidised Cu(111). Surf Sci. 1993;290:302–8.

142. Stacchiola D, Burkholder L, Tysoe WT. Structure and reactivity of propylene on clean and hydrogen-covered Pd(111). Surf Sci. 2003;542:129–41.

143. Griffiths PR, de Haseth JA. Apodization. In: Fourier Transform Infrared Spectroscopy, Second Edition. Second Edi. John Wiley & Sons Ltd.; 2007. p. 30–6.

144. Lord RC, Venkateswarlu P. The infrared spectra of propylene and propylene-d_6*. J Opt Soc Am. 1953;43:1079.

Appendices

Appendix A: Peripheral Work

A.1 Reaction Pathways of HCN on Transition Metal Surfaces

The method of Hagans et al. (78) was used to synthesize HCN and its ^{13}C and ^{15}N isotopologues. $K^{12}C^{14}N(s)$, 1.0 g, was reacted with excess, ~ 5 mL, of 50% $H_2SO_4(aq)$ to produce $HCN(g)$, $H_2O(g)$, and $K_2SO_4(aq)$ according to the chemical equation:

$$2\,KCN(s) + H_2SO_4(aq) + H_2O(l) \rightarrow 2\,HCN(g) + K_2SO_4(aq) + H_2O(g) \qquad \text{Equation A.1}$$

Figure 49 A photograph of the glass apparatus used for the synthesis of HCN.

The synthesis was conducted in a glass apparatus (Figure 49) that was evacuated to ~10 mTorr with a Pfeiffer rotary vane pump. Some of the glassware used for this synthesis was modified by the glass shop at UIC. A two-neck 25-mL round bottom flask was attached to a three-neck 250-mL round bottom flask with adapters and elbows. The three-neck flask was attached to a custom glass manifold that has a port to connect a stainless-steel gas containment bottle, a cold trap, and a pumping port. The open neck of the 25-mL round bottom flask was sealed with a rubber septum, and the remaining openings were sealed with glass stoppers.

The reaction took place in the 25-mL round bottom flask, and the 250-mL round bottom flask was partially filled with P_2O_5 to remove some of the produced water. The stainless-steel bottle was cooled with liquid N_2 to trap the reaction products. The reaction and drying vessels were isolated from the manifold, and H_2SO_4 was added in serial injections through the rubber septum with a 1.0-mL syringe until there was no more gas evolution upon addition of acid. Once the reaction ended, the reaction vessel was isolated. The drying vessel was opened to the cooled bottle and the gases were captured for approximately 10 minutes. The bellows-sealed valve above the bottle was closed and the system was opened to the pump. After another 10 minutes, the reaction vessel was opened to the pump. The pump exhaust hose was submerged in $AgNO_3$ solution as a safety precaution. HCN reacts with $AgNO_3$ to produce AgCN and dilute HNO_3. The presence of AgCN was determined by the formation of a white precipitate in the solution vessel. The synthesis of $H^{13}C^{14}N$ and $H^{12}C^{15}N$ were done following the same procedure; however, a lesser isotopically labeled KCN. amount of the appropriate KCN precursor was used due to the limited availability of the

After the synthesis was complete, the purity was determined with using the UTI 300c QMS in the XPS-System. A significant amount of H_2O was detected by the QMS; therefore, the

synthesized HCN was purified by transferring the gas from the impure vessel cooled by a 200 K ethanol/dry ice bath to a clean vessel cooled by liquid N_2. The 200 K cold bath was used because the vapor pressure of HCN is significantly greater than that of H_2O at 200 K even though both species would be in a frozen state. HCN distillation was done in 1.0 Torr increments until a desired pressure (~100 Torr) was reached. The purity was checked again with the QMS and the results are shown in Figure 41.

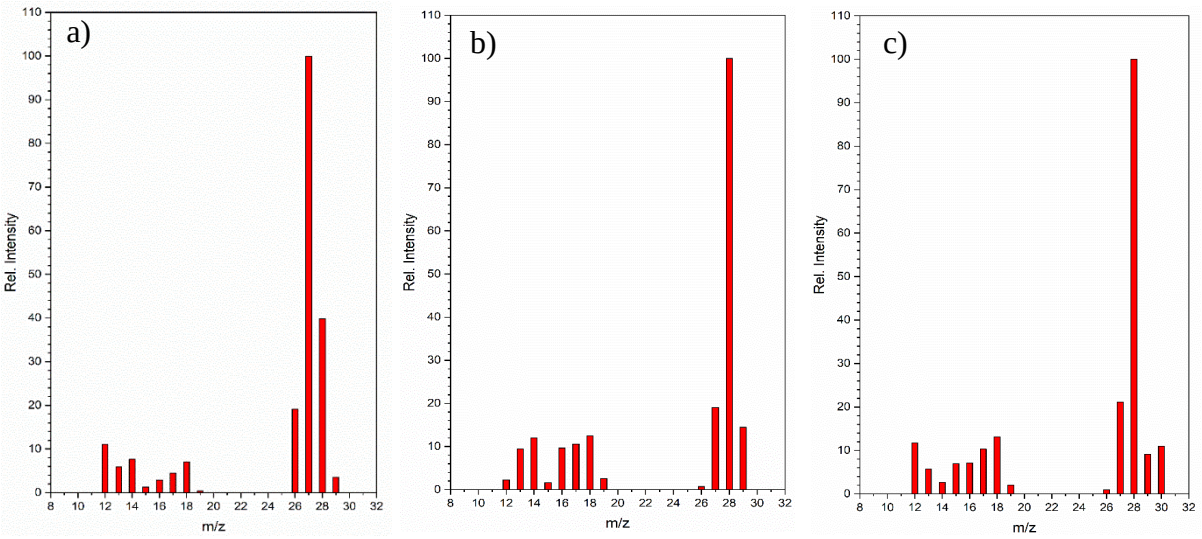

Figure 50 Mass spectra of 5.0×10^{-8} Torr of $H^{12}C^{14}N$ (a), $H^{13}C^{14}N$ (b), and $H^{12}C^{15}N$ (c). The synthesized products were determined to be pure by comparing the relative intensity of mass number 26 for $H^{12}C^{14}N$ (27 for the heavier isotopes) with that of the electron impact mass spectrum of HCN in the NIST database. An intensity of 20% relative to the parent mass number (27 for $H^{12}C^{14}N$ and 28 for the heavier isotopes) agrees with the national standard indicating successful synthesis and purification of HCN.

The deposition of HCN on Pd(111) was characterized with RAIRS to determine which vibrational modes are observed. Figure 51 shows the RAIR spectra with increasing exposures from 0.2 – 0.5 L of HCN. The only feature observed at 0.2 L is a peak at 1780 cm^{-1} which we attribute to background CO adsorbed on Pd(111). It is possible that di-σ HCN is present at 0.2 L since there are no vibration modes that would be detectible by RAIRS; however, this reasoning is not sufficient to draw this conclusion.

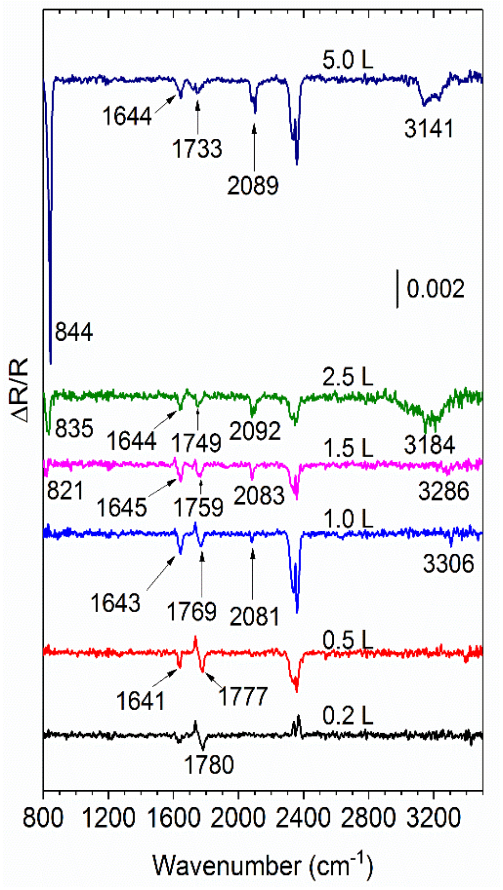

Figure 51 RAIR spectra of $H^{12}C^{14}N$ on Pd(111) taken at 90 K on clean Pd(111). The band beginning at 821 cm^{-1} corresponding to the HCN bending mode which only appears in the multilayer spectra due the RAIRS selection rules. Solid HCN begins forming at exposures of 2.5 L as indicated by the broad C-H stretching mode at 3184 cm^{-1}.

With the aid of DFT calculations, we propose that di-σ HCN should be present on the Pd(111) surface; thus, a featureless spectrum is observed. At 0.5 L, a peak at 1641 cm^{-1} appears which is attributed to 2 × δ(HCN) mode. The surface begins to saturate and some of the MSSR allowed modes of HCN are detected. The overtone of the HCN bend would be MSSR allowed for either the di-σ or upright HCN adsorption geometries. At 1.0 L, the surface is saturated with HCN, and the ν(CH) mode is observed at 3306 cm^{-1}, which is indicative of upright HCN. The 2 × δ(HCN) mode is at essentially the same frequency for the saturated surface, which indicates that the 1641 cm^{-1} peak observed at 0.5 L is most likely due to upright HCN. A small peak at 2081 cm^{-1} is visible at 1.0 L. This peak unambiguously corresponds to the ν(C≡N) mode of HCN providing additional evidence of upright HCN on Pd(111). Above 1.0 L, the RAIR features are those of solid HCN. The presence of solid HCN is indicated by a strong δ(HCN) mode at 844 cm^{-1} and a broad ν(CH) mode at 3141 cm^{-1}.

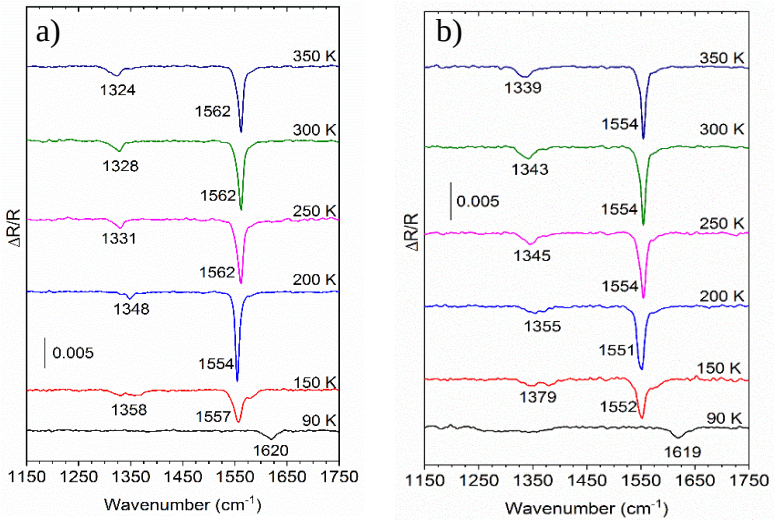

Figure 52 RAIR spectra of a) 1.0 L $H^{13}C^{14}N$ and b) 1.0 L $H^{12}C^{15}N$ on Pd(111) taken at 90 K after annealing for 1 minute at the indicated temperatures.

The formation of aminocarbyne on Pd(111) was determined by annealing the HCN covered surface to various temperatures and collecting RAIR spectra. The spectra of $H^{13}C^{14}N$ and $H^{12}C^{15}N$ are shown in Figure 52. These features are the same as those presented in Figure 17 of Chapter 3. The large shift of the peak from 1562 cm^{-1} ($H^{12}C^{14}N$) to 1554 cm^{-1} ($H^{12}C^{15}N$) allows us to unambiguously assign this peak to the $\delta(NH_2)$ mode of aminocarbyne since the peak is at essentially the same frequency upon ^{13}C substitution.

The effects of the H_2 on the presence of aminocarbyne were also investigated. The spectra are presented in Figure 53. When HCN was exposed to the H_2 covered surface, the intensity of the $\delta(CNH_2)$ peak decreased dramatically with increasing H_2 exposure. This indicates that HCN competes with H_2 for adsorption sites on Pd(111). As more H_2 is present, there are less available adsorption sites for HCN to adsorb, let alone react via the bi-molecular reaction pathway to form aminocarbyne. When H_2 is exposed after the Pd(111) surface is saturated with HCN, the transformation to aminocarbyne is also inhibited. Less aminocarbyne is formed when H_2 is introduced after HCN. This could be due to the mobility of the adsorbates when annealed to 300 K. It is possible that HCN is displaced by H_2 when annealed to 300 K thus making less HCN available for aminocarbyne production. Alternatively, if the formation of aminocarbyne occurs via the bi-molecular pathway, the adsorbed H_2 could prevent HCN from adsorbing at adjacent sites therefore preventing the first step of the bi-molecular mechanism.

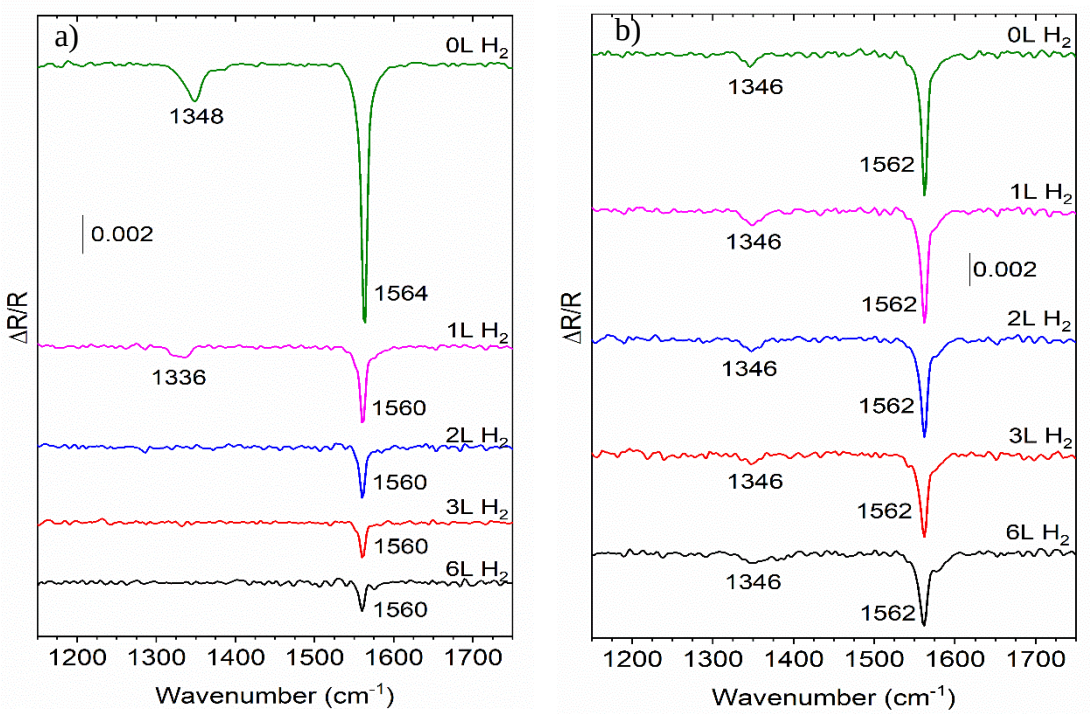

Figure 53 RAIR spectra taken at 90 K of $H^{12}C^{14}N$ on Pd(111) with H_2 pre-exposed (a) and post-deposition exposure of H_2 (b) annealed to 300 K for 1 min. Pre-exposure of H_2 has a more prominent effect on the NH_2 bending mode intensity of the aminocarbyne.

The reaction products of HCN adsorption were also probed with TPRS. The species of interest in this study were HCN (m/z = 27), CN (m/z = 26), H_2 (m/z = 2), and C_2N_2 (m/z = 56). Figure 54 contains TPR spectra from this study where only HCN and H_2 were found to desorb from the Pd(111) surface. The desorption peak at 120 K and the shoulder at 128 K are attributed to the HCN multilayer (α_1 and α_2) desorption. We did not observe HCN monolayer (α_3) desorption which Guo et al. (100) observed at 150 K. The absence of the α_3 can be explained by our RAIR spectra which indicate that HCN reacts to form CNH_2 at 150 K. The aminocarbyne then decomposes to either HCN or CNH, which desorbs at 397 K (β_1). We are unable to distinguish between hydrogen cyanide (HCN) and hydrogen isocyanide (CNH) as they have the same mass

spectrum. It is possible that CNH_2 undergoes dehydrogenation and desorbs from the surface as CNH with the remaining H_{ads} recombining and desorbing as H_2 at the same temperature. It was reported by Guo et al. (100) that HCN adsorption lead to some cyanogen (C_2N_2) formation as evidenced by their TPRS peak for C_2N_2 appearing at approximately 650 K; whereas, we were unable to detect cyanogen. It is plausible that our mass spectrometer could not achieve a sufficient sensitivity to detect C_2N_2.

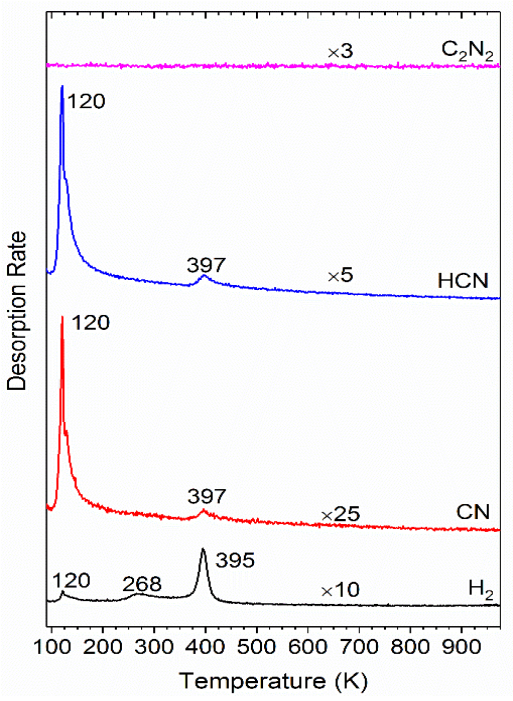

Figure 54 TPR spectra of 5.0 L HCN taken from 90-1000 K at a heating rate of 1.5 K/s. Desorption of H_2 and HCN were observed at ~400 K. C_2N_2 was not observed as a desorption product in this work.

Based on the adaptive summing method of Hensley et al. (99), when the GGA-RPBE ΔE_{ads} value for a gas molecule falls roughly below 70% of the corresponding value in optB86b-vdW, one may expect the contribution of vdW to the adsorption energy on a transition metal surface like Pd(111) to become significant. Table IX lists the ΔE_{ads} of several surface species that may be referenced directly to stable gas-phase species. See Ref. 91 for definition of the parameters *x* and *f*. An adaptively weighted sum of GGA-RPBE and optB86b-vdW ΔE_{ads} is found to be on average more accurate than that calculated using either functional alone. When $f = 1$ (as is the case for all the organic species listed in Table IX), this sum consists entirely of the optB86b-vdW ΔE_{ads}. When $f = 0$, the sum consists entirely of the GGA-RPBE ΔE_{ads}. Thus Table IX indicates that GGA-RPBE under-binds the organic species but is adequate for describing H adsorption, on Pd(111). Comparison with available literature data suggests this conclusion is correct.

Table IX DFT-calculated adsorption energies (ΔEads, in eV) of several molecular and atomic intermediates in HCN decomposition on Pd(111), and their associated adaptive summing parameters (*x* and *f*).

Species	ΔE_{ads}				ΔEads
	GGA-RPBE	optB86b-vdW	*x*	*f*	Exp. Lit.
HCN upright	0.00 [2]	-0.56 [2]	1.00	1.00	-0.39 [1]
HCN di-σ	-0.47 [2]	-1.29 [2]	0.63	1.00	
$(HCN)_2^{\alpha}$	-0.15 [2,3]	-1.02 [2,3]	0.86	1.00	
CNH	-1.08 [2]	-1.80 [2]	0.40	1.00	
H	-0.39 [4]	-0.57 [4]	0.31	0.01	-0.44 [5]

Each adsorbate is located on a (2×2) surface unit cell at 1/4 ML coverage. Δ*E*ads is with respect to each adsorbate in gas phase and is non-ZPE corrected.
1 From Ref. 2
2 With respect to gas-phase HCN.
3 Per unit of HCN.
4 With respect to gas-phase H_2, per H atom.
5 From Ref. 4.

A.2 Deposition and Characterization of Stoichiometric Films V_2O_5 on Pd(111)

The RAIR spectra presented in Chapter 4 were processed using cosine 4th apodization. Apodization of FTIR signals is a common practice to provide an instrumental lineshape function to the interferogram. Boxcar apodization is a basic truncation function that provides an instrumental lineshape; however, the side lobes of the interferogram remain significant. Other apodization functions are used to remove the side lobes of the instrumental lineshape. The relationship between the spectrum and interferogram is given by Equation A.1, where S(δ) is the interferogram intensity and D(δ) is the apodization function.

$$B(\tilde{\nu}) = \int_{-\infty}^{+\infty} S(\delta)D(\delta)\cos 2\pi\tilde{\nu}\delta \, d\delta \qquad \text{Equation A.2}$$

Apodization is done by limiting the retardation of the interferometer, δ, within a finite range of values, ±Δ. The triangular apodization function, $A_1(\delta)$, and the cosine apodization function, $A_2(\delta)$, are defined by the following conditions (143):

$$A_1(\delta) = D(\delta) \cdot [1 - \frac{|\delta|}{\Delta}] \qquad \text{Equation A.3}$$

$$A_2(\delta) = D(\delta) \cdot \frac{1}{2}\left[1 + \cos\left(\frac{\pi\delta}{\Delta}\right)\right] \qquad \text{Equation A.4}$$

There are various apodization functions embedded in many data acquisition software. Different apodization functions result in the spectral data being represented by different instrument line shape (ILS) functions. The ILS functions for the triangular and cosine apodization are given by equations A.3 and A.4 for the triangular and cosine apodization methods, respectively: (143):

$$f(\tilde{\nu}) = \Delta\text{sinc}^2(\pi\tilde{\nu}\Delta) \qquad \text{Equation A.5}$$

$$f(\tilde{\nu}) = \frac{2\Delta\,\text{sinc}(2\pi\tilde{\nu}\Delta)}{2\pi\tilde{\nu}(1-4\Delta^2\tilde{\nu}^2)} \qquad \text{Equation A.6}$$

The different ILS functions lead to different full width half maxima. The cosine apodization reduces the amplitude of the interference fringes; however, it also broadens the peak compared to the triangular apodization function. Figure 55 compare the RAIR spectra of V_2O_5 thin films when processed with triangular and cosine apodization functions. The peaks in Figure 55a are sharper than Figure 55b; however, there is a significant amount of interference in the spectra in Figure 55a.

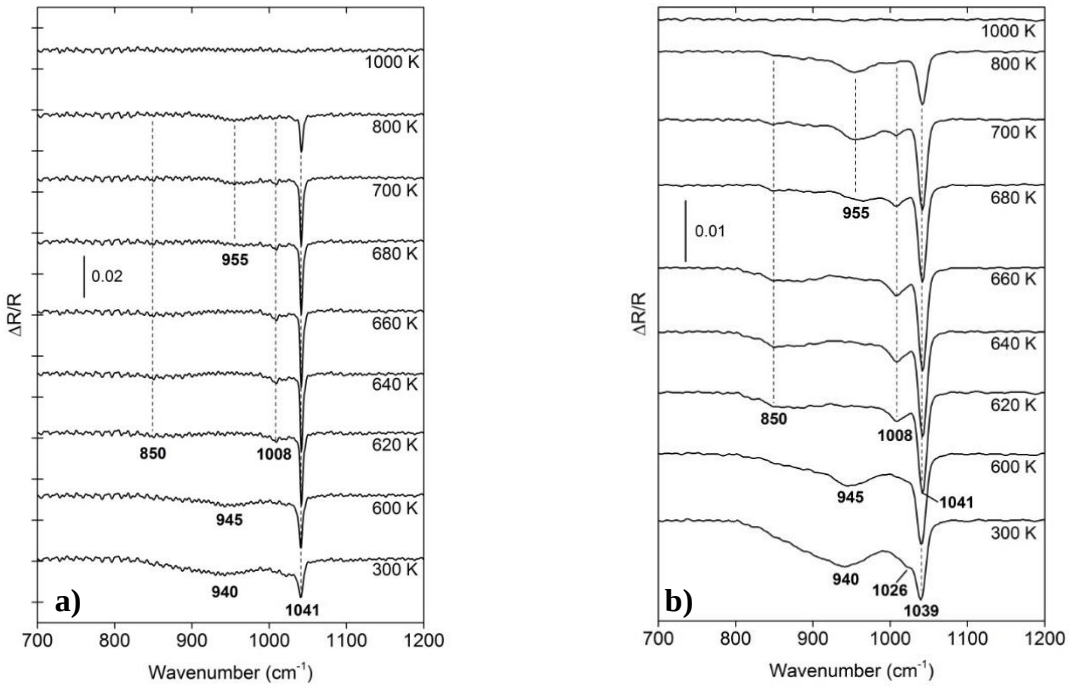

Figure 55 RAIR spectra of the sample for a 1.3 nm V_2O_5 thin film on Pd(111) at 300 K, as well as the sample after annealing up to 1000 K. All spectra were acquired at 300 K using 1024 scans and 2 cm^{-1} resolution with an MCT detector. The spectra in a) were processed with triangular apodization; whereas, the spectra in b) were processed with cosine 4^{th} apodization.

A.3 Propyne hydrogenation over a Pd/Cu(111) single atom alloy studied with ambient pressure infrared spectroscopy

A.3.1 IR spectra of propyne, propene, and propane

Gas phase propyne, propene, and propane IR spectra were collected individually to identify unique features to monitor the hydrogenation reaction. Figure 56 shows the IR spectra of the three gases with the unique features identified. Propyne is identified by unique peaks at 1260, 2200, and 3330 cm^{-1} corresponding to the first overtone of the C≡C–H bend, the C≡C stretch, and the ≡C–H stretch modes, respectively. Propyne has C_{3v} symmetry and its parallel vibrations have resolvable P and R branch envelopes. The most intense peak for propyne is the P branch of the ≡C–H stretch at 3323 cm^{-1}. This peak was monitored to determine how much propyne was consumed during the hydrogenation reactions.

Propene exhibits unique features at 912 (CH_2 wagging), 991 (allylic CH bending), 1650 (C=C stretching), 1820, 2000, and 3100 cm^{-1} (CH_2 antisymmetric stretching). The peak at 1820 cm^{-1} is attributed to the combination of CH_2 bending and CH stretching modes. The peak at 2000 cm^{-1} is attributed to the combination of the CH_3 wagging and CH bending modes. These assignments are based on gas phase IR spectra of propene and propene-d_6 by Lord and Venkateswarlu (144). The most intense peak for propene is the CH_2 wagging mode at 912 cm^{-1}. This peak was monitored to determine the amount of propene produced from the hydrogenation of propyne. Propene has C_s symmetry and some of its rotational structure is partially revolved.

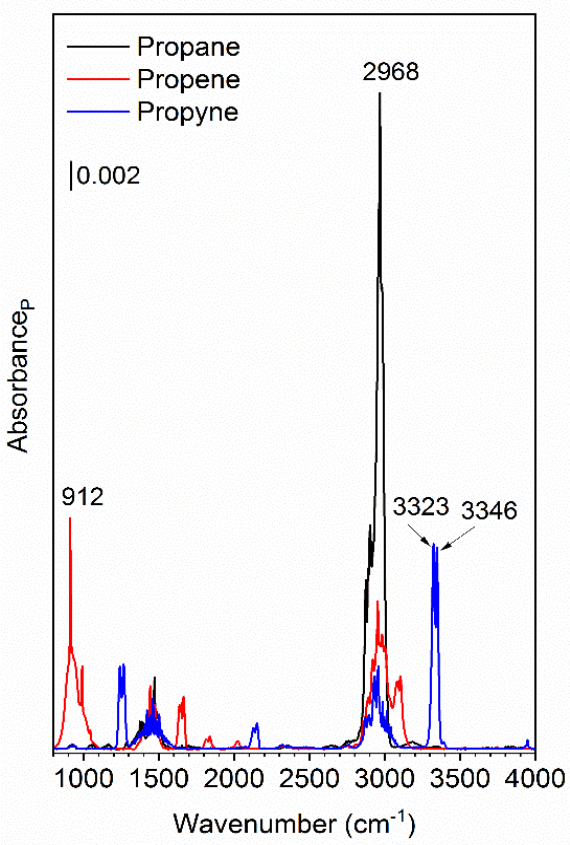

Figure 56 Infrared spectra of propyne, propene, and propane collected individually at 1 Torr.

The major peak for propane is at 2968 cm^{-1} corresponding to the CH_3 antisymmetric stretching mode. A peak at or near this value is observed for all three gases; however, it is significantly larger for propane than for propene and propyne at the same pressure. The antisymmetric methyl deformation mode at 1480 cm^{-1} overlaps with those of propene and propyne. Rotational fine structure is seen in all three gases for this mode. Propane would be noticeable as a hydrogenation product during the reaction because the CH_3 stretching peaks would dominate the spectrum, as opposed to the CH_2 bending or ≡C–H stretching peaks for propene and propyne, respectively.

A.3.2 Propyne and propene amounts from IR spectra

Figure 57 shows the infrared absorbance of propyne (3322 cm^{-1}) and propene (912 cm^{-1}) as the pressure is sequentially increased to 1.0 Torr in the IR cell. The plots in fig. 57 were fitted to the Beer-Lambert Law relating absorbance to partial pressure. The slopes of the lines correspond to the value of in the Beer-Lambert Law. The amount of propyne consumed during the reaction was calculated by converting IR absorbance to partial pressure then pressure to moles using the ideal gas law and the known temperature and volume of the IR cell.

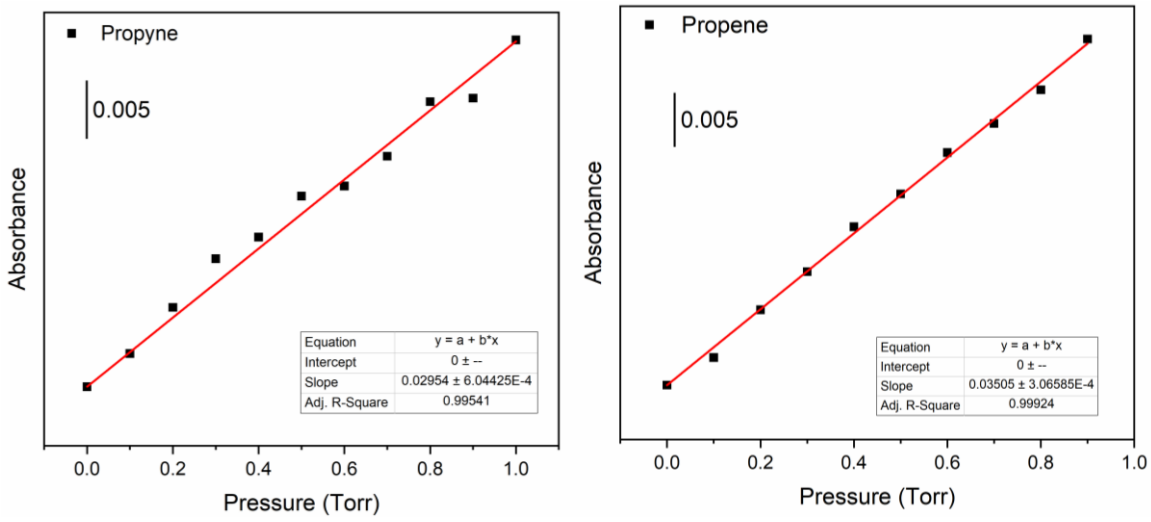

Figure 57 To relate IR absorbance to amount of propyne or propene in the reaction, 10 point calibration curves were generated by increasing the partial pressure of each gas in the IR cell by 0.1 Torr increments.

A.3.3 Surface composition by AES

The hydrogenation reaction over Cu and 2%Pd/Cu surfaces was characterized by AES. The C KVV, Pd MNN, and Cu LMM transitions are shown in Figure 58. The Auger spectra show a comparison of the interaction of propyne with both surfaces. After annealing at 500 K under 50 mTorr of propyne and 150 mTorr of H_2, the Cu catalyst has a surface composition of 71% carbon and 29% copper. After annealing at 1000 K, carbon-containing species were desorbed reducing the surface composition to 56% carbon and 44% copper. The 2% Pd/Cu surface composition becomes 68% carbon, 0.9% palladium, and 31.9% copper after annealing to 500 K. Approximately half of the palladium atoms diffuse into the Cu(111) crystal after annealing at 500 K. Upon annealing at 1000 K, carbon-containing species desorb from the surface and the remaining surface composition becomes 61.5% carbon and 38.5% copper. From the Auger spectra in Figure 58, the presence of palladium facilitates carbon removal at 500 K.

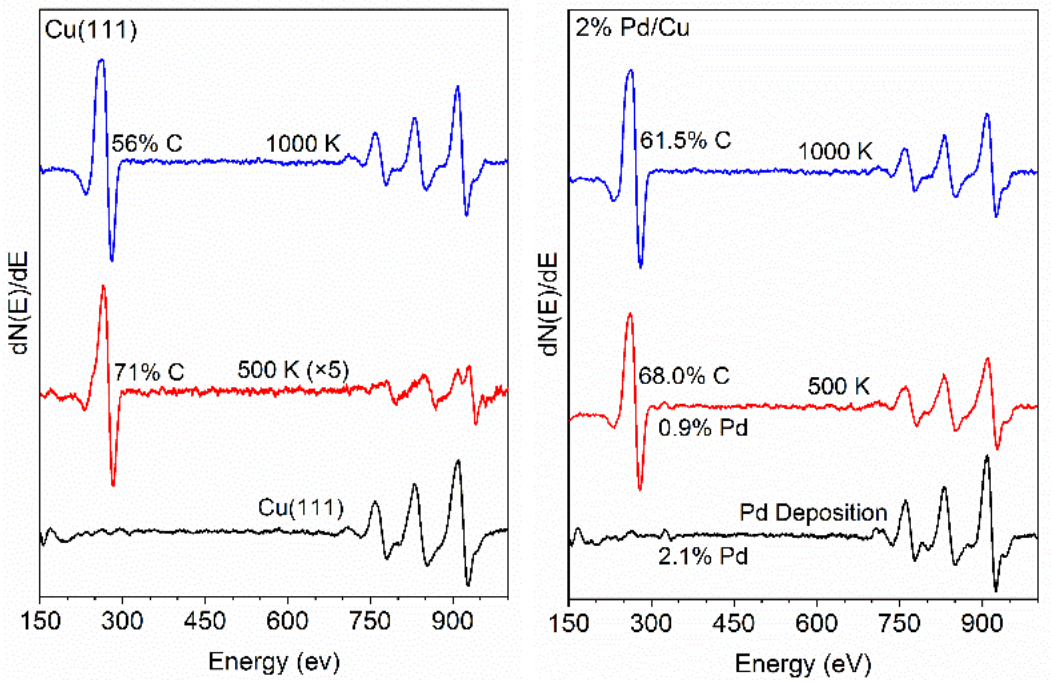

Figure 58 Auger spectra were collected from 150-1000 eV with a beam energy of 2.5 kV. The black spectra correspond to the catalyst after surface preparation. The red spectra were collected after annealing each catalyst in an ambient of 50 mTorr propyne and 150 mTorr H_2 at 500 K for one minute. The blue spectra were collected after heating the catalyst to 1000 K in UHV during the TPD studies.

Similar Auger spectra, shown in Figure 59 were collected for propene interacting with the two surfaces. In both cases, carbon deposited from propene exposure is more easily removed than from propyne exposure by annealing at 500 K. The Cu catalyst surface is composed of 50% carbon after annealing at 500 K. The carbon layer becomes slightly denser as H_2 is evolved when heated to 1000 K. The 2% Pd/Cu surface consists of only 14% carbon when annealed at 500 K indicating that desorption of carbon-containing species is greatly enhanced by the presence of palladium. More carbon is removed from the surface when heated to 1000 K.

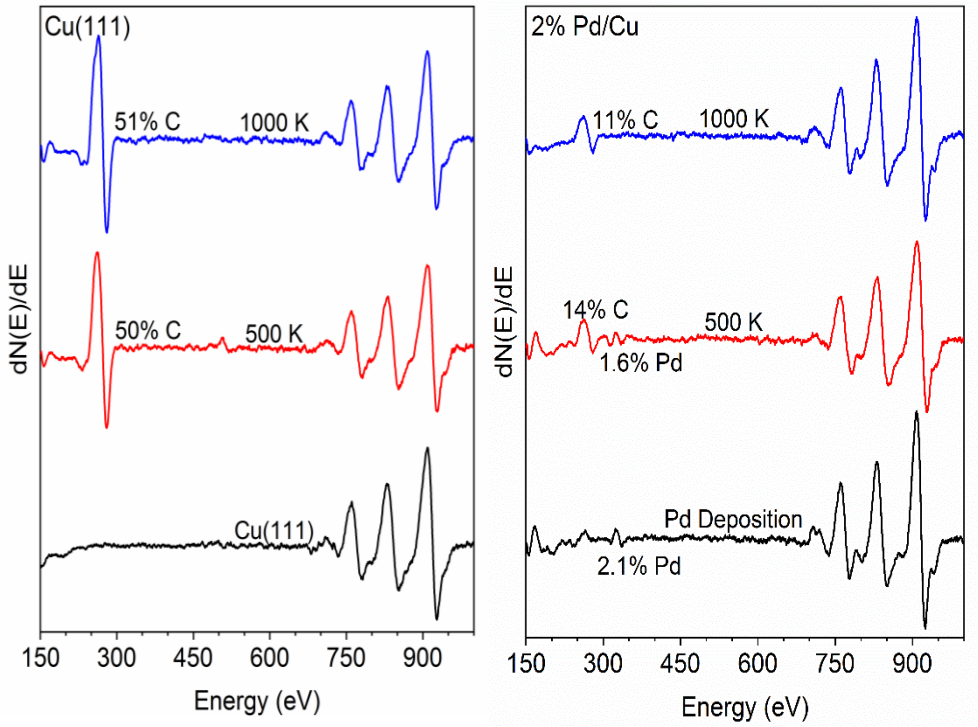

Figure 59 Auger spectra were collected from 150-1000 eV with a beam energy of 2.5 kV. The black spectra correspond to the catalyst after surface preparation. The red spectra were collected after annealing each catalyst in an ambient of 50 mTorr propene and 150 mTorr H_2 at 500 K for one minute. The blue spectra were collected after heating the catalyst to 1000 K in UHV for TPD studies.

After the reaction of 500 mTorr of propyne with 1500 mTorr of H_2 at 383 K, both the Cu and 2%PdCu catalyst surfaces are coated in carbon. The Auger spectra in Figure 60 show that after the reaction completed, the only Auger transition observed is C KVV. The Cu LMM and Pd MNN transitions were not detected. Since there was a propene yield of 50% under these conditions, it is likely the remaining 16 μmol of propyne either oligomerized or decomposed to form this carbonaceous layer.

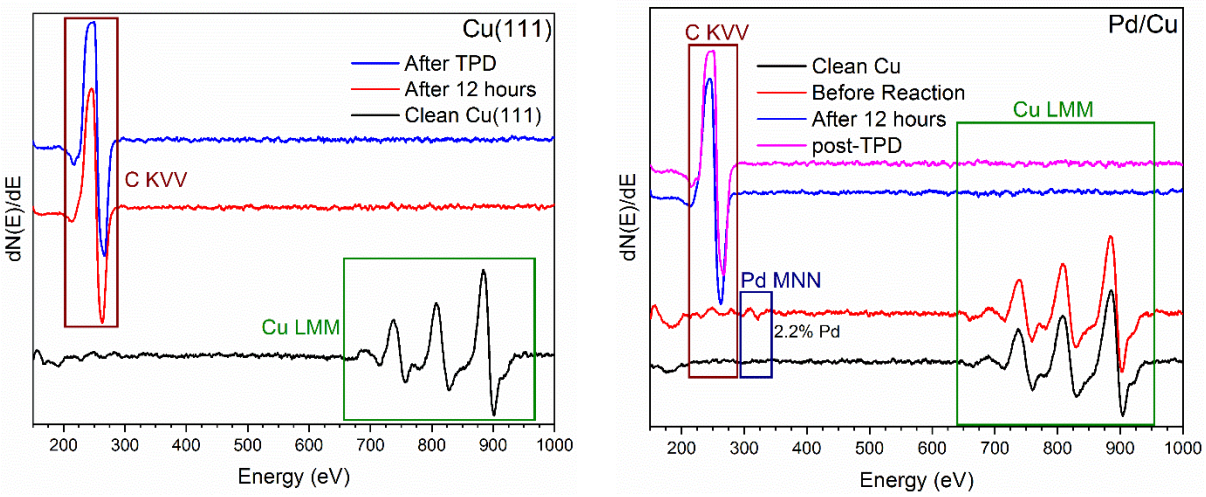

Figure 60 Auger spectra of the catalyst surface after propyne hydrogenation at 383 K after 12 hours and after heating to 1000 K in the course of obtaining TPD results. A carbonaceous layer coats both surfaces after the reaction is completed.

Appendix B: Permissions

Reaction pathways for HCN on transition metal surfaces

M. Abdel-Rahman, X. Feng, M. Muir, K. Ghale, Y. Xu and M. Trenary, *Phys. Chem. Chem. Phys.*, 2019, **21**, 5274
DOI: 10.1039/C8CP07548D

- For reproduction of material from PCCP:
  [Original citation] - Reproduced by permission of the PCCP Owner Societies
- For reproduction of material from PPS:
  [Original citation] - Reproduced by permission of The Royal Society of Chemistry (RSC) on behalf of the European Society for Photobiology, the European Photochemistry Association, and RSC
- For reproduction of material from all other RSC journals:
  [Original citation] - Reproduced by permission of The Royal Society of Chemistry

If you are the author of this article you still need to obtain permission to reproduce the whole article in a third party publication with the exception of reproduction of the whole article in a thesis or dissertation.

Information about reproducing material from RSC articles with different licences is available on our Permission Requests page.

Copyright Clearance Center | RightsLink®

Home | Help | Email Support | Mohammed Abdel-Rahman

surface science

Deposition and characterization of stoichiometric films of V2O5 on Pd(111)

Author: Xu Feng,Mohammed K. Abdel-Rahman,Christopher M. Kruppe,Michael Trenary

Publication: Surface Science

Publisher: Elsevier

Date: October 2017

© 2017 Elsevier B.V. All rights reserved.

Please note that, as the author of this Elsevier article, you retain the right to include it in a thesis or dissertation, provided it is not published commercially. Permission is not required, but please ensure that you reference the journal as the original source. For more information on this and on your other retained rights, please visit: https://www.elsevier.com/about/our-business/policies/copyright#Author-rights

BACK | CLOSE WINDOW

© 2020 Copyright - All Rights Reserved | Copyright Clearance Center, Inc. | Privacy statement | Terms and Conditions
Comments? We would like to hear from you. E-mail us at customercare@copyright.com

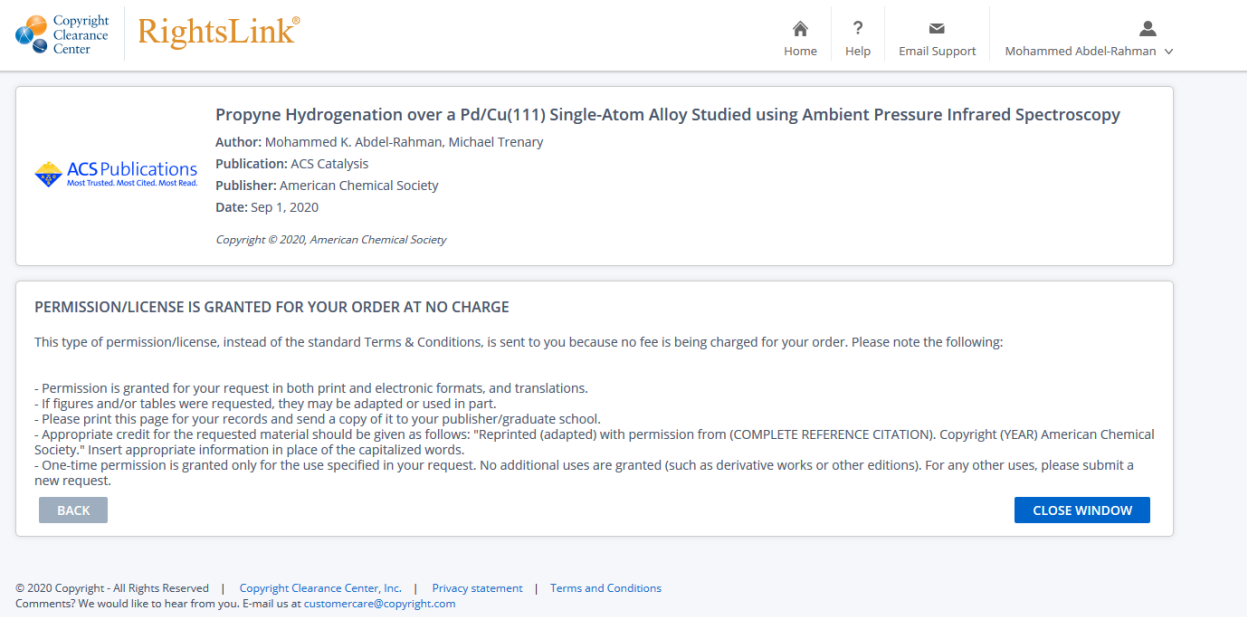

Copyright Clearance Center | RightsLink®

Home | Help | Email Support | Mohammed Abdel-Rahman

ACS Publications
Most Trusted. Most Cited. Most Read.

Propyne Hydrogenation over a Pd/Cu(111) Single-Atom Alloy Studied using Ambient Pressure Infrared Spectroscopy

Author: Mohammed K. Abdel-Rahman, Michael Trenary
Publication: ACS Catalysis
Publisher: American Chemical Society
Date: Sep 1, 2020

Copyright © 2020, American Chemical Society

PERMISSION/LICENSE IS GRANTED FOR YOUR ORDER AT NO CHARGE

This type of permission/license, instead of the standard Terms & Conditions, is sent to you because no fee is being charged for your order. Please note the following:

- Permission is granted for your request in both print and electronic formats, and translations.
- If figures and/or tables were requested, they may be adapted or used in part.
- Please print this page for your records and send a copy of it to your publisher/graduate school.
- Appropriate credit for the requested material should be given as follows: "Reprinted (adapted) with permission from (COMPLETE REFERENCE CITATION). Copyright (YEAR) American Chemical Society." Insert appropriate information in place of the capitalized words.
- One-time permission is granted only for the use specified in your request. No additional uses are granted (such as derivative works or other editions). For any other uses, please submit a new request.

BACK | CLOSE WINDOW

Vita

Mohammed K. Abdel-Rahman

Education

Ph.D. Physical Chemistry
University of Illinois at Chicago
Advisor: Michael Trenary

B.S. Chemistry
University of Illinois at Chicago 2012

Professional Experience

Afton Chemical Corporation
Lab Tech I 2012-2015

Publications

Islam, A.; **Abdel-Rahman, M.K.**; Trenary, M, Reversible Adsorption of Propyne on Cu(111) Studied with Infrared Spectroscopy. *In preparation.*

Muir, M.; Molina, D.L.; Islam, A.; **Abdel-Rahman, M.K.**; Trenary, M., Selctive Hydrogenation of Acrolein on a Pd/Ag(111) Single-Atom Alloy Surface. *J. Phys. Chem. C*, **2020**, 44, 24271-24278.

Muir, M; Molina, D.L.; Islam, A.; **Abdel-Rahman, M.K.**; Trenary, M., Adsorption Properties of Acrolein, Propanal, 2-Propenol, and 1-Propanol on Ag(111). *Phys. Chem. Chem. Phys.* **2020**, 22, 25011-25020.

Abdel-Rahman, M.K.; Trenary, M., Propyne Hydrogenation over a Pd/Cu(111) Single Atom Alloy Catalyst Studied with Ambient Pressure Infrared Spectroscopy, *ACS. Catal*. **2020**, 10, 9716-9724.

Abdel-Rahman, M.K.; Feng, X.; Muir, M.; Gale, K.; Xu, Y.; Trenary, M., Reaction Pathways for HCN on Transition Metal Surfaces, *Phys. Chem. Chem. Phys.*, **2019**, 21, 5274-5284.

Feng, X.; **Abdel-Rahman, M.K.**; Kruppe, C.M.; Trenary, M., Deposition and Characterization of Stoichiometric Films of V_2O_5 on Pd(111), *Surf. Sci.*, **2017**, 664, 1-7.

Presentations

"Propyne Hydrogenation over a Pd/Cu(111) Single Atom Alloy Catalyst Studied with Ambient Pressure Infrared Spectroscopy" AVS 66th International Symposium and Exhibition. Columbus,OH. October, 2019. Oral.

"Propyne Hydrogenation over a Pd/Cu(111) Single Atom Alloy Catalyst Studied with Ambient Pressure Infrared Spectroscopy" UIC Graduate Student Symposium. Chicago, IL. October, 2019. Poster.

"Propyne Hydrogenation over a Pd/Cu(111) Single Atom Alloy Catalyst Studied with Ambient Pressure Infrared Spectroscopy" AVS Prairie Chapter Symposium. Champaign, IL.September, 2019. Poster.

"Propyne Hydrogenation over a Pd/Cu(111) Single Atom Alloy Catalyst Studied with Ambient Pressure Infrared Spectroscopy" Catalysis Club of Chicago Spring Meeting. Chicago,IL. April, 2019. Oral.

"Propyne Hydrogenation over a Pd/Cu(111) Single Atom Alloy Catalyst Studied with Ambient Pressure Infrared Spectroscopy" ACS National Meeting Spring 2019. Orlando, FL. April, 2019. Oral.

"Reaction Pathways for HCN on Transition Metal Surfaces" UIC Graduate Student Symposium. Chicago, IL. October, 2017. Poster.

"Reaction Pathways for HCN on Transition Metal Surfaces" AVS Prairie Chapter Symposium. Milwaukee, WI. September, 2017. Poster.

Professional Memberships

American Chemical Society
American Vacuum Society
Catalysis Club of Chicago

Vita